

Development of new methods to detect and to prevent fouling of reverse osmosis membranes

Helge Hakon Oesinghaus

Vollständiger Abdruck der von der TUM School of Natural Sciences der Technischen Universität München zur Erlangung des akademischen Grades eines

Doktors der Ingenieurwissenschaften

genehmigten Dissertation.

Vorsitz:	Prof. Dr. Michael Rychlik
Prüfende der	1. Prof. Dr. Martin Elsner
Dissertation:	2. Hon.- Prof. Dr. Martina Gastl

Die Dissertation wurde am 15.10.2024 bei der Technischen Universität München eingereicht und durch die TUM School of Natural Sciences am 16.12.2024 angenommen.

Danksagung

Ich danke Vielen meinem Doktorvater Prof. Dr. Martin Elsner, für die Möglichkeit an diesem herausragendem Thema zu arbeiten, sowie für die stets kompetente und unkomplizierte Betreuung. Des Weiteren danke ich Prof. Dr. Martina Gastl für die Übernahme einer Begutachtung. Sie zeichnet sich durch Sachverstand aus, diese anwendungsorientierte Arbeit zu begutachten.

Ein besonderer Dank gilt meinem Arbeitsgruppenleiter Dr.-Ing. Karl Glas, der mich überhaupt erst von der Idee einer Promotion im Rahmen des Drittmittel finanzierten Bio-Mem Projektes überzeugen konnte. Weiterhin hatte er stets ein offenes Ohr für alle Sorgen, die während der Promotion entstanden sind und konnte mir durch seine weitreichenden Kontakte und durch seine Expertise in der Wasseraufbereitung immer schnell helfen.

Meiner Mentorin PD Dr. Ulrike Wacker danke ich für die die Unterstützung meiner Promotion, sowohl mental wie auch ganz praktisch, wie z.B. durch das Querlesen der Publikationen. Weiterhin möchte ich allen Projektpartnern, für die stets gute Kooperationsbereitschaft danken. Nicht zuletzt durch das breit aufgestellte Konsortium konnte ich viel über die Chemie von Desinfektionsmitteln von Dr. Stephanie Holz wie auch über Elektro- / und Datentechnik von Wolfgang Heigl und Wolfgang Ramin lernen. Dr. Florian Meier konnte meinen Horizont in der Membrantechnik durch die Feldflussfraktionierungstechnik erweitern. Der wissenschaftliche Austausch mit PD Dr. Natalia Ivleva wie auch Maximilian Huber war wertvoll, um Neues im Bereich der Spektroskopie zu erlernen.

Von universitärer Seite aus gebührt mein Dank Prof. Dr. Stephen Schrettl, der mit seinem neuen Auftreten in Weihenstephan gegen Ende meiner Promotion eine Sicherheit und eine Perspektive für meine Forschungsfelder vermitteln konnte. Ohne diese wäre diese Dissertation gerade gegen Ende nicht so reibungslos verlaufen. Des Weiteren gebührt mein Dank allen Kollegen der AG Wassertechnologie, die mich als ihr letztes Mitglied so gut aufgenommen haben. Das stets lehrreiche, freundschaftliche und in ihren Fachsimpeleien herausragende Verhältnis zum Christian von Heynitz ist hierbei besonders hervorzuheben. Ein besonderer Dank gebührt weiterhin den für diese Zeit zahlreichen Studenten: Daniel Wanken, Nora Eiden, Henrieke Carell, Kilian Lupp, Conrad Czuprin, Magdalena Bader und Vincent Meiß. Sie haben alle durch ihren Erfolg in ihrer studentischen Arbeiten maßgeblich zum Erfolg dieser Dissertation beigetragen. Weiterhin möchte ich Dr. Derek Kiebal danken, der durch sein Korrekturlesen das Englisch in dieser Dissertation maßgeblich verbessert hat.

Zuletzt möchte ich mich bei meinen Freisinger Freunden und im Besonderen bei meiner Freundin Judith bedanken, die viel Verständnis entgegengebracht haben, wenn der Stress überhand genommen hat oder sich der Feierabend mal wieder auf unbestimmte Zeit verzögerte.

Vorbemerkung

Der praktische Teil dieser Arbeit wurde vom September 2021 bis Mai 2024 in der Arbeitsgruppe für Wassertechnologie der Technischen Universität München durchgeführt. Die Arbeit wurde durch Prof. Dr. Martin Elsner des Instituts für Wasserchemie betreut.

Die wissenschaftlichen Veröffentlichungen [1–3] und Abbildungen wurden mit Genehmigung der Journals *BrewingScience*, *Membranes* und *Desalination and Water treatment* abgedruckt.

Publications

Peer-reviewed publications

*Denotes corresponding author, †denotes equal co-authorship.

S.Hager[†], H.Oesinghaus^{†*}, A.Bachmann, M. Meinardus, T. Hofmann, R. Engelbrecht and K.Glas. CaCO₃ deposits in reverse osmosis: Part III – Incipient Scaling detection via polymer optical fibre sensors. Comparison to hydrochemical prediction and image analytical methods. *BrewingScience*, **2023**, *76*, 1866-5195, doi: 10.23763/BrSc23-03hager [1]

H.Oesinghaus^{†*}, D. Wanken[†], K. Lupp, M. Gastl, M. Elsner and K. Glas. Incipient biofouling detection via fiber optical sensing and image analysis in reverse osmosis processes. *Membranes*, **2023**, *13*, 553, doi: 10.3390/membranes13060553 [2]

H.Oesinghaus*, E.E. Eiden, T. Kratky, M.J. Huber, S. Schrettl, S. Holz, M. Elsner and K. Glas. Analytical characterization of damage in reverse osmosis membranes caused by components of a chlorine dioxide matrix. *Desalination and Water Treatment*, **2024** doi: 10.1016/j.dwt.2024.100633. [3]

Abstract

In times of increasing water scarcity and expanding global population, there is a heightened demand for clean water. Technologies that can produce drinking water from almost any water source are attracting growing interest within both industry and scientific communities. Reverse osmosis (RO), a membrane separation process, is a process with the potential to contribute to these pressing global challenges.

Using RO, water constituents such as ions, viruses, bacteria, and drug residues are filtered out of the water, but the retained substances also concentrate on the membrane surface. This accumulation can lead to fouling, which can damage the membrane and limits its functionality.

This dissertation aims to advance solutions against the two most common types of fouling with novel *in-situ* sensor systems and pretreatment methods. For this purpose, two chapters in this dissertation investigate the feasibility of implementing fiber optic fouling sensors in RO plants. The newly developed sensors enabled the early detection of fouling events for mineral deposits (scaling) and biological deposits (biofouling). Existing countermeasures (antiscalants, pulsatile cross-flow) could also be monitored and controlled via the sensors.

A frequently used strategy against scaling is the addition of antiscalants into the feed water. However, they can promote the growth of microorganisms, which can lead to membrane clogging or degradation. While disinfectants or biocides are often used to inhibit the growth of such microorganisms, the biocides themselves can lead to degradation of the polyamide layer of the RO membrane.

In this context, the third chapter of this dissertation focuses on methods to enhance the applicability of chlorine dioxide as a biocide to effectively reduce biofilms while ideally maintaining the integrity of the membrane.

Our study took a comprehensive approach by considering the chemical components of a technical chlorine dioxide solution and examining their impact on RO membranes. This allowed us deconvolve the different putative oxidants that could potentially harm the membrane. Further analysis of process parameters led us to identify operational modes that caused the least damage to the RO membrane during disinfection. Moreover, we discovered that the key to achieving disinfection compatible with the membrane lay in using a chlorine dioxide solution that is as pure as possible and pH-neutral, while applying minimal mechanical stress to the membrane during biocide application.

Contents

Danksagung	2
Vorbemerkung	3
Publications	4
Abstract	I
Abbreviations and parameters	IV
1 Introduction	1
1.1 Reverse osmosis membranes - a pivotal component in water treatment	1
1.2 Fouling - the first Achilles' heel of reverse osmosis membranes	2
1.2.1 Reverse osmosis setups	3
1.2.2 Inorganic fouling - scaling	4
1.2.3 Biofouling	7
1.3 Antifouling strategies	11
1.4 Oxidative membrane degradation - the second Achilles' heel of reverse osmosis membranes	14
1.5 Evaluation of reverse osmosis process performance	16
2 Objective of this thesis	20
3 Results	22
3.1 Incipient scaling detection via polymer optical fiber sensors. Comparison to hydrochemical prediction and image analytical methods . .	23
3.1.1 Abstract	24
3.1.2 Introduction	24
3.1.3 Materials and methods	26
3.1.4 Experimental setup - POFs in different supersaturated salt solutions	28
3.1.5 Experimental setups and results	31
3.1.6 Conclusion	40
3.1.7 Outlook	40
3.1.8 Acknowledgments	41
3.1.9 References	42
3.2 Incipient biofouling detection via fiber optical sensing and image analysis in reverse osmosis processes	44
3.2.1 Abstract	45
3.2.2 Introduction	45
3.2.3 Materials and methods	47
3.2.4 Results and discussion	52

3.2.5	Conclusion	61
3.2.6	References	63
3.3	Analytical characterization of damage in reverse osmosis membranes caused by components of a chlorine dioxide matrix	65
3.3.1	Abstract	67
3.3.2	Introduction	67
3.3.3	Materials and Methods	71
3.3.4	Results and Discussion	74
3.3.5	Conclusions	86
3.3.6	References	87
4	Discussion	90
4.1	Early detection of fouling using polymer optical fibers	91
4.1.1	Detecting the early onset of scaling	91
4.1.2	Detecting the early onset of biofilm formation	93
4.2	Sensitivity of polymer optical fibers to existing anti-fouling treatments	95
4.3	Chlorine dioxide as a biocide for reverse osmosis membranes	96
4.4	Developments in fouling detection and prevention in reverse osmosis processes	97
4.5	Future opportunities for anti-fouling sensing and treatment	99
	Bibliography	101
	List of Figures	114
	List of Tables	119

Abbreviations and parameters

Symbols and model parameters

Parameter	Description	Unit
β	concentration factor	—
π	osmotic pressure	bar
c	concentration	mol L^{-1}
w	width	m
l	length	m
n	number of stages	—
r	recovery	%
t	time	second
v	velocity	m s^{-1}
A	membrane area	m^2
\dot{C}	carbon charge	mg s^{-1}
CF	concentration factor	—
D	diffusion coefficient	$\text{m}^2 \text{s}^{-1}$
FCP	feed channel pressure drop	bar
IAP	ion activity product	—
J_w	permeate flux	$\text{L m}^{-2} \text{h}^{-1}$
K_s	solubility product	—
LSI	Langlier saturation index	—
Q	flow rate	L h^{-1}
R	rejection	%
Re	Reynolds number	—
SI	saturation index	—
SP	salt passage	%
P	pressure	bar
P_w	permability	$\text{L m}^{-2} \text{h}^{-1} \text{bar}^{-1}$
T	temperature	$^{\circ}\text{C}$
TMP	trans membrane pressure	bar
TOC	total organic carbon	mg L^{-1}

Abbreviations

Abbreviation	Description
ACC	amorphous calcium carbonate
AS	anti-scalant
ATP	adenosine triphosphate
ATR	attenuated total reflection
CP	concentration polarization
CFU	colony forming unit
CIP	cleaning in place
DAF	dissolved air flotation
EIS	electron impedace spectroscopy
EPS	extracellular polysaccharide
FC	flow cytometry
FTIR	Fourier transformed infrared
GAC	granular activated carbon
LED	light emitting diode
MB	methylene blue
MCC	monohydrated calcium carbonate
MF	micro filtration
MFC	membrane flat cell
MO	microorganism
PAA	poly(acrylic acid)
PES	polyethersulfone
PMAA	poly(methacrylic acid)
PMA	poly(maleic acid)
PMMA	poly(mehtyl methacrylate)
POF	polymeric optical fiber
PP	polypropylene
RGB	red green blue
RO	reverse osmosis
SEM	scanning electron microscopy
SWM	spiral wound module
TCC	total cell number
UF	ultrafiltration
UTDR	ultrasonic time domain reflectrometry
XLE	extreme low energy consumption
XPS	X-ray photoelectron spectroscopy

1 Introduction

1.1 Reverse osmosis membranes - a pivotal component in water treatment

Water scarcity is increasing in many regions of the world due to a growing world population, widespread agricultural irrigation and the water demands of an increasing industrial development [4–7]. Commonly exploited water reservoirs are increasingly polluted [6], garnering interest in water purification techniques [5, 8]. One purification process that is even capable of producing drinkable water from seawater is reverse osmosis, given that reverse osmosis membranes are capable of removing inorganic, organic and biological pollutants from the feed water [2, 9, 10].

The most frequently used reverse osmosis membranes are polyamide (PA) thin film composite membranes, which consist of three different layers. The PA layer, which carries out the filtration, is only between 10 to 200 nm thick and typically rejects 99% of the dissolved ions from the feed water. A thicker microporous polyether sulfone layer and a polyester fleece serve as supports for the active filtration PA layer [11].

The membranes in reverse osmosis desalination are typically housed in spiral wound modules (SWM) that compact a high membrane surface area into a minimum amount of space (see Figure 1.1A). Between the wound membrane sheets, a feed spacer net (see Figure 1.1B) is placed to separate the two active filtration sides of the membranes and to enhance the mixing of the feed in order to minimize the effects of concentration polarization at the membrane surface [7]. Concentration polarization is a boundary layer effect that describes the concentration gradient of different solutes in the water that are retained by the membrane at the surface. Finally, the permeate is drained through the permeate carrier to a perforated permeate pipe.

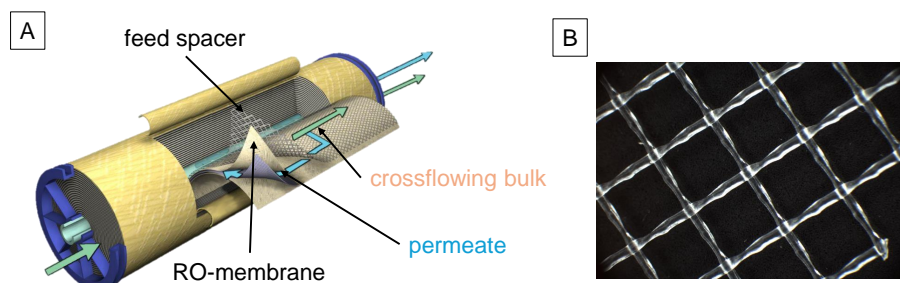


Figure 1.1: A) Composition of a spiral wound module, B) feed spacer from a commercially available LOW 4 Oltremare SWM module.

Standard reverse osmosis setups like the one just described are inherently vulnerable to different types of deposits on the membrane and spacer surfaces. The formation

of deposits in this way on the membrane surface is known as fouling and impedes the filtration technology significantly. Despite efforts to curb reverse osmosis membrane fouling, especially on an industrial scale [12–14], few solutions exist that adequately address the problem of fouling of reverse osmosis membranes. Tackling this issue is the intrinsic motivation for this dissertation.

1.2 Fouling - the first Achilles' heel of reverse osmosis membranes

The fouling of reverse osmosis membrane systems can be divided into four different forms of fouling (Figure 1.2): colloidal fouling, inorganic fouling (scaling), organic fouling and biological fouling (biofouling) [15]. The two most detected forms of fouling that are discovered in reverse osmosis modules during membrane autopsies are biofouling (31 %) and scaling (32 %) [16].

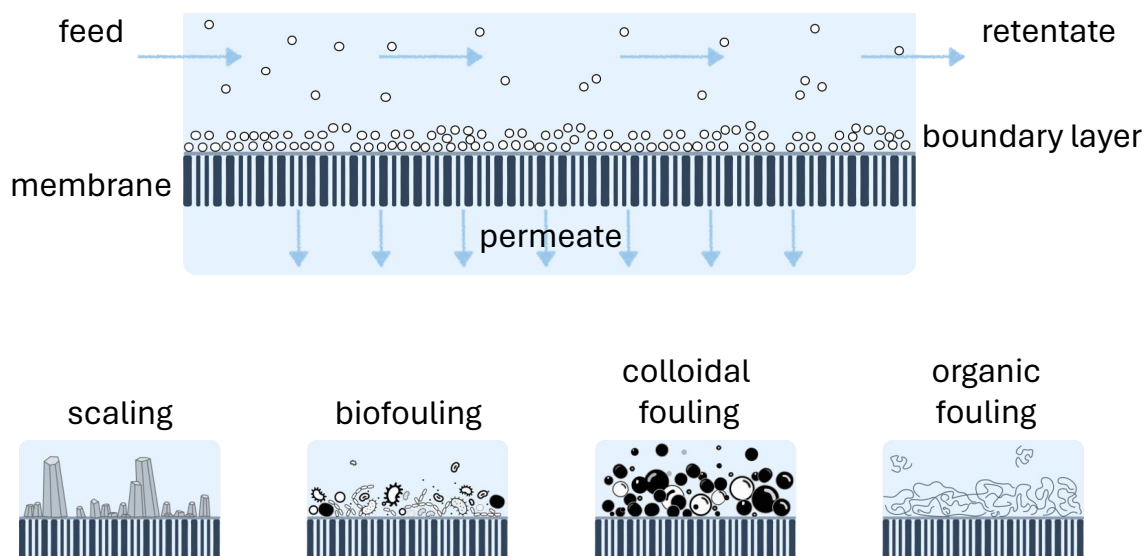


Figure 1.2: Top: Reverse osmosis membrane during operation. Shown are the typical cross-flow conditions with a forming boundary layer. The permeate (purified water) is pressed through the membrane. Bottom: Displayed are the four different types of fouling, formed by the rejected water impurities that are concentrated at the boundary layer.

The fouling, whether it occurs in the feed channel or on the membrane, impacts the properties of the reverse osmosis system. Changes in the hydraulic parameters of the feed channel that are caused by fouling typically result in reduced selectivity and productivity of the membrane (see Section 1.5). In order to avoid such losses in membrane efficiency, the SWMs of industrial reverse osmosis plants are installed under specific conditions that attempt to control where and how the fouling occurs.

1.2.1 Reverse osmosis setups

In order to maximize the efficiency of energy and water recovery, SWMs in reverse osmosis plants are normally installed in series [17] in a way similar to that depicted in Figure 1.3. The retentate of the SWMs in the first stage is recycled and used as the feed of the second stage [18–22].

However, according to the conservation of mass and depending on the recovery (r) efficiency of each stage, the feed of the second stage is diminished by the permeate rejection of the first stage. For each stage the recovery in the most RO plants is about 50 % [23, 24].

$$r = \frac{Q_P}{Q_F} \quad (1.1)$$

As a result, the overflow velocity and thus filtration efficiency decreases in the following stages. This issue can be solved partly by coupling SWMs in parallel in the first stage (Figure 1.3B). The cross-flow velocity will however not be stabilized over the whole length of the SWMs in every stage.

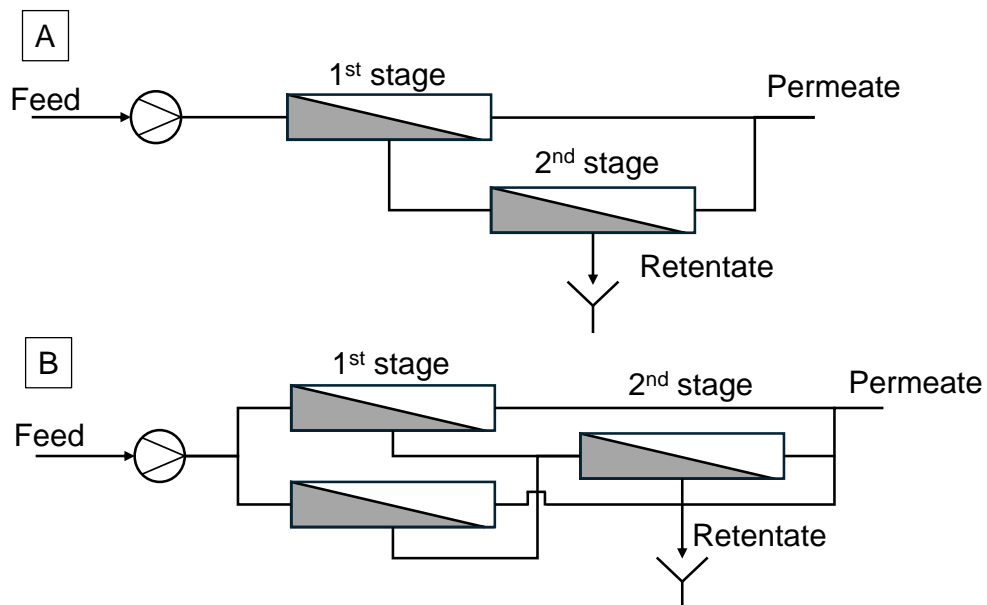


Figure 1.3: A) Simple reverse osmosis installation with retentate recycling in two stages. B) The first stage is divided into two parallel segments and the retentate is recycled through the second stage to maintain higher cross-flow velocity in the second stage.

If the cross-flow velocity is reduced, the concentration polarization across the membrane layers increases progressively for subsequent retentate stages. Additionally, due to the rejection of the permeate from the feed stream, the concentration of solutes in the rejected water increases in the retentate stages [21]. The effective concentration in the final stage, can be determined by the number of stages (n) and depending on the recovery of the stages.

$$r_{tot} = 1 - (r_{stage})^n \quad (1.2)$$

The concentration factor CF can be calculated by equation 1.3, assuming 100% membrane rejection [25].

$$CF_{tot} = \frac{1}{1 - r_{tot}} \quad (1.3)$$

To minimize the waste water production and maximize the energy recovery industrial RO plants always use several stages. Hence, scaling will occur first in the last stages of an reverse osmosis installation. In these final stages, the concentration polarization and the ionic strength are highest. This phenomenon is discussed in more detail in section 1.5.

On the other hand, the nutrients that accelerate biological growth are most concentrated in the first stages of an reverse osmosis system. Microorganisms that are attached on the feed side already metabolize the nutrients in the first stage, which means that these nutrients are no longer available in the downstream stages [26].

Besides the reverse osmosis installation setup, another key factor that influences membrane fouling is the solute content of the feed water. High organic or microbial loads lead to biofouling, while scaling is induced by high salt concentrations. Several theories and quantitative methods exist that characterize the tendency of crystals to form from the feed water or to describe crystal growth on the membrane surface [27–32].

1.2.2 Inorganic fouling - scaling

In general, scaling (i.e., the deposition of crystals) occurs on reverse osmosis membrane surfaces if the feed water reaches its saturation point of the corresponding salt on the membrane surface. One type of crystal that is often found on reverse osmosis membrane surfaces is calcite, a polymorph of the calcium carbonate salt [27–29]. Calcium carbonate can crystallize as either aragonite, vaterite or calcite polymorphs, of which calcite is the most thermodynamically favored [33]. The more saturated the feed water, the more likely it is that calcium carbonate crystals will form and negatively impact the filtration process. Thus, it is vital to know the saturation level of the feed water, which can be calculated using the ion activities for calcium carbonate ($\{Ca^{2+}\}$, $\{CO_3^{2-}\}$) and the thermodynamic solubility product K_s . The ion activities of the corresponding ions are summarized by the ion activity product (IAP). Equation 1.4 calculates the saturation index (SI) for calcium carbonate. A positive SI value indicates that the water is saturated with the corresponding polymorph.

$$SI = \log\left(\frac{\{Ca^{2+}\} \cdot \{CO_3^{2-}\}}{K_s}\right) = \log\left(\frac{IAP}{K_s}\right) \quad (1.4)$$

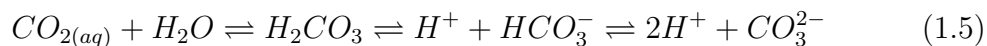
The formation of crystals on the membrane surface typically occurs in two stages,

first by the formation of primary nuclei followed by formation of highly stable secondary crystals atop these nuclei [31, 32]. When and whether the membrane surface nucleates calcite crystal growth depends largely on the crystalline state of the calcium carbonate [30]. The precipitation of CaCO_3 can be classified into two forms: the crystalline form, mainly calcite, and the amorphous form known as amorphous CaCO_3 (ACC). The ACC can contain varying amounts of adsorbed water [34], which is further classified into general ACC and monohydrated CaCO_3 (MCC) in scaling studies [31, 32, 35]. In highly saturated feed water, multiple crystal nuclei are formed rapidly and homogeneously in the cross-flowing feed water. On the other hand, if the water is less saturated, crystals nucleate more slowly and in a heterogeneous manner on the membrane surface. The higher saturation point is referred to as the saturation point of the general ACC, while the lower one, indicating heterogeneous crystallization, is known as the saturation point of the MCC [35]. Both ACC and MCC polymorphs, hence, play the role of a precursor that forms ion clusters and later the crystal nuclei [35].

The process parameters during the scale formation change if the crystals exceed a critical size or amount. They influence the SWM's hydraulic properties and affect the osmotic pressure across the membrane surface, which can lead to a decreased permeate flow, reduced salt retention, and the need for higher pump power to compensate for the pressure drop in the feed channel [36]. Due to these negative influences on the effectiveness of reverse osmosis membranes, anti-scaling treatment is a topic of active research. Among the countermeasures that are adopted to combat scaling, a distinction is made between upstream and downstream cleaning concepts [37, 38]. This topic is discussed further in Section 1.3. However, many of the problems caused by scaling could be avoided by employing an *in-situ* sensing technique that allows for the early detection of salt precipitation on reverse osmosis membrane surfaces [39].

Predicting and early sensing techniques for membrane scaling

In order to define the earliest point at which salt nuclei are formed on reverse osmosis membrane surfaces, two main approaches are known from the recent literature. One method seeks to implement early sensing systems in existing membrane modules [40]. Other methods use simulations to predict the saturation points of MCC, ACC and calcite polymorphs, which have in many cases successfully predicted the point at which crystal nuclei begin to form on membrane surfaces [28, 31, 32, 41]. An important factor to consider in these simulations is the pH-dependent equilibrium of calcite formation, which is governed by Equations 1.5 and 1.6.



The pH value of a simulated saturated feed water is compared to the measured pH value of the real feed water. In the hydrodynamic simulation of cross-flowing water, the boundary layer effect of the concentration polarization, the concentration across the reverse osmosis modules and gas exchanges with the atmosphere are taken into account. If the saturation of the corresponding polymorph is reached, the Langlier saturation index (LSI) (represented by Equation 1.7) becomes positive. In this way, pH measurements can be used to quickly and accurately predict the saturation of calcite polymorphs that promote (especially heterogeneous) crystallization on the membrane, thus making membrane operation more efficient and less prone to clogging [31, 32].

$$LSI = pH_{measured} - pH_{sat}(polymorph) \quad (1.7)$$

An important value that describes the impact of scaling on the reverse osmosis process is the induction time (t_{ind}), which refers to the time during which "measurable" crystallization impacts the reverse osmosis process [42, 43]. Equation 1.8 describes the induction period, whereas A and B are fitting parameters.

$$\log(t_{ind}) = A(SI)^{-2} + B \quad (1.8)$$

Accurately characterizing t_{ind} is often difficult, given that detection of the formation of the first crystal nuclei on the membrane, especially for SWMs, is nearly impossible. Instead, depending on the sensitivity of the measuring method and the scale of the water filtration process, the onset of membrane scaling is often first discovered via the detection of decreasing salt rejection, diminished permeability or a higher pressure drop between the feed and the retentate side of a SWM [2, 36]. Thus, in order to refine scaling detection methods, a variety of approaches have been investigated so far. One *in-situ* method detects crystal deposits on the membrane surfaces by ultrasonic time domain reflectometry (UTDR), which uses ultrasonic waves that are emitted into the feed channel and reflected by (i) the feed spacer, (ii) the membrane, and (iii) formed nuclei on the membrane surface. By measuring the time that is needed until the reflected acoustic wave arrives at the detector, case (iii) can be directly monitored [40, 44]. However, UTDR often requires a specialized membrane cell and detects the deposit formation once the flux has already begun to decline [45]. Interferences with the ultrasonic signal are to be expected if the feed water contains higher concentrations of particles that reflect, diffract or scatter the sound waves. Comparable limitations are encountered with electrical impedance spectroscopy (EIS), a sensing technique that relies on measurements of changes in the electrical properties of the membrane in the presence of crystals on the membrane surface [45]. In contrast to acoustic- and impedance-based methods, real-time image analysis provides a direct and promising method that is able to detect the onset of scaling [45, 46]. However this method is only suitable for membrane flat cells (MFC) and not for industrial SWMs. Comparable but more detailed analyses have been recently realized by integrating an optical window into an reverse osmosis MFC to

allow for Raman spectroscopy-based identification of calcite crystals [47].

Ex-situ methods provide an alternative approach to detect crystals on membrane surfaces, one of the most prominent of which is scanning electron microscopy (SEM) [28, 39, 47, 48]. Although SEM imaging can detect even the smallest crystal nuclei on the membrane surface, preparing samples for SEM analysis is far from practical for reverse osmosis membranes. In order to measure a membrane sample, the membrane first has to be dried, which complicates the sample preparation if small amounts of the feed solution remains on the membrane surface. Water evaporation during the drying process leads to a saturation and thus precipitation of the component salts, making it difficult to distinguish between precipitates that formed before or after the drying process. This problem can only be solved using cryo-SEM, which circumvents the need for sample drying but is not a commonly accessible technique for many research labs or industrial plants. Other *ex-situ* detection and identification methods available include atomic absorption spectroscopy, X-ray diffraction, grazing incidence wide angle X-ray scattering, vertical scanning interferometry and atomic force microscopy [49]. Nevertheless, these methods suffer from similar sample preparation difficulties as SEM.

To address the challenges faced by the current state of the art in membrane scaling detection, this dissertation introduces a new, highly sensitive *in-situ* fiber-based sensing technique for detecting mineral deposits. Given that commonly used reverse osmosis membranes often contain feed spacers consisting of polypropylene (PP) fibers, it is anticipated that the detection method investigated in this thesis could be easily integrated into existing membrane fabrication protocols. The employed optical fibers consist of a high refractive index core and a low refractive index cladding that enhances the total reflection in the fiber core [50]. Optical fibers are typically coated with a fluoropolymer, which, in addition to its desirable optical properties, gives fibers a smooth surface that makes them easy to install in pipes or other systems for data transfer. In order to make such fibers more sensitive to surface deposits, the fiber cladding can be removed [50–53]. Crystals with a higher refractive index scatter the light out of the optical core. The loss of transmitted light can then be detected. This method could provide an interesting approach to detect the first nuclei growth. By using such a method in membrane modules, existing crystallization theories can be refined, recoveries can be better controlled, and existing purification processes can be improved. Potentially this method will also enable the more accurate calculation of induction times.

1.2.3 Biofouling

In addition to scaling, the adhesion of microorganisms to SWMs is another prominent type of fouling, known as biofouling. Biofouling can become a significant problem if microbially degradable organic substances are accompanied by viable microorganisms in the feed water [54]. In general, biofouling occurs in three different steps:

1. The lag or adhesion phase marks the point when microorganisms are attached to parts of the SWM. The adhesion predominantly takes place in areas of low cross-flow velocity. The intersections of the feed spacers, hence, are typically the first place where microorganisms are found in SWMs [55].
2. The second period is the so-called log phase or exponential-growth phase [56]. During this phase, the microorganisms are growing and are forming clusters, which can interact with each other by quorum sensing. Furthermore, the microorganisms are expressing extracellular polysaccharides and proteins in order to protect themselves from environmental conditions. This threshold of interference marks the latest point at which the membrane can be successfully cleaned [57]. As more extracellular substances are produced to protect the microorganisms, chemical or mechanical removal of the biofilm becomes increasingly difficult.

The effects of biofilm formation in a reverse osmosis water purification system become apparent during this period. The first sign is that the pressure drop in the feed channel increases due to the reduced cross-sectional flow [58–60]. In this situation, the reverse osmosis pump requires more energy to maintain the pressure across all SWMs. Later, the biofilm will also attach to the membrane surface, which blocks the free membrane space and increases the filter resistance. As a consequence, the trans-membrane pressure and the permeate flux decrease [58].

3. In the last period of biofouling, larger parts of the biofilm begin to detach from the surfaces of the SWM due to increasing shear stresses under cross-flow conditions. As a result, biomass growth and the detachment of biomass from the membrane surface reach similar rates. The feed spacer experiences higher flow resistance, which may cause the feed spacer to protrude out of the SWM, thus destroying the SWM. The longer the biofilm remains attached to the membrane surface, and depending on the membrane material, biodegradation of the membrane itself may become possible [61]. Leakages in the membrane could then lead to contamination of the permeate with the products of biofouling, which may contain human pathogenic bacteria [62, 63].

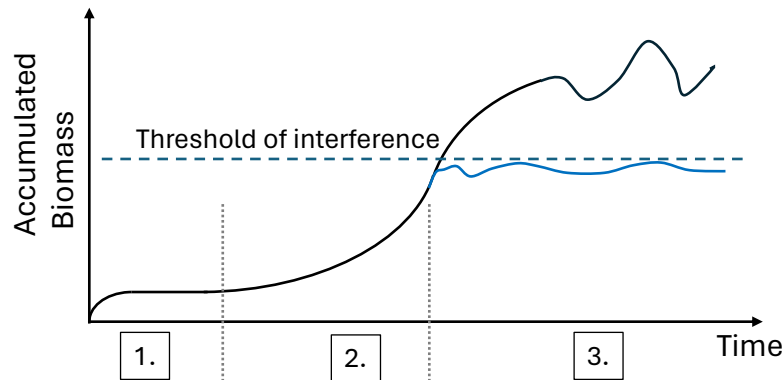


Figure 1.4: Time-dependent biofouling showing the typical phases of formation: 1. lag/accumulation phase, 2. logarithmic or log phase, 3. plateau phase. Adapted from Flemming *et al.* [57].

The potential risks of biofouling for reverse osmosis membranes and the ubiquitous presence of microorganisms in feed water make the treatment of biofouling and early detection essential. Early detection is, however, not only an issue in reverse osmosis membrane systems since biofouling harms various industrial processes such as cooling/heating systems or health-relevant surfaces. Hence, the detection mechanisms that could play a role can not only be found in the reverse osmosis literature.

Usually, biofilms may be detected by taking water samples for an extended period and culturing the microorganisms in the water to define hot spots for biofouling via detection of the number of colony forming units (CFU) [64]. However, it is often difficult to account for the microorganism that are assembled in the depths of the biofilm [64]. Therefore, counting microorganisms via fluorescence microscopy to determine the total microbial cell count often leads to a more realistic picture of microbial contamination. *In-line* counting techniques such as flow cytometry (FC) can be used to determine the total cell number (TCC) [65]. In reverse osmosis membrane systems, flow cytometers must be installed separately to monitor both the feed and the retentate flow with the aim of detecting cell attachment and detachment. Other techniques measure the total adenosine triphosphate (ATP) concentration or balance the amount of total organic carbon in order to monitor biofouling via the accumulated nutrients in a membrane system.

Since biofilms grow on surfaces, past methods to monitor biofouling used surfaces as a target to measure the kinetics of biofouling formation and in order to monitor cleaning efficacy [64, 66].

Several previous approaches used the biofilm-induced changes to the resistance of metal surfaces to monitor biofouling [67–69]. While such methods are still used today with commercially available sensors, electrochemical approaches for biofilm detection in SWMs are impractical because there are no metal surfaces in SWM, making it impossible to integrate the existing sensors in SWM. Moreover, the application of UTDR, as well as optical imaging and online refractometers, have been studied to detect biological growth on surfaces [64, 70, 71]. However, the most promising

approaches to creating a detection system specific for reverse osmosis conditions use the fouling simulators developed by Vrouwenvelder *et al.* [55, 58, 59, 64, 72]. These simulators are small membrane flat cells adapted to the flow conditions in real SWMs [73]. The biofouling itself is not detected directly; instead, this is done so indirectly by monitoring the increasing feed channel pressure drop (FCP), which is rising due to blocking the feed channel with biomass. The fouling simulator is installed in a bypass next to the first SWM, where the nutrient concentrations are highest and biofilm will grow first.

While such methods have proven effective in many cases, a more direct way of detecting biofouling in SWMs remains desirable. Thus far, sensing apparatuses that could be integrated into the feed spacers and that would be able to measure the biofilm formation on the feed spacer structure have not yet been developed. Since the feed spacer is made of fibers, optical fiber sensors are in principle easy to integrate into the spacers. Recent studies have shown that optical fibers can be incorporated into industrial water apparatuses to detect microorganisms via backscattering of light [71, 74, 75]. However, in these setups, the fibers must be arranged perpendicularly to the sensed surface (Figure 1.5A), which is not possible to implement with membrane and spacer surfaces in SWMs. Alternatively, Zhong *et al.* validated a fiber setup to monitor algae biofilm growth that uses polymeric optical fibers with a cut "window" in the fiber cross section [76] (Figure 1.5B). Fiber setups that measure color changes in the cross-flowing media via evanescent fields have also been tested successfully [77]. This type of detection is made possible by partially removing the fiber cladding to produce a sensitized zone (Figure 1.5B). Such an attenuated total reflection (ATR) setup was also validated for biofilm detection by several groups [78–81].

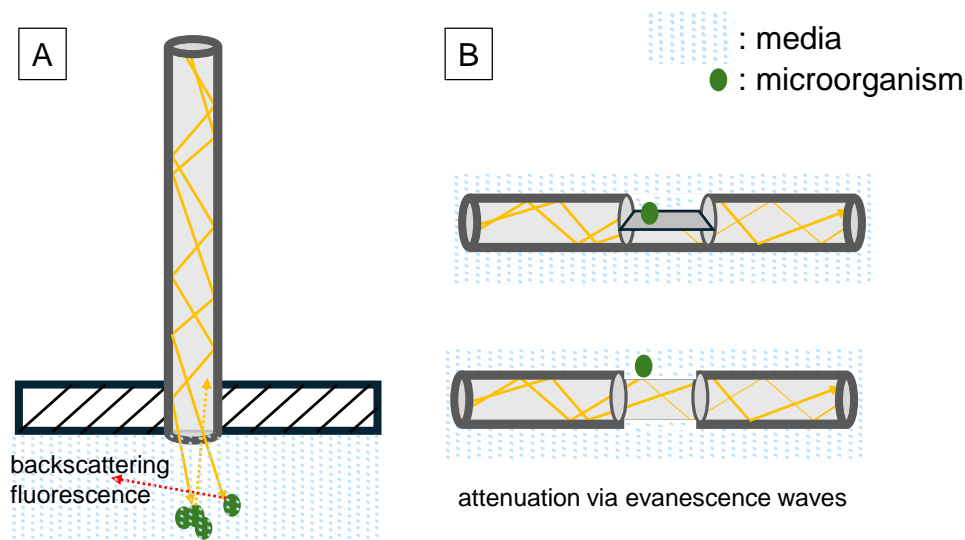


Figure 1.5: Schematic depicting the principles of fiber optic biofilm sensors. A) Orthogonal fiber setup. Microorganisms are detected via backscattered reflected or emitted light. B) The fiber is immersed into the medium, and the fiber cladding is partially removed. Microorganisms are detected by the attenuation of evanescent waves.

However, studies that investigate a possible implementation of the fiber ATR setup into reverse osmosis feed spacers so far have not been developed. Thus, in addition to the early detection of scaling via de-clad fibers, the ATR fiber setup for biofouling detection is the second sensing principle to be demonstrated in this dissertation.

1.3 Antifouling strategies

The antifouling strategies used to date to prevent the negative effects of fouling in SWMs have been designed to counteract primarily one type of fouling, thus leaving the SWMs vulnerable to other types of fouling that can evade detection. Furthermore, only mitigating one type of fouling (e.g., scaling or biofouling produced by a particular microorganism) can inadvertently lead to the acceleration of other types of fouling. Thus, it is necessary to use the developed fiber optic sensing technology to effectively and simultaneously target all types of fouling occurring at the membrane surface.

Anti-scaling strategies

Anti-scaling strategies can be divided into two different approaches. With the first approach, the saturation index is influenced to avoid any nuclei formation on the membranes. Since most crystals on the membrane surface consist of carbonate salts, a pH adjustment significantly reduces the saturation indexes of all polymorphs. Hence, the precursors for secondary (homogeneous and heterogeneous) as well as primary crystallization can be avoided [82]. One method to lower the pH value of the feed water and thus lower the saturation index is CO₂ injection into the feed water. The diluted CO₂ forms carboxylic acid and therefore lowers the pH value [83]. Alternatively, an ion exchanger can be used to swap calcium ions in the feed water for sodium ions, which also reduces the saturation index of calcium carbonate polymorphs [84].

The second approach only reduces the effects of crystallization on the reverse osmosis performance. By adding anti-scalants to the feed water, the formation of nuclei can be reduced by competing complexation mechanisms that decrease the concentration of free metal ions, such as calcium, in the feed water. [85]. Other effects of the dosed anti-scalants stabilize the existing crystal nuclei either via chelation [86], or the anti-scalant adsorbs onto the crystal nucleus to stabilize it via ionic or steric interactions [87]. Other proposed mechanisms describe a crystal lattice distortion, which means a change of the crystal morphology, or the inhibition by antiscalants of cluster formation, the process that precedes and is necessary for the formation of nuclei [88].

Commercially available anti-scalants can be classified as either phosphorous-based or phosphorous-free anti-scalants [88, 89]. Phosphorous-based anti-scalants are comprised of either phosphates or phosphonates. A well-known and frequently used phosphate-based anti-scalant is sodium hexa-meta-phosphate (SHMP), which is

thought to inhibit crystal formation via chelation, crystal lattice distortion and cluster inhibition mechanisms [88, 90, 91]. On the other hand phosphorous-free anti-scalants consist of organic polymers such as poly (acrylic acid) (PAA), poly(methacrylic acid) (PMAA) or poly(maleic acid) (PMA) [92]. The phosphorous free anti-scalants are reducing the effects of scaling by chelation, adsorption onto nuclei, crystal lattice distortion or by inhibiting the nuclei formation [87].

While anti-scalants mitigate the effects of crystallization on the reverse osmosis plant's performance, they can also have negative effects on the environment [93, 94] due to the fact that they persist in the retentate of the reverse osmosis plant, thus entering into the municipal waste water treatment and surrounding aquatic environment. Polymer-based antiscalants are assumed to be almost non-biodegradable due to their high resistance to chemical and thermal decomposition [87]. In contrast, it is assumed that some phosphorous-based anti-scalants are naturally broken down into components that serve as nutrients for several microorganisms and thus promote further biofilm growth in the reverse osmosis filtration system [92, 95].

Monitoring techniques that allow controlled dosing of anti-scalants to mitigate microorganism and crystal growth on spacers and membranes could enhance the effectiveness of the widely used anti-scalants in reverse osmosis water treatment. Using such monitoring techniques, the precise effect of the dosed anti-scalant on crystal growth in reverse osmosis membrane systems could be better understood. Furthermore, the anti-scalants themselves could be redesigned and refined to suppress scaling more effectively by avoiding degradation products that are nutritious for microorganisms. Advanced oxidation processes hold promise as an approach to degrade anti-scalants in the retentate before they can enter the aquatic environment [93, 94]. Another approach could be a defined combination of anti-scalant dosing and corresponding anti-biofouling strategies to prevent scaling and biofouling simultaneously. However, more research is needed to establish effective treatment of anti-scalants in the retentate of reverse osmosis plants.

Anti-biofouling strategies

Given the ubiquity of biofouling in reverse osmosis membranes, methods for pretreating the feed water or disinfecting the membrane itself have been important topics of research for many years [12, 54]. From this research, two primary anti-biofouling strategies have emerged:

1. Pretreatment of the feed water.

The pretreatment of the feed water describes the disinfection of the feed water or the nutrient reduction in the feed water. The sanitation can be performed by dosing disinfectants into the feed water or by filtering the feed water with an ultrafiltration membrane (UF) before the water is pumped through the reverse osmosis membrane [96]. In order to remove fine organic particles or algae cells, the use of dissolved air flotation (DAF) has shown promising results in the case of sea water reverse osmosis [97]. Pilot plants in Spain, Chile, Singapore

and the Middle East have tackled algae blooms by using a pretreatment that combines DAF with microfiltration (MF). The DAF can reduce the biomass in the following membrane modules without cell autolysis, thus significantly reducing nutrients in subsequent process steps and by this the production of EPS by microorganisms [98].

Other methods take the approach of reducing the amount of nutrients, and hence of assimilable organic carbon and phosphorous, in the feed water to mitigate biofouling. The techniques that come into question here are coagulation and adsorption. Regarding the coagulation it is important that the dosed anti-scalants are either dosed after the upstream removal of nutrients or the anti-scalants are adapted to the pretreatment so that they are not removed [61]. Another method relies on the adsorption of nutrients by granular activated carbon (GAC), which was successfully demonstrated by several groups [61, 99, 100].

Finally, a type of pretreatment in which viable microorganisms are physically inactivated by irradiating the feed water by UV-LEDs has gained research interest in recent years. A key advantage of this approach over other irradiation-based pretreatment strategies that use, for example, mercury lamps lies in the fact that UV-LEDs are much more energy-efficient. For example, Sperle *et al.* observed a slowing of biomass accumulation in the feed channel and changes in the microbial of the biofilm after irradiating the feed water at 254 nm [9].

2. Sanitation of the reverse osmosis membrane

This second approach is not aimed at preventing or slowing membrane biofouling, but rather removes the formed biofilm with frequent cleaning steps in order to minimize fouling effects on the reverse osmosis performance parameters.

One way in which commercially available membranes are cleaned is by pumping hot water ($60^\circ\text{C} < T < 85^\circ\text{C}$) through the SWMs to inactivate the microorganisms, which requires that the membranes be stable against the high temperatures used. However, it is often the case that the permeability of the SWMs is reduced after the first heat treatment. Hence, these SWM require higher feed pressures and, thereby, a higher energy consumption to produce the same amount of permeate with the same amount of membrane area [101, 102]. Furthermore, while the hot water is pumped through the SWM it has to be purified and the TMP is required to be as low as possible [101]. Thus, while heat treatment is effective to sanitize reverse osmosis membrane surfaces, the energy consumption and the technical requirements for such a sanitation makes this method cost intensive and less practical for reverse osmosis membrane users.

Sanitation, which can be achieved using disinfectants rather than heat, has been a key focus of reverse osmosis membrane research for a long time [12, 103]. The current focus of ongoing research is the high oxidative potential of disin-

fectants, which typically degrades the lipids and proteins of organic matter. However, a significant drawback of oxidative disinfection methods is that, since the molecular structure of the essential PA layer of reverse osmosis membranes closely resembles proteins, the PA layer is also degraded by disinfectants, leading to a loss of the reverse osmosis membranes' rejection properties. Currently, research is being directed towards developing membrane materials that are more resistant to one or more disinfectants [104–106] and towards investigating the membrane degradation process to gain a better understanding of the mechanisms involved [107–112]. This understanding will help in defining process conditions aimed at minimizing membrane degradation during sanitation. Consequently, a break-even point for the membrane lifetime can be established. The lifetime of the membrane is then determined by either a loss of membrane integrity due to biofouling or oxidative deterioration [113]. Therefore, this dissertation focuses on the detection methods for oxidative membrane damages and the matrix of oxidative disinfectants, with a special focus on chlorine dioxide.

1.4 Oxidative membrane degradation - the second Achilles' heel of reverse osmosis membranes

Understanding how and when oxidative decomposition of the PA layer of reverse osmosis membranes takes place is the first research gap that is addressed by the third chapter of this dissertation, which compares various online and offline measuring methods. This comparison aims to improve our understanding of membrane degradation and to show which techniques are most sensitive at different stages of membrane degradation.

The user of a reverse osmosis system only recognizes the loss of rejection and performance properties of the reverse osmosis membranes when they are in operation. However, such changes in the online measured parameters (see Section 1.5) are only detectable after significant fouling has already occurred [111]. The measuring techniques that play a crucial role in detecting the initial changes in the reverse osmosis membrane properties are those that measure chemically induced changes of the PA layer of the membrane [12, 112]. In comparison, the supporting PES layer remains unaffected by the chemically induced oxidation reactions [107]. The most widely used techniques to detect chemical changes in the PA layer are attenuated total reflection (ATR) Fourier transformed infrared spectroscopy (FTIR) or the Fujiwara test [114–117]. The Fujiwara test is a dye test that qualitatively indicates whether the PA layer of the RO membrane is halogenated [117]. However, recent studies have shown that the Fujiwara test is less sensitive in detecting chlorination reactions than ATR-FTIR. To the best of my knowledge, ATR-FTIR analyses have been primarily used in a qualitative manner. Semi-quantitative approaches are not yet widely used to detect chemical changes and to categorize membranes based on the extent of their chemical changes [117]. More advanced techniques that al-

low for direct quantitative measurements of chemical changes include, for example, X-ray photoelectron spectroscopy [109, 118]. However, this method requires more time and an expensive spectrometer, which limits the amount of samples that can be measured. To assess the effectiveness of methods to assess membrane integrity or that study their sensitivity, reverse osmosis membranes were to the best of my knowledge exposed to three different disinfectants in all the studies: free chlorine, chlorine dioxide, and monochloramine.

The most studied disinfectant is free chlorine, which when dissolved in water is found most commonly in the form of either hypochlorite and hypochlorous acid. Hypochlorous acid is most prevalent in water with a pH above 7.53, while hypochlorite predominates in water with a pH below 7.53 [111]. Both species react differently with the PA layer. The commonly cited hypothesis suggests that the PA layer is chlorinated by both species, starting with the nitrogen atom and then proceeding to the aromatic ring. Chlorinating the nitrogen atom results in partial charge of the amide bond, which likely facilitates a nucleophile attack of OH ions to the carbon atom of the amide bond and then hydrolytic cleavage of the PA chains. In neutral or acidic conditions, hydrolytic cleavage is less likely due to the lower concentration of OH ions. When free chlorine reacts with the PA layer of the membrane, the mechanical properties of the PA layer change, which can lead to detachment, swelling, or tightening of this layer that in turn affects membrane performance [111]. The resultant morphological changes in the PA layer are detectable by SEM imaging [112, 119, 120]. Nevertheless, it is difficult to identify changes in the membrane surface that are responsible for the performance loss of the membrane.

The second research gap that is addressed in the third chapter of this dissertation is the chemical complexity of the chlorine dioxide manufacturing processes with regard to the caused membrane damages. The solutions of technical chlorine dioxide, used for water disinfection, are commonly produced by acidifying a sodium chlorite solution or by oxidizing chlorite with hydrogen peroxide, persulfate, or hypochlorite [138], resulting in the main by products, free chlorine, persulfate, chlorite, chloride, chlorate and sulfate. In addition to the various manufacturing processes, which make it difficult to compare the chlorine dioxide concerning membrane compatibility, there are significantly fewer studies overall that have investigated the membrane compatibility of chlorine dioxide. To the best of my knowledge, only purified chlorine dioxide with acidic pH value was used in recent studies to evaluate the effects of chlorine dioxide on the reverse osmosis membrane's process performance [103, 122, 123]. Since this is far from practical use, this dissertation investigates the individual components of a chlorine dioxide solution with the aim to define the chlorine dioxide manufacturing processes that have the least impact on the reverse osmosis membrane properties and could therefore be the most attractive for preserving the membrane itself during treatment. Furthermore, the influence of mechanical stress is investigated during the disinfection by varying process parameters of the filtration in a way that mimics real usage conditions.

1.5 Evaluation of reverse osmosis process performance

To describe the process performance of reverse osmosis membranes, there are three main parameters that can be calculated:

1. **The selectivity** describes the ability of the membrane to reject different solutes from the feed water. The most commonly used parameter is the salt rejection R [124, 125], the inverse of which is the salt passage SP . These parameters are defined in Equation 1.9. The salt rejection is the parameter most often calculated for cross-flow conditions in SWMs or membrane flat cells.

$$R = 100\% - \frac{c_{perm}}{c_{feed}} \cdot 100\% = 100\% - SP \quad (1.9)$$

Other selectivity parameters used are the rejection of the total organic carbon (TOC), microorganisms, viruses or specific ions [126, 127]. In order to simplify the calculation, the concentration of all diluted ions c is often replaced by the corresponding conductivities [128]. Moreover, if the membrane is used in a dead-end mode, the effects of concentration polarization have to be taken into account to accurately calculate the salt rejection. Concentration polarization (CP) is a boundary layer effect that describes the accumulation of the rejected ions c_m on the rejecting surface, in this case the reverse osmosis membrane. The Figure 1.6 sketches the different scenarios that show the different cases for the concentration polarization.

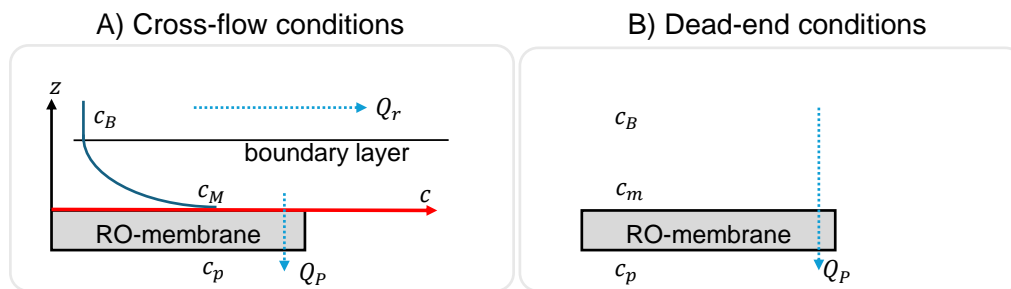


Figure 1.6: Scenarios for the mass transport at the surface of and through the reverse osmosis membrane. A) Cross-flow conditions present in SWMs and membrane flat cells. B) Dead-end conditions. The relevant parameters that are needed to describe the CP is the concentration of the dissolved ions in the bulk (c_B), the concentration of the dissolved ions in the permeate (c_p), the permeate stream Q_P and the retentate stream (Q_r).

In the case of dead-end filtration, two different transport mechanisms are relevant for the calculation of the accumulation of the rejected solutes from the feed water. The first (diffusion) can act against the permeation velocity v_P that can be calculated by the membrane area A and the permeate stream Q_P

as in Equation 1.10. The second one is the mass transport of water and ions through the membrane.

$$v_P = \frac{Q_P}{A} \quad (1.10)$$

The general equation for the concentration polarization effect on the concentration gradient is defined by Equation 1.11. Whereas D is the diffusion coefficient for the rejected ions and z is the distance to the membrane surface.

$$c(z) = c_B + \frac{v_P}{D} \cdot c_m \cdot \exp(-v_P \cdot \frac{z}{D}) \quad (1.11)$$

If no phase transition of the rejected ions takes place, no crystals form a mass balance of ions in there boundary layer leads to the following differential equation 1.12. Note here that the concentration of the dissolved ions in the permeate is $c_P = (100\% - R) \cdot c_M$.

$$\begin{aligned} \frac{dc_e}{dt} = v_P \cdot c_B - v_P \cdot c_M \cdot (100\% - R) &\implies \int 1dc_m = \int v_P \cdot c_B - v_P \cdot c_P dt \\ &\implies c_m = v_P \cdot t(c_B - c_P) \end{aligned} \quad (1.12)$$

The combination of the Equations 1.11 and 1.12 leads to Equation 1.13 respectively that the boundary condition $z = 0$ for the calculation of the concentration at the membrane surface.

$$\begin{aligned} c(z = 0) = c_M = c_B + \frac{v_P}{D} \cdot c_m \cdot \exp(-v_P \cdot \frac{z}{D}) \\ = c_B + \frac{v_P^2}{D} \cdot t \cdot (c_B - c_P) \end{aligned} \quad (1.13)$$

The calculations and theories for scaling, as well as the salt rejection in the case of an dead-end filtration, were first published by Mitrouli *et al.* [129]. The rejection capacity of the membrane is then not calculated by the concentration of the ions in the cross-flowing bulk c_B or c_F , but rather by the concentration of ions on the direct membrane surface c_M . These calculations are used in the third chapter of this thesis to validate the methylene blue (MB) test, a dye test that allows to better visualize which membrane areas suffer from a loss in the rejection capacity.

2. **The productivity** of an reverse osmosis membrane can be defined by the flux J_W , the quotient of the permeate stream Q_P and the membrane area A in use.

$$J_W = \frac{Q_P}{A} \quad (1.14)$$

To normalize the flux with feed pressure (p_F), permeate pressure (p_P) and feed osmotic pressure (π), the permeability (P_W) is a key parameter for any membrane that can be affected by membrane fouling and deterioration, by changes in membrane surface charge due to pH variations [130, 131] or due to mechanical and chemical defects in the membrane's surface polymers at the surface.

$$P_W = \frac{Q_P}{A \cdot (p_F - (p_P + \pi))} \quad (1.15)$$

The osmotic pressure is only calculated for the feed side of the membrane using van't Hoff's equation for simplification. In the permeate stream most of the ions are rejected, therefore permeate osmotic pressure is near to zero. However, the effects of concentration polarization have not yet been considered when determining the productivity of the membrane. This can be achieved by calculating the factor β that represents the amount of ionic strength that is higher at the membrane surface compared to the cross-flowing bulk. In this dissertation, the factor β is calculated for all chapters, including for cross-flow experiments, by empirical equations following the methods reported by Koustglou *et al.* and Crittenden *et al.* [124, 132]. While these formulas take the flow regime and the thickness of a mean boundary layer into account, local effects of different cross-flow conditions caused by the feed spacer geometries are not considered.

3. **The hydraulics** of an reverse osmosis plant are important, since all MFCs as well as SWMs have an hydraulic resistance that is mainly caused by the thin feed spacers in the feed channels. These feed channels mix the bulk water flowing across the membrane and reduce concentration polarization on a macroscopic level. The pressure drop in the feed channel (FCP) decreases, especially at the feed spacer intersections, depending on the feed spacer's geometry (Figure 1.7). According to Schock & Miquel, as well as according to the law of Hagen-Poiseuille, a theoretical FCP can be calculated as shown in Equation 1.16 (where p_F and p_R represent the osmotic pressures of the feed and retentate, respectively) to validate the properties of a MFC and ensure it shows similar hydrodynamic properties to that of an SWM [72, 133, 134]. All membrane flat cells that have been used in this dissertation have been validated in this way before the experiments were executed.

$$FCP = p_F - p_R \quad (1.16)$$

While feed spacers are effective in reducing concentration polarization on a larger scale, they also result in varying flow velocities at a microscopic level [135]. As a result, shear rates are diminished at the flow shadows of the feed spacer intersections, creating favorable conditions for the accumulation of microorganisms. The reduced cross-flow velocities also have an impact on the concentration polarization. Both effects influence where fouling tends to occur in reverse osmosis modules.

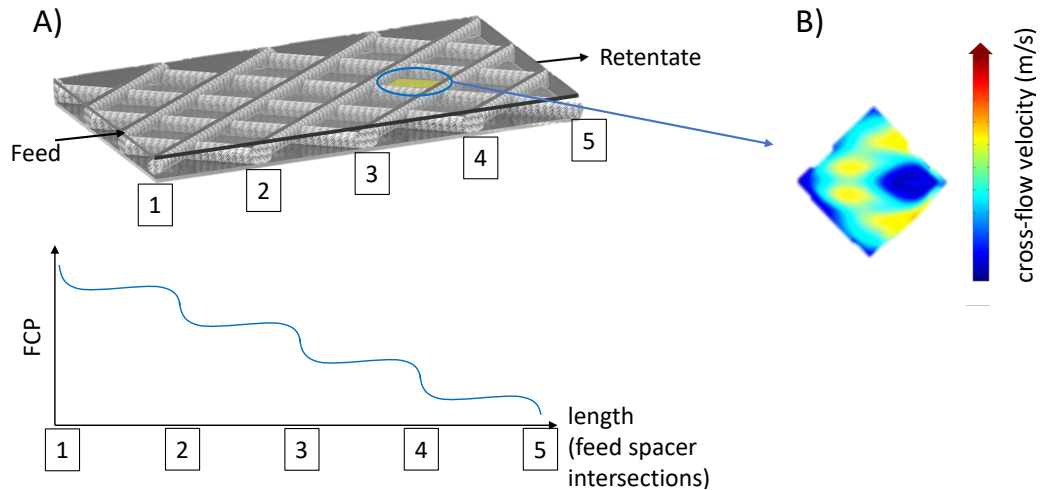


Figure 1.7: A) section of a spacer filled feed channel with the typical feed spacer crossings and the increased pressure drops at the feed spacer crossings. B) flow velocities in a feed spacer square. The graphic is adapted from the results of Picioreanu *et al.* [135]

If fouling or scaling occurs in the feed channel, the available space for water to pass through decreases, leading to a higher FCP. In industrial reverse osmosis plants with SWMs installed in series, the decreasing pressure causes lower feed pressures in the subsequent SWMs, resulting in a reduced permeate flux in those modules on the retentate side. Higher pump power levels may counteract this increased FCP until reaching the maximum feed pressure. Therefore, monitoring the required pump power is another possibility for assessing changes in hydraulic properties in an automated reverse osmosis system.

All online measured process parameters of the last three sections may change if fouling or membrane degradation occurs on the membrane surface. The parameters and their order of change depend on the type of fouling and membrane degradation.

2 Objective of this thesis

In the previous chapter, several issues regarding the detection and treatment of fouling in reverse osmosis filtration setups were discussed. The work presented in the subsequent three chapters addresses these challenges using an application-focused scientific approach.

The three main objectives of this thesis are illustrated in Figure 2.1, in line with the publications upon which this cumulative dissertation is based.

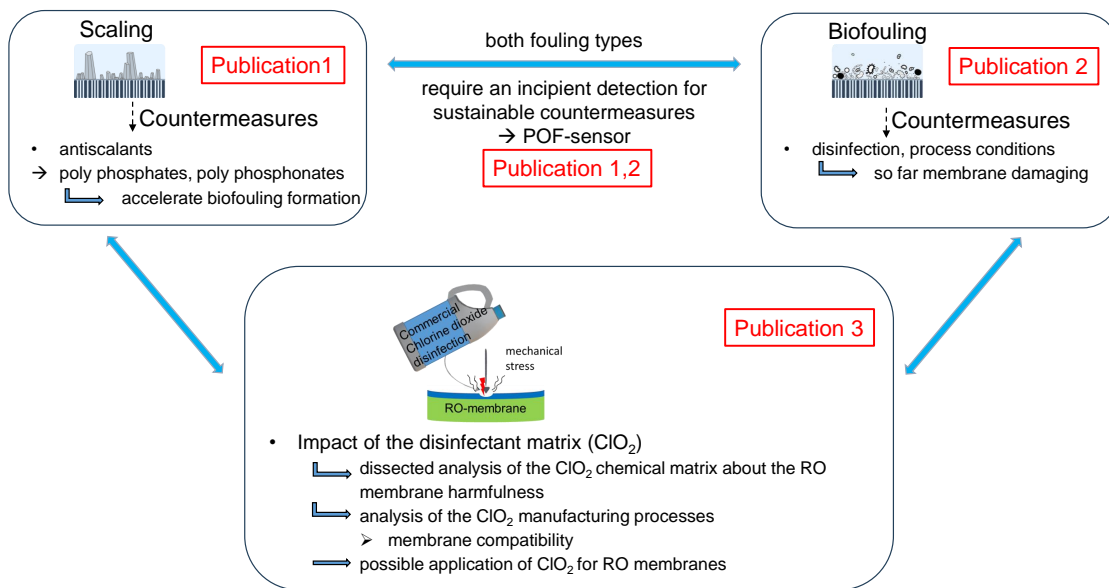


Figure 2.1: Visualization of the main objectives and their relationship

So far, no *in-situ* fouling sensors are readily available that can detect both scaling and biofouling in single wound modules (SWMs). Thus, on-site anti-fouling treatment is primarily limited to preventative countermeasures, which is less sustainable than an on-point treatment driven by early sensing. Regarding the countermeasures, biocides do indeed protect the RO membrane from biofouling, oxidative damage can still occur to the polyaramide (PA) layer of the RO membrane, which can be fatal for RO filtration systems.

In this context, this thesis aims to develop and demonstrate the application of optical fiber sensors that can be used in SWMs to detect the onset of membrane fouling, thus allowing better optimized treatment conditions. Optical fiber sensors were installed and tested in a RO pilot plant, and the data collected from these sensors was rationalized by existing fouling formation theories. Moreover, the sensors were used to compare different anti-fouling treatment strategies against commonly used biocidal countermeasures. Through these comparative investigations, the membrane-damaging components of a commercially available anti-fouling chlorine dioxide solution were identified. By determining the process conditions that

are least likely to lead to membrane damage, an approach is devised in which otherwise membrane-damaging disinfectants can be used to feasibly treat fouling on RO membranes. Going forward, membrane scaling and biofouling can be counteracted using the approach presented herein by combining biocides with frequently used antiscalants and *in-situ* early detection technology.

3 Results

The results which mark the progress of this cumulative dissertation are all research papers that are published individually in different journals.

An overview of the publications is displayed in table 3.1. The full copies can be found in this result section with the permission of the individual journals.

Table 3.1: Overview of the three publications including title, major objectives, methods and data evaluation and main statements

publication no.	1	2	3
Publication title	CaCO ₃ deposits in reverse osmosis Part III – Incipient Scaling detection via polymer optical fiber sensors. Comparison to hydrochemical prediction and image analytical methods	Incipient biofouling detection via fiber optical sensing and image analysis in reverse osmosis processes	Analytical characterization of damage in reverse osmosis membranes caused by components of a chlorine dioxide matrix
Major objectives	Incipient Scaling detection via POFs and image analytical methods and evaluation of the detection <i>ex-situ</i> and <i>in-situ</i> with several crystals and in presence of antiscalants.	Incipient biofouling detection on feed spacers and membranes by POFs and image analytical methods. Use of pulsatile cross-flow conditions to retard the fouling occurrence.	Evaluation of the damaging potential of the chlorine dioxide matrix for RO membranes. Enhancement in disinfection processes for RO membrane systems. Comparison of several analytical methods that detect membrane integrity.
Methods and data evaluation	Demonstration of the POFs function on early scaling detection <ul style="list-style-type: none"> • Introduction of the RO system with all sensors and detection capacities • Proof of hydrochemical simulations using a practical RO plant. • Use of two different experimental setups to saturate the feed water in order to accelerate the scaling on the membrane surface. 	Demonstration of the POF as biofouling sensor <ul style="list-style-type: none"> • Adaption of the RO setup to biofouling experiments • Evaluation of different POF installation and manufacturing methods for the POF's sensor zones. • Use of a standardized method to accelerate the biological growth in the membrane module. 	Impact of chlorine dioxide matrix components on RO membrane damages. <ul style="list-style-type: none"> • Improvement of the methylene blue (MB) test • Using peak ratios for the evaluation of ATF-FTIR spectras • Cross-comparison of ATR-FTIR, MB-test, XPS and SEM analytics
Main statements	<ul style="list-style-type: none"> • POFs and image analysis are capable of detecting several forms of membrane scaling • The POFs stand out as an early detection method that is capable of differentiating between heterogeneous and homogeneous crystallization. • POF's signals react on the presence of antiscalants in supersaturated salt solutions. • pH-measurements in the feed and retentate give an indication of the precipitation potential if they are combined with hydrochemical simulations. 	<ul style="list-style-type: none"> • POFs and image analytical methods can detect incipient biofouling formation on feed spacers and RO membranes. • POFs detect the first accumulation of MOs on their surfaces. • The best cross validation of the sensor principle is given by the TOC accumulation in the feed channel. • The cleaning efficacy of pulsatile crossflow can be monitored by the POFs. • Color changes of the membrane can be monitored automatically with pearson correlations and give a cross-reference for biofouling in membrane systems 	<ul style="list-style-type: none"> • The manufacturing process of chlorine dioxide is crucial for the chlorine dioxide's membrane-damaging potential on RO membranes. • The membrane damaging potential for the possible components of the chlorine dioxide matrix can be determined in an ascending order: chlorite<persulfate<purified chlorine dioxide<free chlorine. Chlorate, sulfate and chloride do not damage RO membranes. • Image analytical enhancements can improve the MB-test • The MB-test and results from ATR-FTIR are comparable in quantitative terms. SEM analysis and XPS measurements corroborate the findings of the MB tests and FTIR analyses regarding the observed membrane damage. • The best disinfection process for RO membranes combines low concentrations of membrane damaging by-products with low mechanical stress at neutral pH.

3.1 Incipient scaling detection via polymer optical fiber sensors. Comparison to hydrochemical prediction and image analytical methods

The research article “CaCO₃ deposits in reverse osmosis: Part III – Incipient scaling detection via polymer optical fiber sensors. “Comparison to hydrochemical prediction and image analytical methods” was published in “*BrewingScience*” in 2023 (doi: 10.23763/BrSc23-03hager). This article is a shared-first-author paper by H. Oesinghaus and S. Hager. H. Oesinghaus performed the experiments, analyzed and interpreted the data, developed the image analysis method, co-wrote the original manuscript, and revised the manuscript based on the reviewers’ comments.

Currently, no robust sensing system exists that can reliably detect the early stages of scaling in RO setups. Methods reported in the literature suffer from cross-sensitivities to other events in RO systems and, therefore, do not provide a reliable signal that enables precise monitoring of crystallization in SWMs. Furthermore, to the best of my knowledge, no approach has yet been developed that directly measures the effects of antiscalants on nuclei formation and crystal growth. While some studies have reported camera setups that provide a direct image of crystal growth on RO membranes installed in flat cells [45, 136, 137], methods capable of automatically identifying crystals on the membrane surface or measuring the surface area covered by the crystals have not yet been demonstrated.

To address these challenges, the first publication of this cumulative dissertation provides new sensing techniques that utilize polymer optical fibers (POFs) and image analytical methods for monitoring crystal growth on RO membranes. Both methods are compared with state-of-the-art online monitoring techniques that measure important membrane parameters such as permeability, salt passage, feed channel pressure drop, and changes in pH values. In addition, the new sensing methods are validated by hydrochemical simulations that take into account the effect of different precursors on both heterogeneous and homogeneous crystallization processes. Using these simulations, it is shown that a decrease in transmission of the POFs by $7\pm 3\%$ signals the onset of heterogeneous crystallization, and that more significant transmission losses indicate homogeneous crystallization in the RO system. It is also shown that the crystals detected by the POF monitoring apparatus are primarily comprised of CaCO₃, CaSO₄, BaSO₄, and SrSO₄. However, detecting CaSO₄ is more difficult, due to the tendency of this mineral to form single crystals that cover only a small surface area of the POFs. Experiments with supersaturated CaCO₃ and different concentrations of a phosphate-containing antiscalant demonstrate that POFs can detect changes in the time series of suppressed crystallization solutions.

The work presented in this chapter represents a milestone in scaling detection and may pave the way for better understanding of crystallization processes in RO Systems.

Published manuscript

Authors: Simon Hager^{*a)}, Helge Oesinghaus^{*a)}, Alexander Bachmann^{b)}, Martin Meinardus^{c)}, Thomas Hofmann^{a)}, Rainer Engelbrecht^{b)}, and Karl Glas^{a)}

a) Water Systems Engineering, Chair of Food Chemistry and Molecular Sensory Science, TUM School of Life Sciences, Technische Universität München, Maximus-von-Imhof-Forum 2, 85354 Freising, Germany

b) Polymer Optical Fiber Application Center (POF AC), Technische Hochschule Nürnberg Georg Simon Ohm, Wassertorstraße 10, 90489 Nuremberg, Germany

c) Grünbeck Wasseraufbereitung GmbH, Josef-Grünbeck-Straße 1, 89420 Höchstädt a.d. Donau, Germany

corresponding author: helge.oesinghaus@tum.de

*These authors contributed equally to this publication.

3.1.1 Abstract

Reverse Osmosis (RO) is a widely used technology for water treatment in the beverage industry to produce brewing water, process water or tap water. The weak points of RO-membrane filtration are membrane degradation due to oxidative water constituents or membrane fouling in the difficult-to-clean, spacer-filled feed channel. The fouling can be distinguished into two main categories. The first one is caused by feed waters with a high organic and microbial load. The second type of fouling is triggered by supersaturated salt solutions, which leads to the precipitation of salts on the membrane surface. Both fouling types are destroying spiral wound RO-modules if they are not detected in an early stage. This work presents and validates a new optical online detection method via polymer optical fibers (POF) for inorganic fouling as CaCO_3 , CaSO_4 , BaSO_4 , SrSO_4 . The new detection method is tested by three experimental setups and compared with common prediction and detection methods such as saturation calculation, measurement of salt rejection, permeability, and the pressure drop in the feed channel. In addition to conventional online analysis methods for detecting deposits in reverse osmosis systems, this study presents an image analysis method that provides reliable evidence of POF sensor operation. The POF sensor is able to detect incipient crystal formation during the RO process. This gives this study the opportunity to discuss current crystallisation theories such as the induction time theory and the role of monohydrated calcium carbonate (MCC) as a precursor in the formation of CaCO_3 deposits.

3.1.2 Introduction

With the widespread application of reverse osmosis (RO) to the treatment of a great variety of waters, the topic of membrane scaling became a subject of high research interest. In the 1980s, for example, numerous publications already deal with

the avoidance of scaling on RO membrane modules [A1]. Efficient RO operation and the associated challenges related to mineral deposits in membrane modules are drivers of a continued high level of research interest [A2]. The findings of experimental scaling research are based on a great variety of methods for detecting crystals or their effect on the membrane process. In a recent study, for example, it is shown by transmission electron microscopy that CaCO_3 crystals of a few nm in size can be found in cavities of the microstructured polyamide surface that serves as the active RO membrane layer [A3]. Research on the structure of already advanced salt deposition also provides important findings. For example, it has recently been shown by evaluating membrane permeability and subsequent *ex-situ* membrane analysis that an electromagnetic field (EMF) can be used to cause a permeability-improving change in crystal or scaling structure. The cleanability of the membrane surface could also be improved by applying the EMF. Energy dispersive X-ray spectroscopy (EDX) and scanning electron microscope (SEM) are used to analyse the scaling structure [A4]. In another study it could be shown that a permeability decrease of the membrane depends more on the growth orientation of the crystals than on the deposited crystal salt amount [A5]. A characterization of the scaling and crystal structure could be carried out by membrane removal and further conditioning steps. For this purpose atomic absorption spectrometry (AAS), X-ray diffraction (XRD), grazing incidence wide angle X-ray scattering (GIWAXS), vertical scanning interferometry (VSI) and atomic force microscopy (AFM) are applied [A5]. Also, some recent publications deal with the influences of scaling inhibiting or modifying ingredients as they occur in real applications. For example, it is recently shown by SEM and EDX that an optional upstream ultrafiltration resulted in an increased scaling caused by a reduction of organic matter [A6]. An induction time theory at existing supersaturation is assumed since long for various scaling substances such as CaCO_3 . However with regard to CaCO_3 , it is now considered that the induction time theory is not applicable and that only the late detectability in the membrane process had led to this assumption [A7]. Nevertheless, the induction time theory is still used in scaling research on CaCO_3 . For example, in their experiments, Mangal 2021 *et al.* defined the time span up to a pH drop of 0.03 units by CaCO_3 precipitation as the induction time [A8]. For the evaluation of sulphate deposits such as CaSO_4 , the induction time is frequently used in the recent literature [A9–A12]. In general, the methods used for scaling analysis can be divided into *ex-situ* and *in-situ* analysis. The classical *in-situ* approaches of scaling detection by evaluation of membrane performance such as flux or permeability can only indicate advanced scaling. Using the *ex-situ* methods, the membrane modules used must be opened and are thereby destroyed to examine the suspected salt precipitation. The major advantage of *ex-situ* methods is the subsequent applicability in a great variety of analysis methods such as described above. However, when removing and handling membranes outside the membrane modules to examine the crystal structures, numerous possible influences must be considered. For example, influences on the crystalline structures by crystal ripening or a subsequent formation of crystals by evaporation and drying of dissolved salt residues on the membranes must be considered. In addition to the elaborate and mostly destructive *ex-situ* methods described here as examples,

we have already given an overview of existing *in-situ* sensor systems in Part 1 of this publication series [A13]. The need for a universal and simple detection method for early-stage scaling and fouling in general is pointed out there. This need for research and development of detection methods is also highlighted as an important research gap in recent literature [A7]. The purpose of this paper is to demonstrate the potential of a new optoelectronic *in-situ* and highly sensitive detection method based on polymer optical fibers. This is the third part of our publication series on CaCO_3 scaling in RO membrane modules. In Part 1, the state of the science on the prediction and detection of CaCO_3 scaling was presented. The results presented in this work are based on a new measurement method using POF. This principle was presented in Part 1 and placed in comparison to current methods. In Part 2, a new hydrochemical simulation model was presented, which is used in this paper as a basis for describing the saturation of important CaCO_3 polymorphs and crystallization zones.

3.1.3 Materials and methods

This study aims at the combination of predictive calculations of CaCO_3 supersaturation on RO-membrane surfaces with several monitoring methods to detect deposits on RO membranes. To start, the monitoring methods among them the image analysis and the setup of polymer optical fiber sensors will be presented in the sections 3.1.3 and 3.1.3 In a second step saturation predictions and the experimental setups will be described.

Image analysis method

The flat membrane module made of Polymethylmethacrylate (PMMA) allows to take pictures in transmitted light mode. The advantage is that CaCO_3 -crystals scatter the light out of the optical line “light source-membrane-camera” (see figure 3.3) due to their deviating refractive index, such they appear dark in the photo. The pictures are taken with a Basler-acA3088-57uc CMOS camera every 5 min. The images can be focused on the membrane surface due to inhomogeneities on the surface.

Imaging of the membrane surface and subsequent image processing is aimed at detecting CaCO_3 -crystals on the membrane surface. The recorded images are processed with MATLAB 2020b software. The detection of the crystals allows the determination of the membrane area covered with crystals.

Figure 3.1 illustrates the steps of image processing. The images are rotated and then cropped so that the free membrane area can be further analysed in a feed spacer square of 1.8 x 1.8 mm. The feed flows diagonally through the feed spacer square. Photos are typically described by three matrices with the red, green and blue components. The original colour RGB image is converted to a grey-scale image. To improve image quality, the contrast stretching method is often used [A14]. Using this method, the crystals on the membrane surface become more visible. The membrane

area coated by crystals can be measured using binarization of the grey-scaled image. As a threshold to binarize the grey image a local adaptive function with a brighter background is employed. For binarization an adaptive method is used, such that brightness differences do not impact the image analysis. Finally, a crystallisation ratio was calculated by comparing the area ratios of the overall image to the area covered with crystals. The minimum size for the detection of the CaCO_3 -crystals is a covered membrane area of $350 \mu\text{m}^2$.

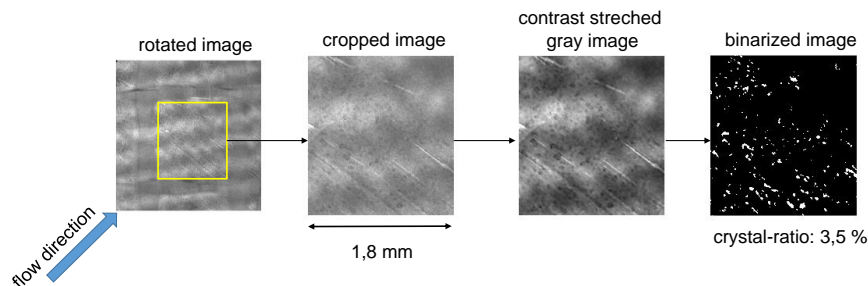


Figure 3.1: Image processing for crystal detection on the membrane surface. From left to right: Rotated image, taken in transmitted light mode, Cropped image, Contrast stretched grey scaled image, Final binarized image with detected crystals on the surface (white points) and the crystal-ratio=white pixels/total pixels

Optical fiber setup

We chose as fibers for the optical sensors Asahi Luminos DB 500 polymer optical fibers (POF) with a diameter of $500 \mu\text{m}$. The fiber consists of a PMMA core and a fluoropolymer cladding. For the scaling detection, the $10 \mu\text{m}$ fluoropolymer cladding is removed as a sensor zone with a length of 5 cm using ethylacetate. This principle was already illustrated in the first part of this publication series [A13]. In the sensor zone, the light rays interact with deposits on the fiber surface, because there is the possibility of interrupting the total reflection of the light in the fiber. In 3.2 these are the modified sensor-fibers 1 and 3.

As shown in Figure 3.2, red light (660 nm) is emitted in a light splitter and into the POF for scaling detection. Red LED are commonly used for data communication over POF because of the low optical attenuation in this wavelength region [A15]. Fiber 2 is the reference fiber without a sensor zone. This fiber is used to detect optical power fluctuations which are not due to scaling, for example due to thermally fluctuating LED power or detection sensitivity of the sensor, or due to ageing of LED, detectors and fibers. For measuring the optical power (optometry), the transmitted optical power of all fibers is detected by amplified photodetectors (Thorlabs PDA100a), and their output voltage U proportional to the optical power P is registered digitally. The optical setup is used in the RO flat cell as well as in water bath experiments, where supersaturated salt solutions with sulphates and CaCO_3 were examined.

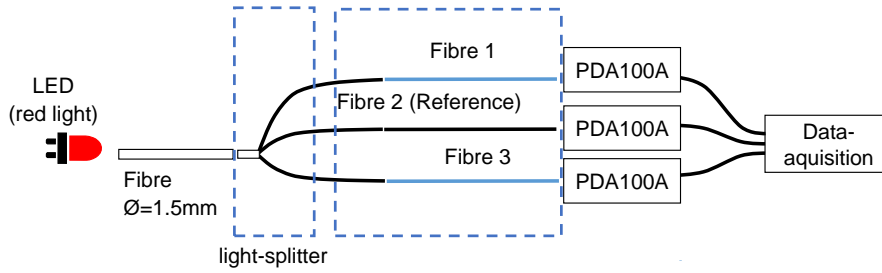


Figure 3.2: Polymer optical fiber setup as a sensor for scaling detection

For the data processing, only relative transmission signals τ are used. τ is calculated by the ratio between the measured transmitted light power P and the intrinsic transmitted power at the beginning of the experiments P_0 . In addition, the behavior of the reference fiber is included in the calculation of τ .

$$\tau = \frac{P}{P_0} - \frac{P(ref)}{P_0(ref)} + 1 \quad (3.1)$$

PHREEQC calculations

The measurement-based detection methods are compared with hydrochemical simulations performed using PHREEQC software – describing the supersaturation of CaCO_3 and sulfates. The calculation of CaCO_3 as ΔpH value is carried out as described in Part II of this publication series [A16]. CO_2 passage through the membrane is calculated according to measured pH values in the retentate stream. The calculations were run in PHREEQC version 3.7.3.15968 using the phreec.dat database. Rising pH values in the feed solution with the second experimental protocol in section 3.2 are also adapted by CO_2 extraction. Saturations of sulfates for the water bath experiments are likewise calculated using the phreec.dat database.

3.1.4 Experimental setup - POFs in different supersaturated salt solutions

The primary purpose of the initial tests with the POF sensors is to prove the theoretically forecasted influence of crystallisation on the sensor signal. The secondary objective is to achieve different salt precipitations on the surfaces of the POF so that common scaling components could be tested.

Therefore, the POFs are installed in supersaturated salt solutions. The experiments are carried out in triplicate, with CaSO_4 , BaSO_4 , SrSO_4 and CaCO_3 being investigated. The CaCO_3 – solution is tested in pure form as well as with 2 different concentrations of the antiscalant MT4000. The experiments took place at a temperature of 21 °C. The pH value is measured with a pH-meter, type WTW Multi 3320. Table 3.2 lists the concentrations of all synthesised salt solutions together with the component salts which form the final deposit on the POF surface. Based on Gibb's

free energy, the supersaturation, i.e. saturation indices greater than 0, represent a measure of the driving force of precipitation [A13]. After the experiments, the POFs are dried, and pictures are taken of the POF surfaces with a light microscope.

Table 3.2: Examined salt solutions with the individual components from which the crystals on the POF surfaces were formed.

final deposit	solution 1	solution 2	saturation index	precipitate name	precipitation potential in mmol L^{-1}
CaCO_3	99 mmol L^{-1} NaHCO_3	33 mmol L^{-1} CaCl_2	Calcite: 2.5 (1.4 as ΔpH) MCC: 1.2 (0.9 as ΔpH) ACC:0.5 (0.4 as ΔpH)	Calcite	30
$\text{CaSO}_4 + 2 \text{H}_2\text{O}$	70 mmol L^{-1} Na_2SO_4	70 mmol L^{-1} CaCl_2	0.7	Gypsum	46
SrSO_4	8.2 mmol L^{-1} Na_2SO_4	8.2 mmol L^{-1} SrCl_2	1.6	Celestite	7.5
BaSO_4	1.5 mmol L^{-1} Na_2SO_4	1.5 mmol L^{-1} BaCl_2	3.7	Barite	1.49

Experimental RO-setup

The experiments to investigate the effects of scaling in an RO-filtration system are carried out in a cross-flow filtration setup with a spacer-filled channel. A schematic diagram of the pilot-RO-system is provided in Figure 3.3. The cross-flow conditions are representative for spiral wound membrane modules [A17]. Before the scaling experiments started, the hydraulics of the cell are validated by comparing the expected pressure drop and measured values with calculations according to Schock and Miquel (1987) [A18]. By a variation of the cross-flow velocity, the pressure drop could be measured and compared to the theory [A18].

For this study, thin film composite membranes (Type: DOW XLE) with a size of $95 \text{ cm} \times 3.4 \text{ cm}$ (3.4 cm^2) are used. The storage of the low-pressure membranes took place in 4% $\text{Na}_2\text{S}_2\text{O}_3$ at 20°C until the experiment starts.

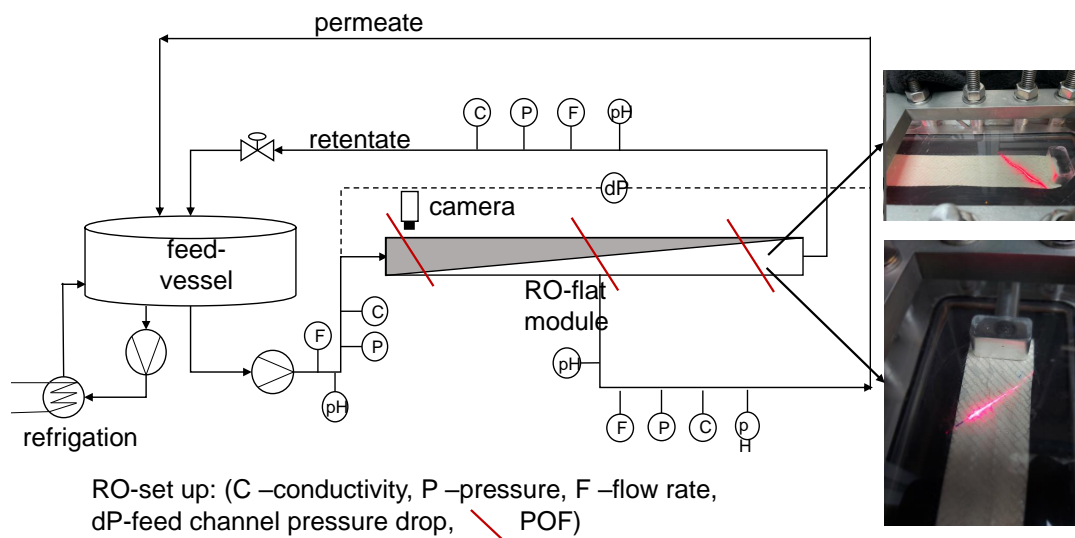


Figure 3.3: Schematic diagram and photo of the RO pilot plant, involving a cross-flow membrane flat module with POF sensors

For all crystallisation experiments, synthetic water containing NaHCO_3 and CaCl_2 is mixed in an 80 L feed vessel. The concentrations and CaCO_3 saturations are shown in associated sections 3.2 and 3.3. The test solutions were prepared newly for each experiment and kept almost constant at $20\text{ }^\circ\text{C}$ ($\pm 1\text{ }^\circ\text{C}$) by cooling. The test solution is fed via a Novados H1 pump through the feed-sensor module (pH, conductivity, temperature, flow rate) in the flat membrane module. In the feed channel above the membrane and under the feed spacer three POFs are diagonally installed along and between two fibers of the feed spacer. The pH value, the conductivity, and the flow rate of the permeate and retentate are measured continuously. Table 3.3 lists the sensor types used in the RO-pilot plant.

Table 3.3: Sensor types in the RO-pilot plant

measurand	place	sensor type
flow rate	retentate	E+H Promass A300/8A3B01 DN 01
flow rate	permeate	Natec NU-140
conductivity	feed, retentate	Jesco-LF-110 (0-20mS/cm)
conductivity	permeate	Jesco-LF-110 (0-1mS/cm)
pH	feed, retentate, permeate	Hamilton PolyLite-Plus-H-Arc-120
temperature	feed, permeate	PT-100- Jesco-LF-110
pressure	feed, retentate, permeate	Wika-A-10
differential pressure	feed-channel	E+H PMD75

All sensor data are collected and stored by a Siemens S7 SPS in time intervals of 1s. The retentate flow is automatically kept constant by a motorised needle

valve and the flow rate sensor in the retentate, so that the cross-flow velocity stays 10 cm/s during the tests. Such flow velocity and resulting Reynolds number are found in retentate side membrane modules in practice [A16]. The feed pressure is automatically kept constant at 12 bar by coupling the pressure sensor in the feed and a frequency converter for the feed pressure pump. Further parameters are shown in Table 3.4. They were determined in a reference experiment with 2 g L⁻¹ NaCl feed solution.

Table 3.4: RO Parameter measured in a reference experiment with 2 g L⁻¹ NaCl-feed-solution

RO-parameter	formular symbol	magnitude
flux	J_w	55 L m ⁻²
recovery	r	30 %
temperature	T	20 °C ±1 °C
concentration factor	CF	1.45
Reynolds number	Re	140
Schmidts number	Sc	800
Shrwoods number	Sh	2.5
concentration polarization	β	1.1

During the experiments, the supersaturation of the different polymorphs of CaCO₃ is reached by adjusting the concentration (reject permeate) or by dosing sodium hydroxide in the feed vessel to the solution containing Ca²⁺ and dissolved carbon. The experimental protocol and its results will be presented in the following chapter.

3.1.5 Experimental setups and results

The series of experiments are splitted into three parts. Firstly, POFs are immersed in the supersaturated salt solutions. In the second part an experimental protocol is discussed in which the supersaturation of all CaCO₃-polymorphs in the RO-pilot plant is reached by continuous dosing NaOH to the feed-solution. The third experimental protocol is devoted to a constant feed concentration in analogy to the literature [A19] in order to apply conditions that are as relevant to industrial practice as possible.

Experimental protocol – POF in highly supersaturated salt solutions

The first experimental protocol is a setup for POFs placed in supersaturated water solutions. The aim is to prove that different salt deposits on POF's surfaces cause a drop of light transmission. Is this hypothesis hold, the transmission drop means the detection of salt deposits via polymer optical fiber sensors. Therefore, the POFs are tested in calcium carbonate, calcium sulfate, barium sulfate and strontium sulfate solutions. These are common deposits on RO-membrane surfaces. All solutions

are supersaturated, see table 3.2. Figure 3.4 shows the course of the transmission for the sulfate solutions together with photos of the POF surfaces taken after the experiments, that is reached when a quasi-steady state of τ is reached.

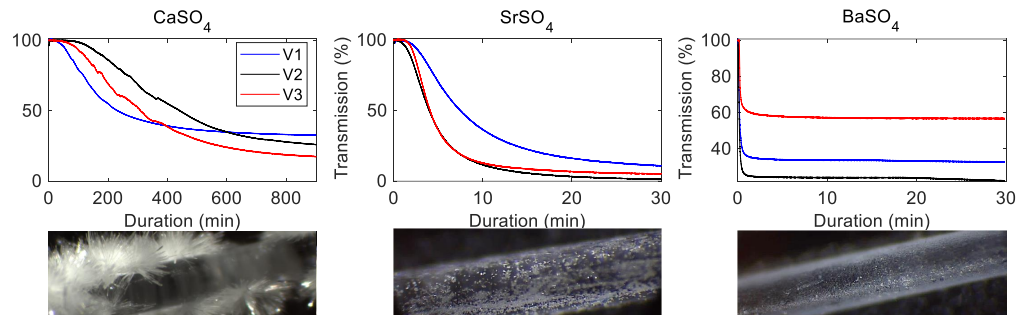


Figure 3.4: Upper part: Transmission data from the POFs immersed in the sulfate solutions. From left to right: Calcium sulfate, strontium sulfate and barium sulfate. Lower Part: Photos of the POFs after the experiments with respective salt crystals on their surfaces. V1, V2, V3 describe the triplicate.

The photos clearly show the crystals on the POF surfaces. The crystals have different morphologies such as the characteristic needles from gypsum. As the experiment progresses, the light transmission τ via the sensor fibers decreases. For all three sulfate salts τ drops in the first phase of the experiment. Later τ approaches an almost constant level. In the present sulfate experiments, the saturation indices increase from CaSO_4 to SrSO_4 and finally to BaSO_4 (see Table 3.2). The precipitation kinetics determined with the POF also show this relationship with the fastest transmission decline in the BaSO_4 experiments. Note also that the slightly supersaturated CaSO_4 solution show a relatively slow transmission decline over several hours. The following experiments show the detection of CaCO_3 -crystals in water bath of the salt solutions. Also, the influence of antiscalant (AS) MT 4000 on the crystallisation and in particular on the development of transmission decline is shown. As a reference measurement for CaCO_3 precipitation, the development of the pH value is also monitored.

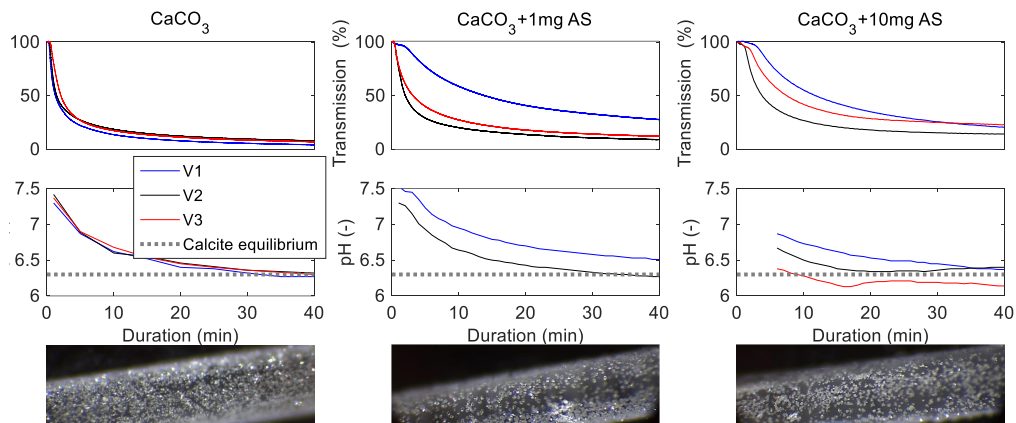


Figure 3.5: Experimental data from POFs immersed in CaCO_3 -solutions. Top row: transmission data of POFs immersed in a pure CaCO_3 -solution, a solution with 1 mg/l antiscalant (AS) MT4000 and 10 mg/l. Middle row: Development of the pH values of the corresponding experiments. Bottom Row: Photos of the POFs after the experiments with the salt crystals on their surfaces.

In all experiments CaCO_3 -scaling is indicated by decreasing pH values as well as decreasing transmittance values of the POFs. Trigonal calcite deposits are visible on the fiber surfaces in the photos. With increasing concentration of the AS, the transmission decreases less. Furthermore, the increasing AS concentration delays the transmission loss. The weaker decrease in transmission indicates decreasing crystallisation. 10 mg L^{-1} AS cause a delay of 2–5 min of the strong transmission drop at the beginning of the experiment. For the AS experiments, the photos show less but larger crystals. Commonly, AS impacts the free surface of crystal clusters, thereby retarding the formation rate and growth rates of crystallisation [A20]. We conclude that, all salt precipitations (CaSO_4 , BaSO_4 , SrSO_4 and CaCO_3) cause a strong transmission loss via the POFs with a sensor zone. In combination with the AS, the transmission behaviour is changed and slowed down. These experiments proof that POFs can be a universal sensing element for precipitation detection of salts relevant in reverse osmosis technology.

Experimental protocol – membrane cell – supersaturating CaCO_3 via pH adjustment

In this section we start the experiments with undersaturated solutions for all CaCO_3 -polymorphs. The experiments are designed so that undersaturation of all CaCO_3 -polymorphs in the solution is achieved by the dosage of HCl down to $\text{pH} = 4.5$. The experimental conditions, including the cross-flow velocity $v = 10 \text{ cm s}^{-1}$ and the feed pressure $p_{feed} = 12 \text{ bar}$, are kept constant during the whole experiment. The experiment is obtained in full-recycle mode. The saturations values of all polymorphs were determined with the software PHREEQC. Each experimental protocol is run in triplicate. They are started with cleaning the RO-system using citric acid at $\text{pH} = 3$. Next, the rinsed membrane with feed-spacer, permeate-spacer and three POFs are installed in the membrane flat cell. Among the POFs, one fiber is a reference-fiber

where the cladding is intact; hence no detection of deposits is possible by this fiber. The POFs with sensor zones were included on the feed side of the flat cell and the retentate side. The experimental procedure includes first a conditioning phase for 12 h at experimental conditions but with desalinated tap water. After the conditioning phase, $2 \text{ mmol L}^{-1} \text{ CaCl}_2$; $3.5 \text{ mmol L}^{-1} \text{ NaHCO}_3$ and $3.2 \text{ mmol L}^{-1} \text{ HCl}$ are mixed in the feed vessel. Each salt is pre-solved in 80 L desalinated water and then mixed in 80 L desalinated water. This procedure avoids homogenous crystallisation. The undersaturated CaCO_3 -solution is then pumped through the RO-system for a period of 24 hours in complete recycling mode. Then the dosing of $2 \text{ mL h}^{-1} \text{ 0.1 mol NaOH}$ is started at experimental time = 36 h until the pH value of 11 is reached as the end of the experiment. During the entire experiment, photos are taken every 5 min with a resolution of 3088×2064 pixels. After the termination of the experiments (i.e. 144 h), the membranes and the POFs were dried and prepared for light- and scanning electron microscopy. The experimental data of one experiment are shown in figure 3.6. The two remaining experiments of the triplicate show similar results.

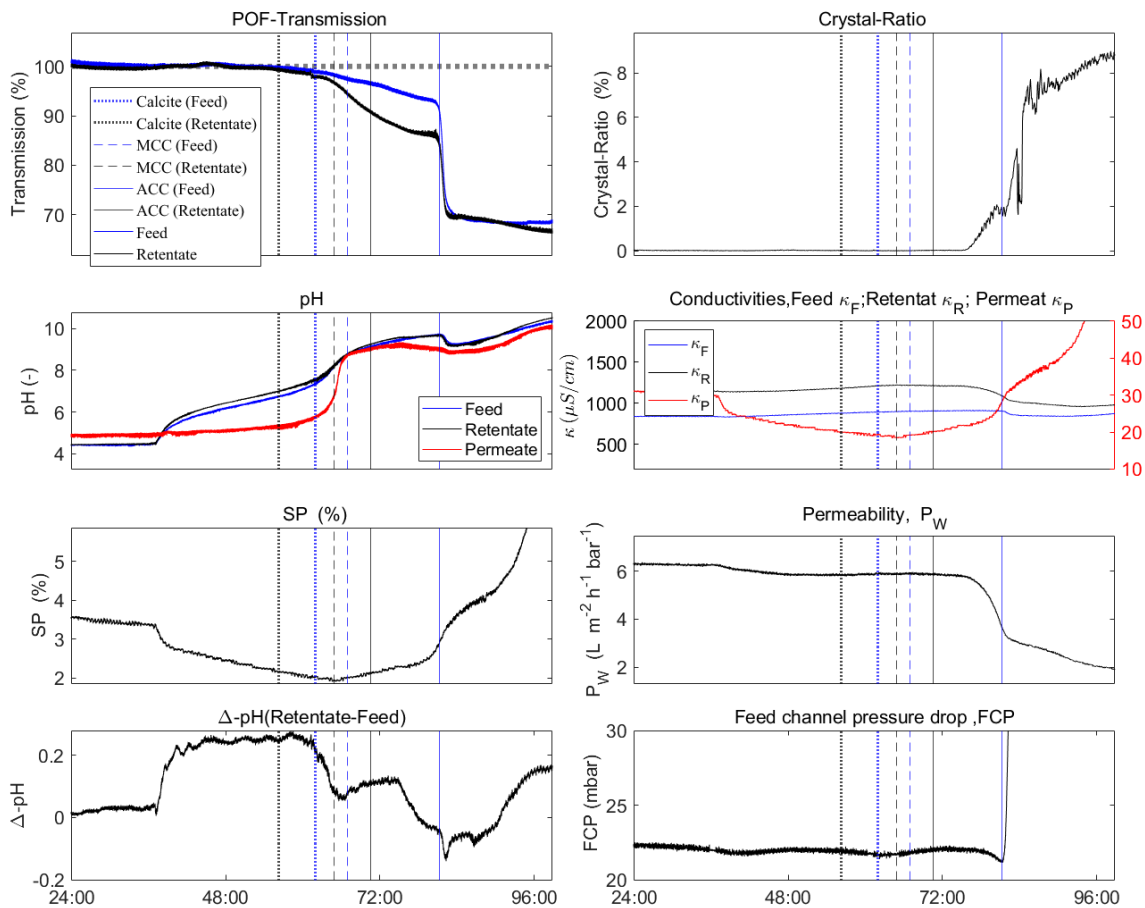


Figure 3.6: Time series from the experiment with CaCO_3 - supersaturating via pH adjustment. The initial pH value is adjusted with hydrochloric acid to 4.5. Then the supersaturation of the CaCO_3 -polymorphs is achieved by dosing 0.1M NaOH into the feed water. The vertical lines mark the first occurrence of supersaturation of the CaCO_3 -polymorphs in the feed and the retentate.

The total experimental duration is 144 h. The time series show the effects of crystallisation in the RO-plant until 96 h for closer visualisation of the most relevant period. The FCP value increased by about 300 % at the very end. The FCP serves a measure for hydraulic resistance along the membrane, and is therefore indicating a narrowing of the flow channel along the membrane at the constant volume flow rate. Note that the salt passage first decreases, and later increases. The early decrease is caused by the pH-dependent salt rejection of polyamide-RO-membranes [A21]. The following increase indicates scaling. The salt passage increases by about 750 % throughout the whole experiment. The water permeability through the membrane is decreasing by about 80 %. All these basic parameters indicate the CaCO_3 -crystallisation and deposition in the RO-system. The conductivities in the feed and retentate remain almost constant until strong crystallisation occurs at time = 80 h.

Figure 3.6 also shows the time series of the calculated crystallisation rate which is shown in more detail in Figure 3.7 (image processing see section 3.1.3).

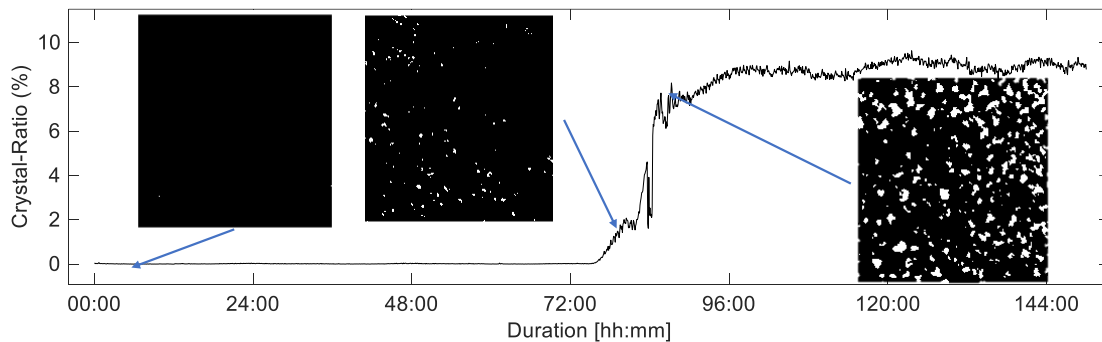


Figure 3.7: Crystal-Ratio Time series with raw images and binarized images. From left to right: no Scaling; light Scaling; progressed scaled membrane

Until 72 h no crystals on the membrane surface are detected. From 82 h forward the crystal-ratio increases strongly. After 75 h a slight increase of the crystal ratio can be observed. During this first increase the CaCO_3 - crystals are rather located in the lower left corner of the processed image. Due to the location of the first visible crystals, the CaCO_3 -crystals seem to be formed and grow in the flow shadows behind the feed-spacer (see figure 3.1). This indicates a higher concentration polarisation (CP) in flow-shadowed regions on the membrane surface. CP often calculated as a mean value describing a whole membrane module. In fact, it is known that the flow conditions in spacer filled feed channels are widely inhomogeneous [A22]. The local flow conditions influence the local CP directly [A23]. Another effect illustrated in Figure 3.7 is the plateau of the crystal-ratio as reached after the first detected crystals ($t=84$ h). Even when the membrane surface is fully covered with CaCO_3 -crystals the crystal-ratio will never reach the value of 100%. This discrepancy may be caused by inevitable approximation in image processing when dealing with overlapping crystals. These overlapping crystals cause a backscattering of the transmitted light into the optical line “light source-membrane-camera”, so that the crystals appear no longer dark in the captured images and are no longer detectable.

This effect can be proofed by SEM analysis as shown in figure 3.8. This picture illustrates the overlapping calcite crystals on the membrane surface.

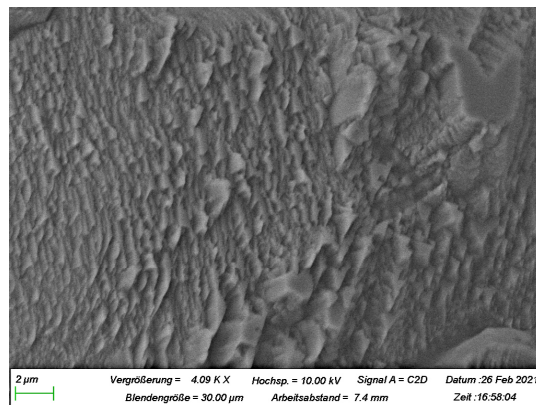


Figure 3.8: SEM picture of overlapping calcite crystals on the RO membrane surface. The picture is taken after an experiment with increasing pH value

In conclusion, the image analysis method can give a good impression of the first visually detected CaCO_3 -crystals and of the incipient crystallization. However, as the crystallization proceeds, overlapping crystals make a correct calculation of crystallization ratio impossible. A realistic view of the crystallization on the membrane surface can be obtained between the plateau, where the crystals overlap each other and the first crystals are detected; this holds for $t=75$ h until $t=84$ h in the experiment shown in figure 3.7. In RO-plants, heterogeneous crystallization is to be expected the predominate crystallization pathway (undersaturation of ACC). A major challenge during the experiments is to reproduce heterogeneous crystal nucleation in the RO-pilot plant. There are two theories for the crystal formation in the literature. According to the theory of Karabelas *et al.* heterogeneous crystallization takes place whenever calcite is supersaturated [A19]. They proved their theory by SEM imaging of crystal nuclei formation on RO-membrane surfaces. Elfil *et al.* purpose a heterogeneous crystallization as soon as monohydrated CaCO_3 (MCC) is supersaturated [A24]. MCC is the precursor for crystal nuclei formation. Our experiments, presented in this paper with initial undersaturated start, the theory of Elfil *et al.* seems more suitable since simultaneously to the saturation of MCC we observe an alteration in the salt passage and also the transmitted light through the POFs. The ΔpH in figure 3.6 indicates the difference in pH values between feed and retentate stream. It also changes with the supersaturation of calcite in the feed solution. The pH value in the retentate increases in this time range by 0.2 compared to the pH value in the feed. Precipitation of CaCO_3 leads to decreasing pH values and could therefore indicate precipitation in the membrane cell. This interpretation again is rather compatible to Karabelas theory [A19]. Three parameters feed channel pressure drop, permeability, and the calculated image crystal-ratio are changing simultaneously to the supersaturation of amorphous CaCO_3 (ACC). This indicates the expected strong homogenous crystallization in the RO-plant according to the theory of Elfil *et al.* [A24]. With the saturation of ACC, the POF signal also reacts strongly with a rapid decrease of light transmission. The transmission loss at this

point is much stronger as it is at the saturation point of MCC previously. In summary, the calculation for the CaCO_3 saturation of different polymorphs (vertical lines in Figure 3.6) are a good indicator of when precipitation on the membrane surface is to be expected. The POF sensor is sensitive to incipient crystallization on the membrane surface. Incipient crystallization is detected by the first transmission drops earlier than the common parameters permeability, FCP or even image analysis. The salt passage changes in time with the POF transmission drops. However, it is unclear whether this is due to scaling alone or to the pH-dependent behaviour of the salt passage. Certainly, it is difficult to distinguish between primary or secondary crystallization. The RO-pilot system is not designed and built according to the principles of hygienic design. Therefore, incomplete cleaning of crystal residues is possible, which may lead to secondary crystallization from the beginning of each experiment. However, the second and strong transmission loss of the POF sensors (ACC saturation in the feed water) indicates that the pH increases during the experiment initially led to primary, heterogeneous crystal formation in the feed channel. Our saturation calculations on MCC and ACC saturation support this hypothesis. The presented experimental results in this section do not allow a clear preference to either the theory of Karabelas *et al.* [A19] or the theory of precursor role of MCC of Elfil *et al.* [A24]. In order to produce heterogeneous scaling on the membrane with greater reliability, another experimental setup is performed in the RO-pilot plant.

Experimental protocol – membrane cell – constant conductivities and pH values

In the third experimental protocol, presented in this section, the saturation is kept almost constant. This leads to a more realistic RO-setup. The functionality of the POF sensor can thus be examined for practice orientated precipitate formation. Firstly, a compaction phase proceeded for 24 h. Secondly, the feed solution is mixed in the feed vessel. The feed solution consists of 11.8 mmol L^{-1} CaCl_2 and 6.5 mmol L^{-1} NaHCO_3 . The pH value is adjusted to 6.8 by HCl. The experimental protocol includes a discharge of permeate and retentate during the experiment. The whole experimental setup is as close as possible to that of Mitrouli and Karabelas *et al.* [A19, A25]. They propounded the theory that no induction time exists and CaCO_3 precipitates immediately after supersaturation of calcite. Figure 3.9 presents our experimental results.

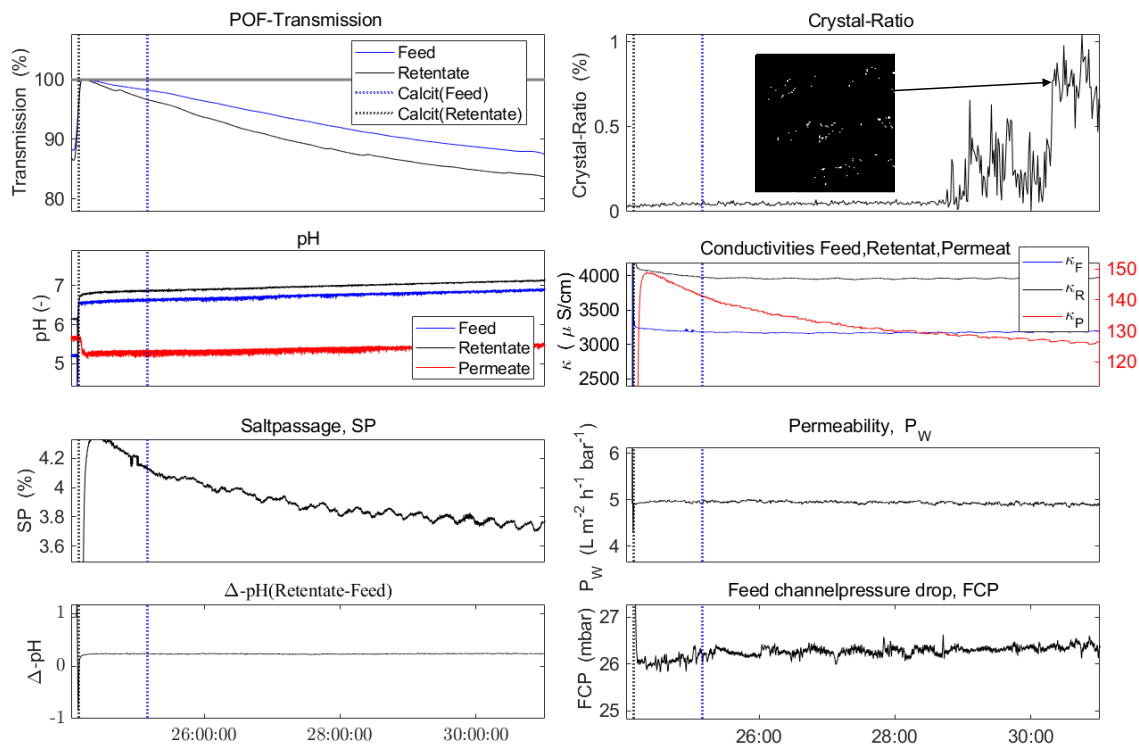


Figure 3.9: Time series of an experiment with calcite supersaturation in the retentate stream. The compaction phase of the membrane lasted up to 24 hours. Then the experiment is continued with almost constant saturation conditions where calcite is supersaturated. The pH value is adjusted to 6.8 with HCl at the beginning of the experiment. The vertical lines mark the first occurrence of supersaturation of calcite in the feed and the retentate. MCC and ACC are undersaturated during the experiment.

The calcite is supersaturated in the retentate since the beginning of the experiment after the compaction phase. Calcite saturation in the feed is reached at duration =25 h due to a slight shift in pH value likely due to CO_2 degassing from the ventilated circulation tank. The experimental data show the effect of light scaling in the RO-system. The permeability is slightly decreasing from 5 to $4.9 \text{ L h}^{-1} \text{ bar}^{-1} \text{ m}^{-2}$, and the pressure drop in the feed channel is increasing slowly from 26.0 to 26.5 mbar. The origin of these marginal trends, which stand out only slightly from the signal noise, cannot be clearly determined. The salt passage is decreasing by 15%. This might be an effect of a post-compaction of the membrane during the experiment. The image analysis is the only parameter that shows that crystallization is certainly taking place in the RO-system. From 29 h time forward, small crystals are detected by the image analysis. The level of crystallization detected in the images is only 1 %. This means that the crystal-ratio calculated by automatically image analysis is below the above-mentioned plateau level, where the overlapping crystals affect the image analysis. Regarding to the minimum detection level of $350 \mu\text{m}^2$ for each crystal the image analysis gives a realistic view of emerging CaCO_3 crystals on the membrane surface. The light transmission through the POFs is immediately decreasing after dosing the salts in the feed vessel. As in the previous section the

retentate fiber transmission is decreasing stronger than the feed fiber transmission. This can be explained by an earlier and stronger crystallization on the retentate side of the membrane cell. Here, the salt concentration and thus the supersaturation is higher than in feed side of the cell. As shown in Figure 3.9 scaling is detected earlier and more strongly by the POF sensors than any other parameter in the reverse osmosis system. The SEM-picture in figure 3.10 illustrates the effect of POF on RO-membrane surfaces. Clearly visible are the crystals formed near and beneath the POF. It appears as if the POF is partially embedded in the crystals. Furthermore, the crystals are mainly growing near to the POF imprint on the membrane surface. This could be explained due to high local salt saturation, which is enhanced by a higher concentration polarization in the flow shadows generated by the POFs. Hence, the crystals grow firstly in the area around the POFs and in consequence the functioning of the POF as an early scaling sensor seems positively influenced by this locally enhanced concentration polarization as it also appears at the feed spacer fibers along the membrane channel.

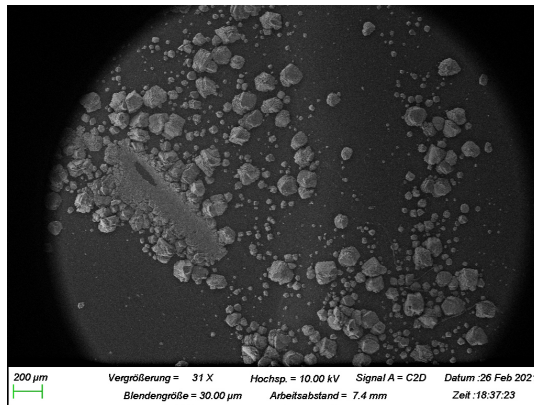


Figure 3.10: SEM Picture with a POF imprint from an experiment with constant conductivities and pH values

In addition, the SEM image (figure 3.9) shows a membrane surface not completely covered with crystals. As explained above, the image processing can therefore still detect single crystals. The time series given in figure 3.9 have not reached the plateau value of 10 %, which is known from the experiments described in section 3.1.5 In conclusion, the comparison of our experiments with those of Karabelas *et al.* led to similar results [A19]. After the triplicate, it can be stated that the supersaturation of calcite is sufficient for crystal growth on RO-membrane surfaces. This has been demonstrated using online sensors such as the POF sensors and image analysis, as well as the offline method through SEM analysis. The results show that supersaturation prediction of MCC is not necessarily the key factor for the critical formation of crystals. It cannot be finally determined whether this is due to an early primary crystal formation or due to crystal nuclei remaining in the RO-system after rinsing with citric acid, which cause secondary crystal growth.

3.1.6 Conclusion

In this study, two new *in-situ* methods for the scaling detection in RO-modules are presented:

- 1 An early detection of inorganic precipitations on the RO-membrane surface and *in vitro* is possible by using polymer optical fiber (POF) sensors. This leads to a method by which crystallization processes in RO-systems can be detected before the crystallization itself impacts on the performance of the RO-filtration. It is proofed in two experimental designs (each executed in triplicate), that in the very moment when the POF first detects crystals the performance of the RO-system is not deteriorate. The membrane permeability (i.e. normalized water flux) and the salt rejection decrease later in the experiments. The feed-channel pressure drop does not increase or increases only many hours after the POFs already have detected the crystals on the membrane. The sensitivity of the POF sensor is proofed in an RO-flat membrane cell with CaCO_3 and in water solutions with CaSO_4 , BaSO_4 , SrSO_4 and CaCO_3 in combinations with an antiscalant.
- 2 The second *in-situ* monitoring method for crystallization processes in membrane flat modules is an image analysis method for the detection of the crystals and for the assessment of their sizes. Due to this method in combination with the transparent PMMA-membrane flat cell we were able to detect CaCO_3 -crystals with a covered membrane area of $350 \mu\text{m}^2$. The image analysis detects crystallization processes earlier than the membrane performance begins to decrease. This is proved in the experiments guided by the experimental setup of Karabelas and Mitrouli *et al.* [A7][A19]. The image analysis method is suitable to validate the presented POF sensors. The POFs can now also be used with spirally wound membrane modules where the image analysis method does not work.

The accompanying simulation methods (published in Part I and II) for calculating saturation by the pH value in the salt solution allows to predict precipitation in experiments. These simulation methods support the functionality of the POFs. The CaCO_3 polymorphs calcite, MCC and ACC were simulated. By our experiments it could not be clarified beyond doubt whether MCC plays a precursor role as in the experiments of Elfil *et al.* [A24]. As has already been shown in the literature with laboratory-scale experiments [A12][A14], it is doubtful whether induction time or meta stability [A24] play a role in CaCO_3 crystal formation in such experimental set-ups.

3.1.7 Outlook

This chapter gives an overview of integration concepts for the new POF sensor in industrial-scale RO systems [A26]. On the one hand, it is possible to couple flat membrane cells with POF as a monitoring device to such full-scale systems.

In addition, figure ?? shows various possibilities for integrating POF into spiral-wound modules. Concepts a) and c) must be included during the production of spiral wound modules. Replacing a spacer fiber by a POF has the advantage of avoiding additional flow shadows in the feed channel. This is desirable since the local concentration polarisation may be enhanced by additional fibers in the spacer net. Another strategy for integrating the POF sensor into conventional spiral-wound modules is shown with concept b). Here, a POF sensor with a front-side mirror (e.g. gold coating) is inserted between two membrane sheets. A realistic approach is to use POF sensors to detect incipient crystal nuclei in the last spiral wound module where the salt concentrations reach the highest values. For the detection of biological fouling the approach of Vrouwenvelder *et al.* [A22] seems more suitable. The highest nutrient loads and therefore biofouling is found in the membrane modules on the feed side. Therefore, a feed-side module should be equipped with a POF sensor for biofouling detection.

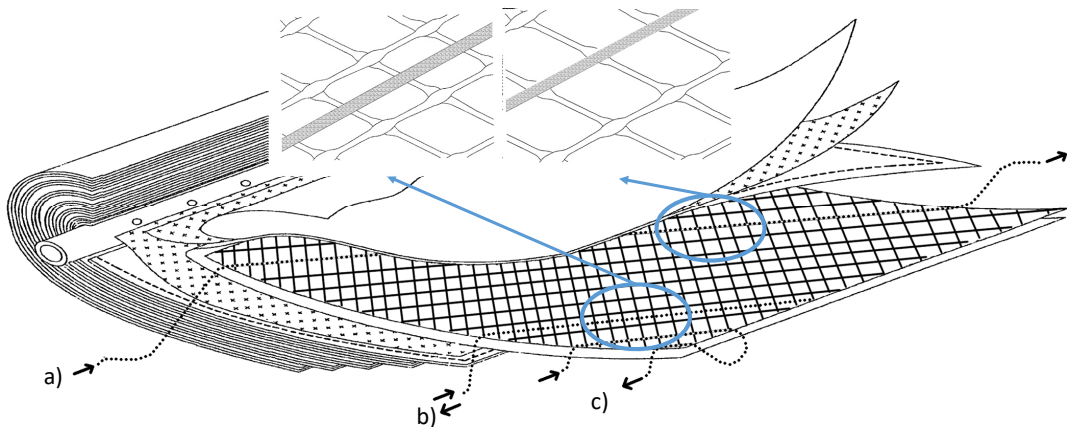


Figure 3.11: Integration concept for polymer optical fibers in spiral wound RO-modules: a) POF is replacing a feed-spacer fiber, b) POF with a mirror on the fiber end, c) back and forth integrated POF in the feed-spacer [A26]

3.1.8 Acknowledgments

The authors wish to thank Heribert Voit (Endress + Hauser) for the suitable cooperation and the rental of sensors to execute the experiments.

3.1.9 References

- [A1] A.G. Pervov, Scale formation prognosis and cleaning procedure schedules in reverse osmosis systems operation, *Desalination* 83 (1991) 77–118.
- [A2] S. Jiang, Y. Li, B.P. Ladewig, A review of reverse osmosis membrane fouling and control strategies, *The Science of the total environment* 595 (2017) 567–583.
- [A3] N.R. Sarker, P. Cherukupally, I. Gourevich, J. Wilbur, S.D. Jons, A.M. Bilton, Multi-scale visualization of incipient CaCO₃ scaling on the polyamide layer of reverse osmosis membranes, *Desalination* 539 (2022) 115956.
- [A4] W. Jiang, X. Xu, D. Johnson, L. Lin, H. Wang, P. Xu, Effectiveness and mechanisms of electromagnetic field on reverse osmosis membrane scaling control during brackish groundwater desalination, *Separation and Purification Technology* 280 (2022) 119823.
- [A5] M. Wang, B. Cao, Y. Hu, D.F. Rodrigues, Mineral Scaling on Reverse Osmosis Membranes: Role of Mass, Orientation, and Crystallinity on Permeability, *Environ. Sci. Technol.* 55 (2021) 16110–16119.
- [A6] X. Tong, Z.-W. Zhang, Y.-H. Wu, Y. Bai, N. Ikuno, K. Ishii, H.-Y. Hu, Ultrafiltration significantly increased the scaling potential of municipal secondary effluent on reverse osmosis membranes, *Water research* 220 (2022) 118672.
- [A7] A.J. Karabelas, S.T. Mitrouli, M. Kostoglou, Scaling in reverse osmosis desalination plants: A perspective focusing on development of comprehensive simulation tools, *Desalination* 474 (2020) 114193.
- [A8] M.N. Mangal, S.G. Salinas-Rodriguez, B. Blankert, V.A. Yangali-Quintanilla, J.C. Schippers, W.G. van der Meer, M.D. Kennedy, Role of phosphate and humic substances in controlling calcium carbonate scaling in a groundwater reverse osmosis system, *Journal of Environmental Chemical Engineering* 9 (2021) 105651.
- [A9] H.M. Abdel-Ghafar, E.A. Abdel-Aal, B.E. El Anadouli, Study on the nucleation aspects and morphology of reverse osmosis desalination scales with and without scale inhibitor at different supersaturation ratios, *Water Supply* 17 (2017) 493–499.
- [A10] J. Benecke, Gypsum scaling during reverse osmosis desalination – characterization and effects of natural organic matter, 2018.
- [A11] M. Bystrianský, O. Nir, M. Šír, Z. Honzajková, R. Vurm, P. Hrychová, A. Bervic, B. van der Bruggen, The presence of ferric iron promotes calcium sulphate scaling in reverse osmosis processes, *Desalination* 393 (2016) 115–119.
- [A12] H. Jaramillo, C. Boo, S.M. Hashmi, M. Elimelech, Zwitterionic coating on thin-film composite membranes to delay gypsum scaling in reverse osmosis, *Journal of Membrane Science* 618 (2021) 118568.
- [A13] S. Hager, A. Bachmann, T. Hofmann, R. Engelbrecht, K. Glas, CaCO₃ deposits in reverse osmosis Part I - Shortcomings of current approaches leading to a new prediction model and monitoring device (2021) 122–133.
- [A14] S.S. Negi, Y.S. Bhandari, A hybrid approach to Image Enhancement using Contrast Stretching on Image Sharpening and the analysis of various cases arising using histogram, in: *International Conference on Recent Advances and Innovations in Engineering (ICRAIE-2014)*, IEEE, 2014, pp. 1–6.
- [A15] O. Ziemann, J. Krauser, P.E. Zamzow, W. Daum, *POF-Handbuch: Optische Kurzstrecken-Übertragungssysteme*, 2nd ed., Springer, Berlin, Heidelberg, 2007.

- [A16] S. Hager, M. Meinardus, Thomas Hofmann, K. Glas, CaCO₃ deposits in reverse osmosis: Part II - Simulation model for hydrochemical predictions of reverse osmosis retentates and scaling propensity, *Brewing Science* 75 (2022) 54–68.
- [A17] N. Siebdrath, W. Ding, E. Pietsch, J. Kruithof, W. Uhl, J. Vrouwenvelder, Construction and validation of a long-channel membrane test cell for representative monitoring of performance and characterization of fouling over the length of spiral-wound membrane modules, *DWT* 89 (2017) 1–16.
- [A18] G. Schock, A. Miquel, Mass transfer and pressure loss in spiral wound modules, *Desalination* 64 (1987) 339–352.
- [A19] S. Mitrouli, A.J. Karabelas, A. Karanasiou, M. Kostoglou, Incipient calcium carbonate scaling of desalination membranes in narrow channels with spacers—experimental insights, *Journal of Membrane Science* 425–426 (2013) 48–57.
- [A20] K. Popov, M. Oshchepkov, A. Pervov, V. Golovesov, A. Ryabova, M. Trukhina, S. Tkachenko, A Case Study of Calcium Carbonate Crystallization during Reverse Osmosis Water Desalination in Presence of Novel Fluorescent-Tagged Antiscalants, *Membranes* 12 (2022).
- [A21] M. Stolov, V. Freger, Membrane Charge Weakly Affects Ion Transport in Reverse Osmosis, *Environ. Sci. Technol. Lett.* 7 (2020) 440–445.
- [A22] J.S. Vrouwenvelder, J.C. Kruithof, M.C.M. van Loosdrecht, *Biofouling of spiral wound membrane systems*, IWA Publishing, London, 2011.
- [A23] J.C. Crittenden, *MWH's water treatment: Principles and design*, 3rd ed., John Wiley and Sons, Hoboken, N.J, 2012.
- [A24] H. Elfil, A. Hannachi, Reconsidering water scaling tendency assessment, *AIChE J.* 52 (2006) 3583–3591.
- [A25] S.T. Mitrouli, M. Kostoglou, A.J. Karabelas, Calcium carbonate scaling of desalination membranes: Assessment of scaling parameters from dead-end filtration experiments, *Journal of Membrane Science* 510 (2016) 293–305.
- [A26] S. Hager, K. Glas, Membranmodul und Verfahren zur Detektion von Ablagerungen in einem Membranmodul.

3.2 Incipient biofouling detection via fiber optical sensing and image analysis in reverse osmosis processes

The research article “Incipient biofouling detection via fiber optical sensing and image analysis in reverse osmosis processes” was published in “*Membranes*” in 2023 (doi: 10.3390/membranes13060553). This article is a shared-first-author paper by H. Oesinghaus and D. Wanken. H. Oesinghaus developed the concept, analyzed and interpreted the data, co-wrote the original manuscript, and revised the manuscript based on the reviewers’ comments.

Several approaches have been published so far in RO membrane biofouling detection. Detection of biofouling at the feed spacers in an RO filtration system is crucial, since this is typically the initial site where biofouling occurs and later leads to downstream issues that are more difficult to mitigate. However, sensing strategies that can reliably detect biofouling at this early stage of the filtration process are yet to be developed. Thus, the purpose of the work presented in this chapter is to adapt the POF and imaging system presented in the previous chapter to the detection of biofouling. In addition, a comprehensive range of offline analytical methods that detect the number of colony forming units (CFU), monitor changes in ATP concentration, and employ total organic carbon (TOC) balancing and 16-s-RNA sequencing were used to verify the results from the online sensing techniques. By comparing these methods, a detailed protocol for early microorganism detection was drawn up for properly monitoring and interpreting the following aspects of biofouling: 1) POFs, 2) image analysis, 3) TOC balancing, 4) CFU Count, 5) ATP concentration changes, 6) changes in permeability, and 7) changes in the feed channel pressure drop (FCP). Moreover, the image analysis method from the previous chapter was successfully adapted to biofouling detection by splitting the image into red, green and blue channels. This allowed for the detection of color changes in the membrane and feed spacers by comparing the images from the entire duration of the experiment to those taken at the start of the experiment using a 2-D Pearson correlation. The POFs were also integrated into the spacer net, reducing their influence on the fluid dynamic properties of the membrane surface.

As an outlook, POFs were used to monitor the cleaning efficacy of pulsatile cross-flow conditions while enhancing biological growth conditions in the RO pilot plant. It was possible to detect changes in the accumulation phase depending on the length of this lag phase concerning the cleavage tendency of the attached microorganisms. Overall, this work contributes to a system that enables RO users to purify water that exhibits a tendency to form biofilms. Strategies to prevent biofouling could be managed by the signals from the fibers, which provide feedback on the cleaning of the membrane and feed spacer surfaces.

Published manuscript

Authors: Helge Oesinghaus^{*a)}, Daniel Wanken^{*a)}, Kilian Lupp^{a)}, Martina Gastl^{b)}, Martin Elsner^{c)}, and Karl Glas^{a)}

a) Water Systems Engineering, Chair of Food Chemistry and Molecular Sensory Science, TUM School of Life Sciences, Technische Universität München, Maximus-von-Imhof-Forum 2, 85354 Freising, Germany

b) Research Center Weihenstephan for Brewing and Food Quality, Technical University of Munich, Alte Akademie 3, 85354 Freising, Germany;

c) Chair of Analytical Chemistry and Water Chemistry, Technical University of Munich, Lichtenbergstraße 4, 85748 Garching, Germany

corresponding author: helge.oesinghaus@tum.de

*These authors contributed equally to this publication.

3.2.1 Abstract

Reverse osmosis (RO) is a widely used membrane technology for producing process water or tap water that is receiving increased attention due to water scarcity caused by climate change. A significant challenge in any membrane filtration is the presence of deposits on the membrane surfaces, which negatively affect filtration performance. Biofouling, the formation of biological deposits, poses a significant challenge in RO processes. Early detection and removal of biofouling are essential for effective sanitation and prevention of biological growth in RO-spiral wound modules. This study introduces two methods for the early detection of biofouling, capable of identifying initial stages of biological growth and biofouling in the spacer-filled feed channel. One method utilizes polymer optical fibre sensors that can be easily integrated into standard spiral wound modules. Additionally, image analysis was used to monitor and analyze biofouling in laboratory experiments, providing a complementary approach. To validate the effectiveness of the developed sensing approaches, accelerated biofouling experiments were conducted using a membrane flat module, and the results were compared with common online and offline detection methods. The reported approaches enable the detection of biofouling before known online parameters become indicative, effectively providing an online detection with sensitivities otherwise only achieved through offline characterization methods.

3.2.2 Introduction

Water scarcity is increasing, which can be primarily attributed to the effects of a rapidly growing world population, climate change, and increasing industrialization [B1]. Consequently, different membrane separation technologies have gained significant research attention in recent years [B2]. Among these processes, reverse osmosis (RO) stands out as an effective method for water purification, capable of

removing inorganic, organic, and pathogenic pollutants from the feed water [B3]. However, a notable drawback of such separation technologies is the formation of deposits on the surface of the membrane. Biological deposits can, for example, pose a significant challenge when raw waters with high organic loads are purified through membrane separation techniques [B4]. Microorganisms (MO) tend to adhere to the surfaces within the spiral wound membrane modules (SWM) [B5]. Once attached, these MOs rapidly produce extracellular polysaccharides (EPS) and proteins that serve as a protective barrier against cleaning and disinfection agents. Consequently, completely inactivating or cleaning the MOs from the membrane surface becomes nearly impossible [B6]. One effective strategy to address the presence of MOs and high organic loads in RO systems is the implementation of pretreatments that effectively reduce the organic components in the feed water. Therefore, advanced oxidation strategies based on peroxydisulfate are discussed as oxidizing agents that can remove organic pollutants from the water [B7]. Alternatively, inactivation of already attached MOs at an early stage can be targeted, specifically before the onset of EPS production. By intervening at this early stage, it becomes possible to rinse the MOs out of the SWM along with organic deposits. As early as 1997, Flemming et al. proposed that cleaning of RO systems should occur before biofouling impacts membrane permeability, before pressure drops in the feed channel, or before membrane biodegradation begins [B6]. Hence, a crucial requirement in any anti-fouling strategy is an early *in-situ* detection of microbial attachment. So far, however, only offline analyses can detect microbial growth in the first attaching and propagation phase. In a recent study, the biofilm formed on the surface of an RO-membrane surface was chemically characterized using ATR-FTIR spectroscopy [B4, B8]. Another suitable approach to detect a biofilm is to measure the amount of total organic carbon (TOC) [B9, B10]. A comparison of the TOC values in the feed and retentate allows us to draw conclusions about the accumulated biomass in an RO system. The number of viable MOs is represented by the parameter colony forming units (CFU), which are determined as the cultivable MOs in the water [B3]. However, determining the CFUs may be an inaccurate measure due to the presence of clustered cells or non-cultivable MOs in the water [B11]. To address this limitation, Vrouwenvelder et al. proposed measuring the concentration of adenosine triphosphate (ATP) as an additional offline parameter, as the ATP concentration is directly proportional to all viable cells present in the characterized waters or biofilms [B3, B10, B11]. However, all offline analytical methods demand significant time-, personnel-, and cost-intensive methods. For instance, the cultivation of MOs according to the German tap water regulation takes 72 h. Hence, there is a pressing need for developing *in-situ* analyses of process data and the development of methods that enable biofilm monitoring with sufficient sensitivity to detect the earliest stages of organic and MO accumulation on membrane surfaces [B11]. So far, online analyses only indirectly recognize the effects of biofilm formation in membrane processes. Vrouwenvelder et al. proposed a membrane fouling simulator (MFS) be installed prior to the first SWM in an RO plant to additionally measure changes in the feed-channel pressure drop or the permeate flux [B10]. This method can detect biofilm formation before the biofouling impacts the SWM of the RO plant [B12].

However, an MFS only measures the consequences of biofouling and does not assess the presence of MOs on the surfaces of RO membranes themselves.

1. A new fiber optical sensor for biofouling detection, which can be easily integrated into both newly constructed and existing SWMs. This sensor provides a reliable method for detecting biofouling in real time within the RO system.
2. The implementation of image analysis techniques for membrane flat modules that are often used in laboratory experiments.

Overall, the approaches present advancements in both *in-situ* biofouling detection using fiber-optical sensors within SWMs and image analysis techniques applicable to membrane flat modules, thereby enhancing our understanding of biofouling processes in RO systems.

3.2.3 Materials and methods

RO-Pilot Plant

The polymer optical fiber (POF) sensors were tested in the same RO pilot plant as previously described by some of us [B13]. The only changes made to the current RO setup were the camera position and composition of the water used for the biofouling experiments. The following figure 3.12 shows the RO pilot plant used for the present study:

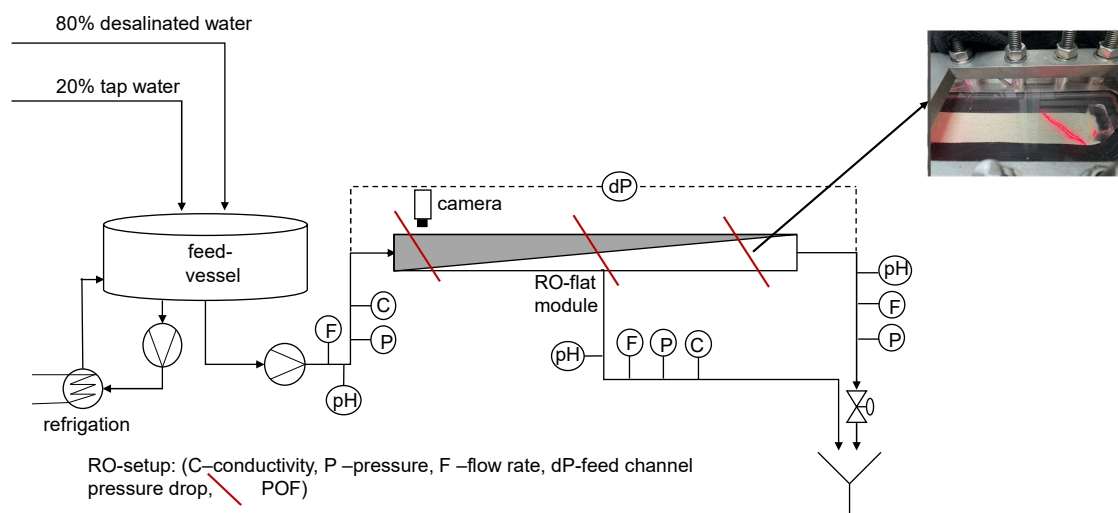


Figure 3.12: Schematic description of the reverse osmosis plant with integrated polymer optical fibers, sensors, and permeate and retentate rejection.

The camera was installed on the feed side of the RO flat module because this is the anticipated location where biofouling should start [B10]. Before every experiment, the RO plant was cleaned and disinfected using 0.1 wt% NaOH, 5 wt% citric acid, and 0.25 wt% H₂O₂. DOW XLE membranes and a Toray spacer were used for the

experiments. The membranes were compacted using a NaCl solution with a conductivity of $200 \mu\text{S cm}^{-1}$ for at least 96 h. Subsequently, the feed water (composition described below) was continuously introduced into the feed vessel. The feed water used in the experiments consisted of a mixture of Freising tap water (20%) and desalinated water (80%). This composition was chosen to prevent exceeding the calcite solubility product and to inhibit crystal formation. In addition, an autoclaved nutrient solution was added to the feed water to give concentrations (C:N:P) of $500 \mu\text{g L}^{-1}$, $100 \mu\text{g L}^{-1}$, and $50 \mu\text{g L}^{-1}$, respectively. This was achieved by dosing 3.42 mg L^{-1} sodium acetate, 1.21 mg L^{-1} sodium nitrate, and 0.39 mg L^{-1} sodium phosphate into the feed, which had an approximate flow rate of 11.5 h L^{-1} . These C:N:P concentrations were half of those used in RO systems previously reported in the literature [B3, B14]. Throughout the experiment, the retentate and permeate streams were discarded.

POF-sensor

The POF-sensor principle is presented in figure 3.13. Polymer optical fibers consist of a core made of polymethylmethacrylate (PMMA) and a fluoropolymer cladding, which maintains the total internal reflection in the fiber core. In this study, the cladding of the fiber was removed on a length of ca. 5 cm in two different methods: chemical removal with ethyl acetate or mechanical removal using a 350-grid abrasive paper. The removal of the fiber's cladding enables the interaction of light with deposits on the fiber surface. As recently demonstrated by Hager *et al.*, such a POF sensor is capable of detecting crystals on the fiber surface [B13,B15]. It is worth noting that the removal of the cladding influences the surface roughness of the fiber. This can be seen in figure 3.13, which shows a comparison of scanning electron microscopy (SEM) images of the surface observed after removing the cladding via different methods.

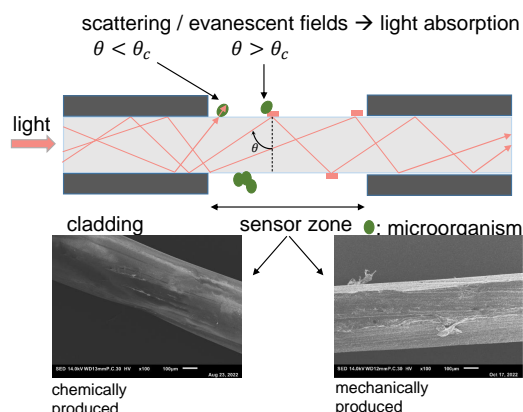


Figure 3.13: Mode of operation of the fiber-optical sensor. Top: schematic description of the optical fiber with removed fluoropolymer cladding and the two modes of interaction between light and deposits on the surface: scattering and evanescence-based attenuation. Bottom: scanning electron images (SEM) images of the sensor zone. In the left image, the cladding is removed using ethylacetate, and in the right micrograph by mechanical abrasion.

The fibers were installed below the feed spacer or as a spacer substitute. The setup with the incorporated fibers, the feed spacer, and the RO membrane is shown in figure 3.14.

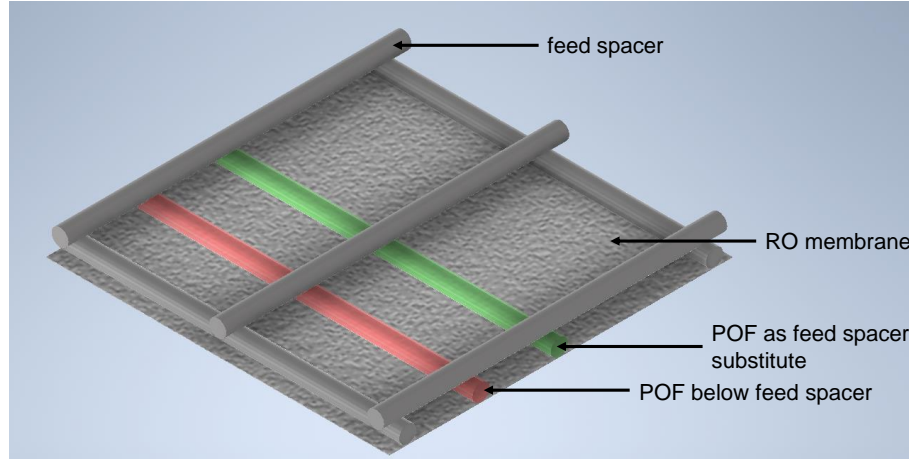


Figure 3.14: Depiction of the two polymer optical fibers that were included in a feed-spacer-square on the RO membrane surface to enable the detection of biofilm formation.

Offline analytic

The following paragraphs describe the offline analysis of the water and the biofilm formation during and after the experiments:

TOC

The analysis of the TOC content as non-purgeable organic carbon (NPOC) was carried out by the Research Center Weihenstephan for Brewing and Food Quality according to DIN EN 1484:1997-08. Using the TOC concentrations in the feed and the retentate, TOC_{Feed} and TOC_{Ret} , respectively, in combination with the flow rates in the feed and the retentate, \dot{V}_{Feed} and \dot{V}_{Ret} , respectively, the carbon rate (\dot{C}) mg L^{-1} was balanced.

$$\dot{C} = TOC_{Ret} \cdot \dot{V}_{Ret} - TOC_{Feed} \cdot \dot{V}_{Feed} \quad (3.2)$$

ATP

ATP samples were immediately frozen after sample collection by submersion in liquid nitrogen to avoid the degradation of extracellular ATP. Subsequently, frozen samples were immediately thawed and measured. Measurements of ATP content were conducted using the EnSURE TouchTM (Sundern, Germany) luminometer from Hygiena (Camarillo, US) using UltraSnapTM, AquasnapTM Total, and AquasnapTM Free testers in accordance with the manufacturer's instructions. ATP standards were prepared using adenosine 5-triphosphate disodium salt from Sigma-Aldrich Chemistry (St. Louis, US).

CFU

The determination of the colony-forming units of cultivable microorganisms at 22 and 36 °C was carried out by the Research Center Weihenstephan for Brewing and Food Quality in accordance with the norm DIN EN ISO 6222:1999-07 corresponding to § 15 (1c) of the German tap water regulation (TrinkwV).

16S rRNA

Sampling was performed after the end of the experiment by sterile swabs (Texwipe™, Kernersville, US) directly from the membrane. Samples were processed by ZIEL—Institute for Food & Health, according to Reitmeier *et al.* [B16] with primers 341F/785R. In deviation from the experimental instructions, DNA isolation was carried out after bead beating using the Maxwell RSC Fecal Microbiome DNA Kit in the MaxWell device from Promega (Walldorf, Germany).

Online analytic

Feed channel pressure drop (FCP)

The FCP value was measured using Endress & Hauser differential pressure sensors (Type PMD75).

Permeability

The permeability was calculated using the flow rate of the permeate (\dot{V}_p) with respect to the net transmembrane pressure TMP_{net} and the membrane area A .

$$P_W = \frac{\dot{V}_P}{A \cdot TMP_{net}} \quad (3.3)$$

Image analysis

A Basler ac-A3088-57uc camera with a CMOS sensor and with 6.4 MP resolution was used to take photos of the membrane surface at 1 h time intervals. The photos were taken in reflected light mode at the feed side of the membrane flat module. The light was turned on for 2 min to avoid algae growth on the membrane surface. The photos were then stored as *.tiff* data with image sizes of $2064 \times 3088 \times 3$ pixels. The terms ‘matrix,’ ‘photo,’ and ‘image’ are interchangeably used throughout the following text, as they all refer to the same visual representation. The matrices were analyzed using Matlab R2021a. The Matlab® code is organized into two steps with (A) the image registration and (B) the calculation of image similarities.

- (A) The motion of the module (due to motor movement etc.) resulted in an imperfect alignment, so the captured images corresponded to different coordinates on the membrane surface. Therefore, it was necessary to perform image registration to align the images. This process followed the four steps of image registration as outlined by Zitová and Flusser [B17]: feature detection, feature matching, transform model estimation, image resampling, and transformation.

1. A distinctive section of the photo containing specific features of a cropped reference greyscale image was manually selected.
2. The images were aligned. The Matlab function *normxcorr2* was used to create a normalized cross-correlation matrix between the selected feature image section and the sensed images of the time series, which were transformed into greyscale images. This function moves the smaller matrix containing the features across the bigger matrix to find the location via the maximum in matching [B18]. Next, parameters for further transformation, namely aligning the sensed images around the selected features, had to be extracted using the Matlab functions *find* and *max*.
3. The gained parameters were then used to align the color images. To be able to transform the images around the same coordinates, they had to be cut in size; thus, gaining room for movement. Hence, the registered images were somewhat smaller than the original ones and consisted of $1937 \times 2913 \times 3$ pixels. As a result of the registration process, all images of the time series had the same size and were centered around the same distinctive features.

The process of image registration is sketched in figure 3.15.

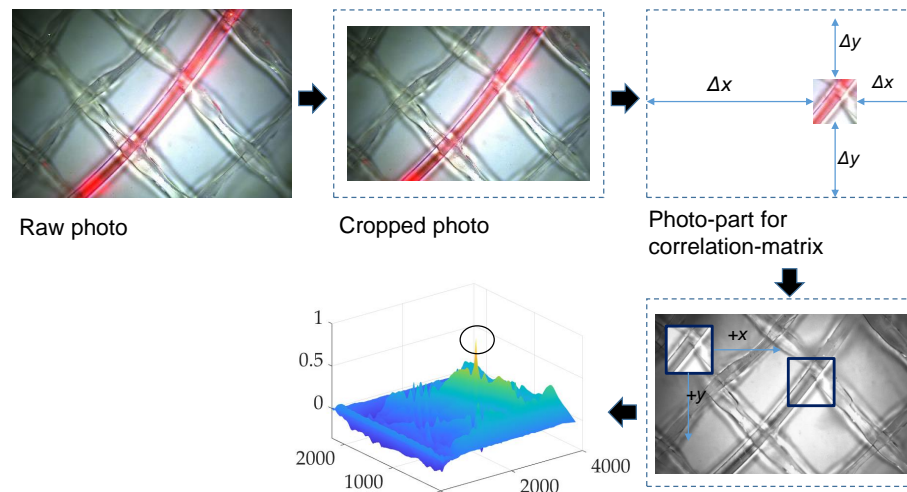


Figure 3.15: The process of image registration that was used for image analysis via the four steps of image registration described by Zitová and Flusser

- (B) A Pearson correlation coefficient is a very suitable tool to measure pixel-by-pixel image similarities [B19, B20]. Therefore, analysis of image similarities was carried out via a 2-dimensional Pearson correlation coefficient. Using our image analysis, we determined the different red, green, and blue layers of one RGB image and compared them with a reference matrix, which is the RGB image at the initial time. This photo was taken before the compaction phase ended and the feed water was changed to the tap water desalinated mixture with dosed nutrients.

A correlation coefficient for each sensed image was calculated in the time series

and for each RGB layer. The single layers were separated via the Matlab function *imsplit*, resulting in three 2D grayscale matrices, each representing one RGB layer. Next, a reference picture, matrix \mathbf{A} of size 1937×2913 , was compared with each sensed image layer, matrix \mathbf{B} of the same size, using the following equation:

$$Pearson = \frac{\sum_m \sum_n (A_{mn} - \bar{A})(B_{mn} - \bar{B})}{\sqrt{\sum_m \sum_n (A_{mn} - \bar{A})^2 \sum_m \sum_n (B_{mn} - \bar{B})^2}} \quad (3.4)$$

with A_{mn} as the reference matrix of size $m \times n$ and B_{mn} as the sensed matrix of the same size. \bar{A} and \bar{B} are the mean pixel intensities of A_{mn} and B_{mn} with $m = 1937$ and $n = 2913$. The calculated correlation coefficient serves as a measure of the deviation between an image captured at a specific time and the initial reference image, quantifying the level of similarity between the two images.

3.2.4 Results and discussion

The results are divided into three experimental parts to demonstrate the function of the POF and the image analysis for early biofouling detection on RO membranes.

Conditioning: POF-transmissions in water

The initial set of experiments aimed to demonstrate the longterm effects of POF transmission. The POFs were integrated into an RO system under normal filtration conditions, without forming deposits on the membrane and spacer surfaces. The RO system operated using a 2 g L^{-1} NaCl feed solution over the course of several days, with the retentate and permeate flowing back into the feed vessel. Figure 3.16 illustrates the time series of transmission obtained from these experiments, which were conducted in triplicate.

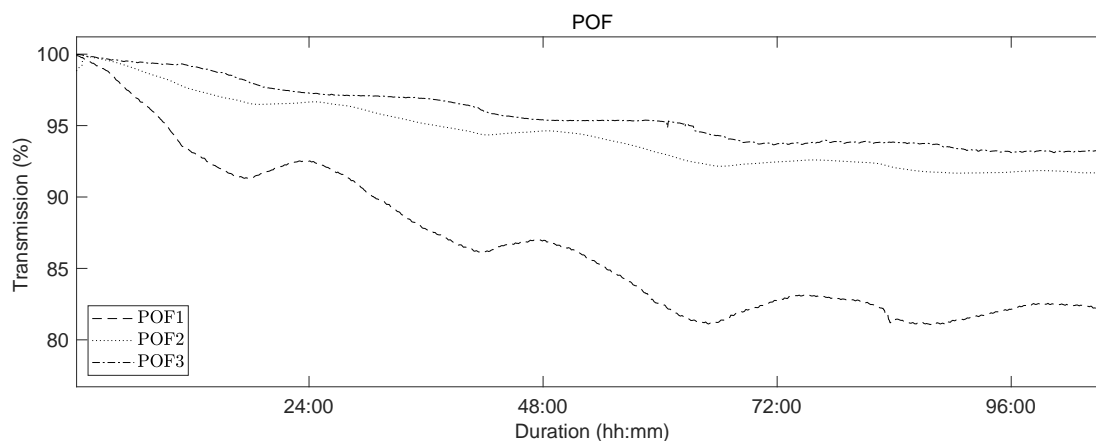


Figure 3.16: Plot showing the light transmission of POFs as a function of time. The feed in the experiment was an aqueous NaCl solution (2 g L^{-1}).

The recorded time series clearly show an asymptotically decreasing light transmission. The magnitude of the total decrease varied among the three experimental runs. In all experiments, the decrease in light transmission ends after ca. 72 h and a limiting value appears to be reached after 96 h. Additionally, all three recorded time series exhibit daily variations. These variations are attributed to the daily cycle of temperature fluctuations, which result in changes in the mechanical stresses experienced by the membrane flat module, due to a differential thermal expansion of the metal screws used to compress the module. These findings are in line with previous reports that have documented a similar influence of water adsorption and mechanical stress on the light transmission of POFs [B2, B21, B22].

First validation: POF-sensors in a yeast suspension

The second series of experiments aimed to investigate the impact of viable cells and organic suspensions on the light transmission of the POFs. In contrast to the above-described experiment, the POF was not installed in the RO-flat module but in a water bath, to which a yeast suspension was added after a conditioning period of 71 h. Two fibers were installed in the water bath: a reference fiber with intact fluoropolymer cladding and a sensor fiber with mechanically removed cladding. Figure 3.17 shows representative results of one of the three experimental runs with this setup.

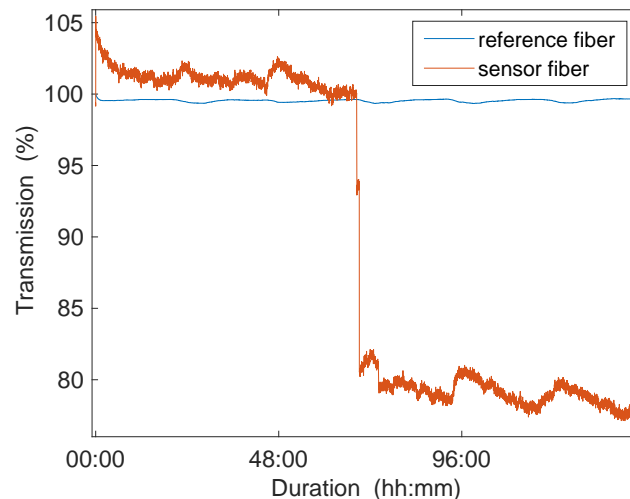


Figure 3.17: Change in transmitted light intensity as a function of time for POF sensors that were immersed in a water bath, to which yeast was added after a conditioning period of 71 h.

Figure 3.17 shows a plot of the recorded transmission over time. The plot shows a nearly constant time series for the transmission of light through the reference fiber over the course of the whole experiment. The plot for the sensor fiber, by contrast, showed a sharp drop in the intensity of transmitted light upon the addition of yeast to the water bath. Hence, the light transmission was significantly influenced by the presence of viable cells. The other two experiments gave similar results. As

previously observed, both time series showed small intensity fluctuations over the course of 24 h due to the daily temperature cycle. The conditioning period ended earlier than in the setup where the POFs were installed in the membrane flat module (see section 3.2.4). The yeast was added to a water bath and therefore the POFs were not installed in the membrane flat module, where the screws of the module compress the POFs. The absence of screw pressure (as illustrated in Figure 3.12)) may have facilitated the adaption of the POFs to the experimental conditions.

Second validation: Biofilm detection in the RO pilot plant

In this following section, the capability of the selected POF sensor and our image analysis approach toward detecting biofouling in RO systems at an early stage is evaluated and compared with current online detection methods. Prior to the experiments, the POF sensors were conditioned for at least 96 h using a NaCl solution to avoid any effects on the intensity of transmitted light due to water adsorption or mechanically induced transmission loss. The experiment was executed three times. Because the results of all experiments were very similar (see figure 3.21), we will focus on discussing the findings from one experiment. Figure 3.18 shows the time series of the measured online parameters. The vertical dotted line marks the end of the conditioning and compaction phase; this also marks the moment the dosing of nutrients was started and the switch in feed composition to a mixture of tap water and desalinated water. Figure 3.18 displays the recorded time series from 96 h onwards, at which point the POF transmission reached a steady-state level (see section 3.2.4).

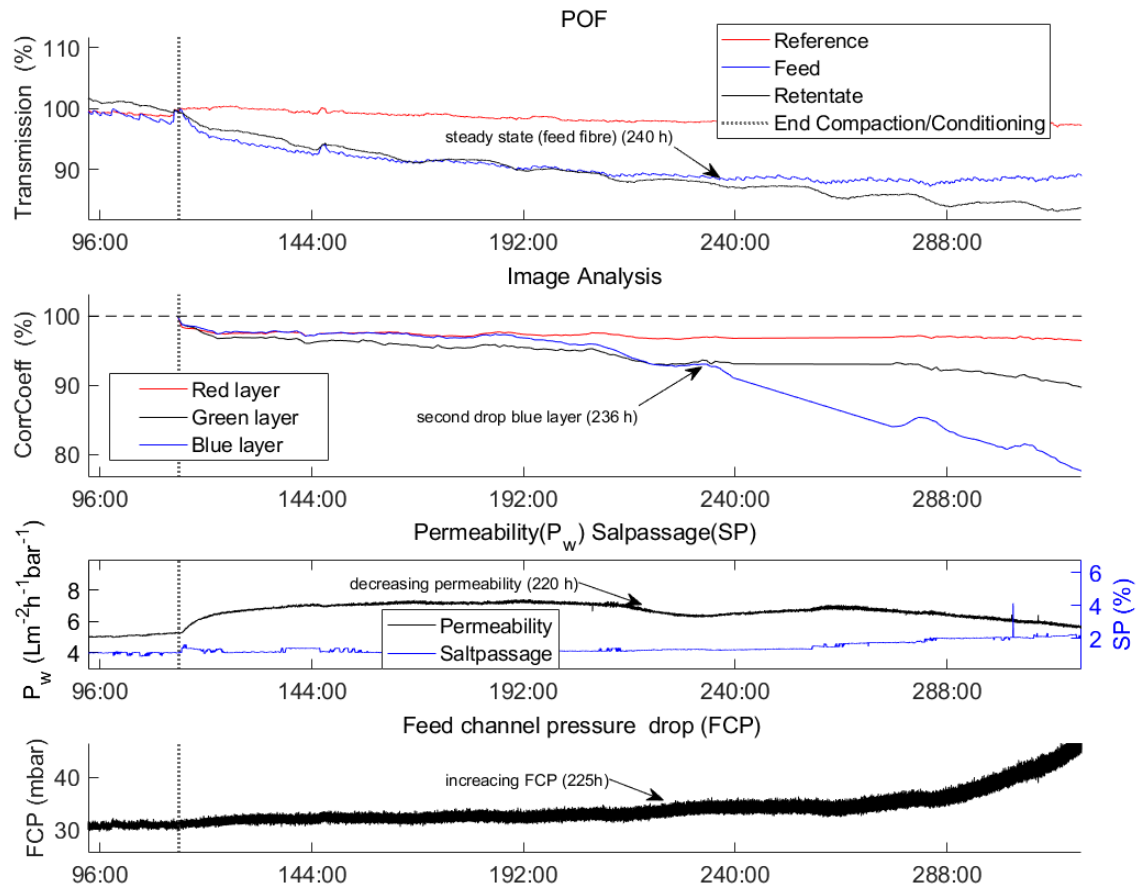


Figure 3.18: Time series showing the evolution of different selected online parameters. Experimental conditions: dosed nutrients (500, 100, 50) (C:N:P) in feed water (20% tap water, 80% desalinated water) from 144 h onwards.

The analysis of the recorded time series shows the effect of biofouling at a very early stage. After the feed water change, the monitored online parameters exhibited changes in the following temporal order: first, the POF's light transmission was affected; then, the correlation coefficient from the image analysis; subsequently, the permeability; and finally, the FCP value was affected. This temporal order is described in the following paragraphs, assuming that biological growth affected the parameters.

The light intensity transmitted by the POFs on the feed and the retentate side immediately decreased after the end of compaction and with the onset of dosing nutrients to the changed feed solution. The POF's light transmission on the feed side of the membrane module stopped decreasing and reached a steady-state level from 240 h onwards while the retentate fiber's light transmission continued to decrease.

The correlation coefficients determined by the image analysis followed a similar trend as the transmission of the POF sensors until 240 h. Subsequently, and nearly simultaneously with the changes in permeability and FCP, the correlation coefficient of the blue layer in the RGB image experienced a significant decrease. This observation could potentially indicate the onset of a phase of exponential growth of a biofilm on the membrane surface. By contrast, the correlation coefficient of the green layer

only slightly decreased over the course of the whole experiment, whereas the correlation coefficient of the red layer remained at an almost constant level after the slight decrease following the nutrient dosage. The variations in the correlation coefficients determined for the R-, G-, and B-layers demonstrate that a separate evaluation of the color layers of the images is crucial for detecting biofouling. Furthermore, the differences in the correlation coefficients show the color and brightness shift from white to brown, which were indicative of the growth of a biofilm.

Figure 3.18 shows that permeability first increased and later (220 h) decreased. The increased permeability can be attributed to pH-dependent membrane surface charges, which changed as a result of the increase in pH from 6.9 to 8 after the compaction, in agreement with previous reports [B23, B24].

The FCP value was observed to increase after 221 h, with the increase becoming more pronounced over time.

The only parameter that stayed almost at a constant level over the course of the experiment was the salt passage. This indicates the absence of scaling on the RO membrane. The absence of any crystals on the membrane was independently confirmed by SEM imaging (not shown here).

All the observed parameter changes indicate an increasing level of biofouling on the membrane and spacer surfaces. As known from the literature, the MOs adhere first to the feed spacers and therefore to the POFs, which correlates with the initial changes observed in the POF transmission and the image analysis [B25]. Moreover, the biofilm started growing on the feed side of the membrane module and later on the retentate side. This phenomenon can be observed from the signal of the two POF sensors. The transmitted light of the POF on the feed side decreases first. The stabilization of the signal at a steady-state level suggests that the biofilm may have completely covered the fiber surface. On the retentate side, the light transmission through the fiber sensor exhibited a more prolonged decrease compared with that of the feed fiber, indicating a delayed biofilm growth on the retentate side. After ca. 236 h, the biofilm had developed on the membrane surface, which reduced the flux and consequently the permeability. Only a few hours later, the correlation coefficient of the blue layer in the image analysis showed a second drop.

Because the growth of the biofilm was more pronounced in the feed channel, the pressure progressively decreased. In our experiment, the change in pressure was the last parameter to indicate biofouling. The weak increase observed at the beginning of the experiment was not statistically significant compared with its strongly fluctuating signal. To validate and compare the POF with offline analytics, which are commonly used to indicate and measure microbial growth in RO plants [B3, B9–B11], a comparison with the measured offline parameters was carried out, as shown in figure 3.19.

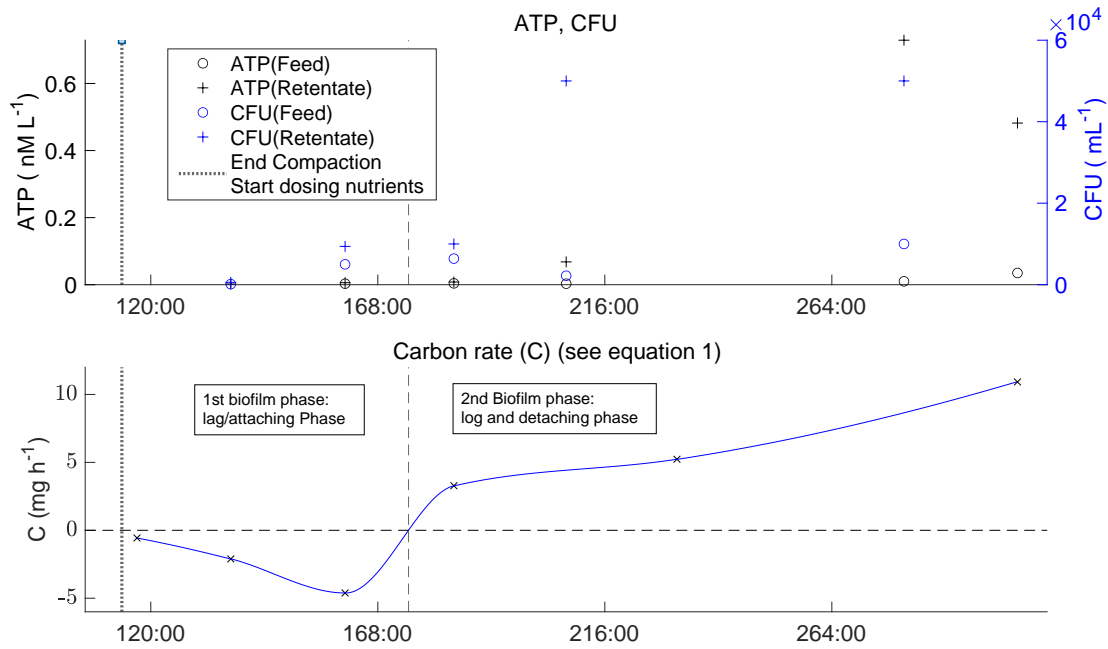


Figure 3.19: Plots of offline parameters of the biofouling experiment (see figure 3.18).

The offline parameters measured at different times indicate the different phases of biofilm formation in the membrane flat module.

First, the negative carbon rate and relatively low CFUs indicate the adhesion and growing phase of the MOs. This initial biofouling phase ended after ca. 160 h, when the CFU in the retentate started to increase compared with the feed values. Furthermore, the carbon rate turned to a positive level. Later, after 207 h, the ATP concentration in the retentate increased compared with the ATP concentration in the feed. Notably, however, the ATP value was very low due to the low cell concentration, and it, therefore, remained difficult to precisely measure the ATP concentration.

All the changes observed in these parameters mark the beginning of the second phase of biofouling, the detaching phase, when parts of the biofilm detach from surfaces inside the membrane flat module. At this stage, the MOs, together with the EPS, flow out of the membrane flat module and cause a positive carbon rate and higher contents of viable MOs in the retentate, consequently increasing the ATP concentration. The determined values indicate that this stage reached a steady-state mode when the biofilm inside the RO module reached a constant thickness. This equilibrium was indicated by the ATP concentrations and CFU in the retentate that ceased to increase, corroborating that the mass of growing biofilm and detaching biofilm are balanced.

The comparison of offline parameters with the new online parameters determined via the integrated POF sensors and through image analysis validates the new sensors' functionality. Simultaneously to the negative carbon rate, the POF signal decreased

in parallel with the correlation coefficient from the image analysis. When the second phase began, the image analysis showed a sharp drop in the correlation coefficient of the blue layer, and the POF sensor on the feed side turned to a steady-state level (244 h). The steady-state mode of the retentate fiber from 244 h onward may be caused by a completely overgrown surface of the POF. This observation is in agreement with previous findings [B10]. In the final step, the MOs in the biofilm are compared with the MO found in other RO plants known from the literature. Biofilms are composed of an assemblage of MO at a boundary layer consisting of either a mixed population or individuals of a single species [B26]. Typical species found in biofilms on RO membranes belong to ubiquitous aquatic microorganisms. These include organisms of the classes *Alphaproteobacteria* (for example, order/family/genus *Rhizobiales/Bradyrhizobiaceae/Rhodopseudomonas* or *Sphingomonadales/Sphingomonadaceae/Sphingomonas*), *Betaproteobacteria* (for example, *Burkholderiales/Comamonadaceae/Acidovorax*), and *Gamma proteo bacteria* (*Pseudomonadales/Pseudomonadaceae/Pseudomonas* or *Xanthomonadales/Xanthomonadaceae/Pseudoxanthomonas*) [B3, B27–B29]. Identification of MOs can be achieved through various methods, including through culturing techniques (e.g., plate cultures) in combination with Matrix-Assisted Laser Desorption/Ionization Time-Of-Flight (MALDI-TOF) mass spectrometry analysis or by 16S rRNA sequencing, and by other methods. However, MALDI-TOF spectrometry has the disadvantage that cultivability of the organisms is required, which is not always given. On the other hand, 16S rRNA sequencing allows for a fairly accurate estimation of the cultures contained in the biofilm based on highly conserved RNA segments, but no statement can be made about the viability of the detected organism within the biofilm [B30]. Here, we chose 16S rRNA sequencing to analyze the species contained in the biofilm. Table 3.5 provides an overview of the microbiological composition of the biofilm. Most of the identified microorganisms (85%) belong to Alpha- and Gammaproteobacteria. Most dominant were the bacteria of the class Gammaproteobacteria, which accounted for 58% of the detected bacteria. Typical biofilm formers such as *Acidovorax*, *Pseudomonas*, and *Pseudoxanthomonas* were detected in the forced biofilm formation experiments. The presence of bacteria of the class Bacteroida was also characteristic of biofilms in membrane processes [B31].

Table 3.5: Relative abundances of MOs from a 16S rRNA analysis of a biofilm on the RO membrane after a 3-week experiment. Not italic: comments to the MO.

Phylum	Class	Order	Family	Genus
<i>Proteobacteria</i>	<i>Gamma</i> proteobacteria (typical biofilm formers)	<i>Burkholderiales</i>	<i>Commamonadaceae</i>	48% <i>Aquabacterium</i>
				29% <i>Acidovorax</i>
			<i>Rhodocyclaceae</i>	3% <i>Deftla</i>
				3% <i>Ferribacterium</i>
			<i>Burkholderiaceae</i>	2% <i>Cupriavidus</i>
				3% <i>Pseudoxanthomonas</i>
			<i>Xanthomonadaceae</i>	0.8% <i>Stenotrophomonas</i>
				0.8% <i>Acinetobacter</i>
			<i>Pseudomonales</i>	1% <i>Pseudomonas</i> (human pathogenic)
				6% <i>Cualobacter</i>
<i>Alphaproteobacteria</i> (typical biofilm formers)			<i>Caulobacteraceae</i>	0.7% <i>Phenylebacterium</i>
			<i>Sphingomonadaceae</i>	0.8% <i>Sphingopyxis</i> 1% <i>Rhodobacter</i>
	<i>Bacteroidia</i>			0.8% <i>Cytophaga</i> (Coexisting within potable water biofilms[B31])

In all experiments, the bacteria present in the drinking water pipe system led to a bacterial community comparable to that in industrial full-scale RO plants. Hence, our new methods should be suitable for typical biofouling detection in other RO plants.

Practical test: POF-sensors as indicators of cleaning-in-place

In the following, insight into possible applications of the POF as a biofouling sensor are provided. The early detection capability of the POF sensors enables the control of a cleaning-in-place (CIP) procedure for membrane modules. This cleaning process is crucial to be carried out before the biofilm significantly impacts the permeability or the feed-channel pressure drop. By implementing effective CIP procedures based on early detection using POF sensors, sustainable desalination through RO membranes can be achieved, even for water sources with high organic loads. Figure 3.20 shows results from an experiment conducted under accelerated standard conditions, as described in section 3.2.4, illustrating the onset of biofouling in this scenario.

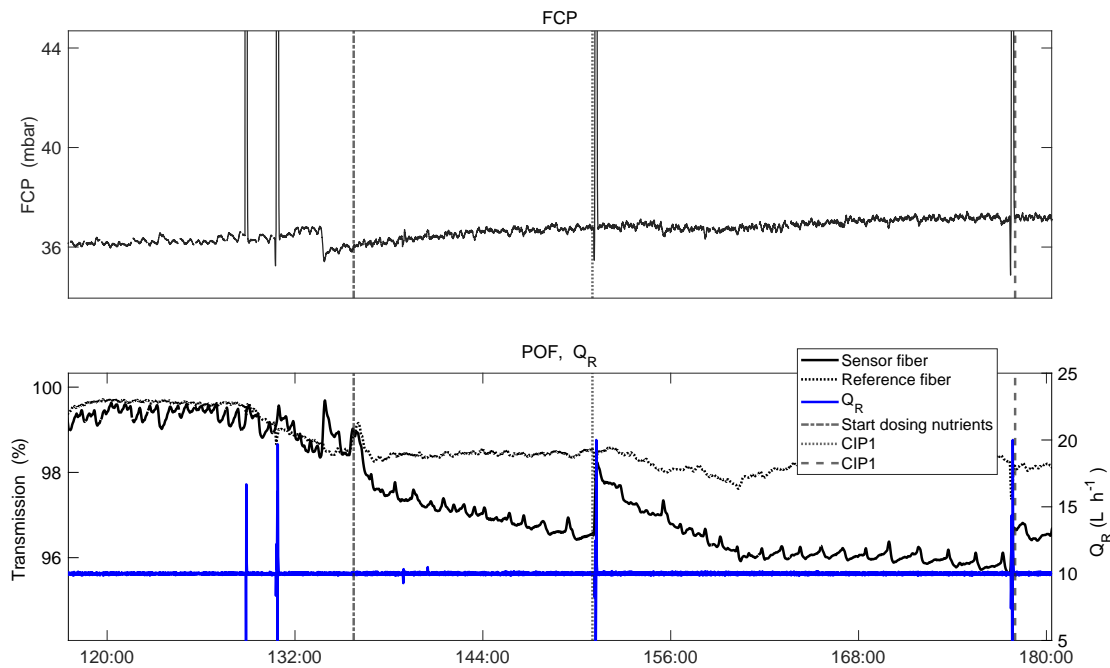


Figure 3.20: Plot of a time series from an experiment with cleaning-in-place (CIP) achieved by higher cross-flow velocities on an RO-Membrane with a POF sensor for monitoring and control.

Figure 3.20 shows four time series. On top, the feed channel pressure drop is shown, which has been conventionally used to detect biofouling in spacer-filled feed channels in RO modules. The FCP value remains relatively constant as it is only influenced by the CIP intervals due to Moody's law. The lower diagram provides the time series of the new POF sensors. The sensor POF shows the typical descending behavior when biofouling occurs. Furthermore, a higher cross-flow velocity (displayed by Q_{Ret}) at 128 and 131 h did not influence the POF signals because no nutrients were dosed to the water and the feed water was not yet polluted with microbial load. Because the nutrients were dosed after the compaction and conditioning phase, the POF's transmission signal began to immediately decrease compared with the reference fiber. At 151 and 178 h, two CIP intervals were executed. In Figure 3.20, it can be observed that the transmission signal of the POF sensor recovers after each CIP interval. However, the magnitude of the recovery is lower during the second CIP interval. This could be attributed to the presence of increased quantities of the EPS matrix within the biofilm, which provides stability and protection against mechanical cleaning. Prior to the second CIP interval, the signal of the POF sensor reached a steady-state level, potentially indicating a complete coverage of the fiber surface by the biofilm. This observation supports the hypothesis of a stronger EPS matrix within the biofilm during advanced stages of biofouling growth.

3.2.5 Conclusion

This publication highlights the advantages of combining two novel detection methods for earlystage biofouling monitoring in RO modules. The methods are introduced, their effectiveness is demonstrated, and their benefits are evaluated in comparison with conventional detection methods. By utilizing these new detection methods, it becomes possible to detect and address biofouling at an early stage, enabling more effective management and prevention strategies in RO systems.

1. Image analysis can quantify the color changes caused by microbial growth at a very early stage. A preparatory step is needed to adjust the photo's positions to the reference images recorded during the conditioning phase. A 2-dimensional Pearson correlation coefficient of the R-, G-, and B-layers was calculated for each photograph of the whole experimental series and compared with the reference image. This results in a time series of image analysis parameters that can be recorded while biofouling is affecting the RO process.
2. Polymer optical fibers are a new method to detect biofouling throughout the entire growth period. The detection process requires the use of conditioned fibers and enables the qualitative detection of biological growth until the fiber surface is completely covered with biomass. The time series of the transmitted light through the fibers strongly differs from the changes observed in fibers used to monitor scaling (inorganic deposit) on the RO membrane.

Figure 3.21 provides a visual representation of the early detection and compares the sensor signals that indicate biofilm presence by means of different detection methods. The changes in the time series of the sensor signals occur at similar points in time. Image analysis and the POF's light transmission indicate the biofouling formation first.

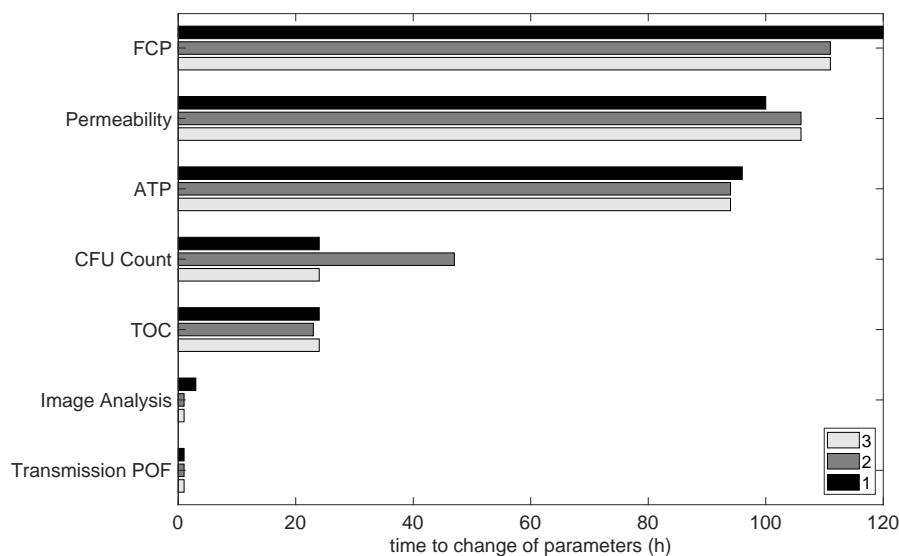


Figure 3.21: Comparison of parameter changes during the triplicate of biofouling experiments in the RO plant. Time starts when dosing nutrients to the tap water/desalinated water mixture.

It should be noted, however, that the exact mechanism behind the POF sensors and their detection of biological growth remains uncertain. It is unclear whether the light transmission is influenced by changes in evanescence or if the light is scattered out of the fiber due to inhomogeneities in the biofilm and resulting refractive index changes. Further research is needed, especially with fiber optic sensors based on fluorescence measurements of organic pollutants on the fibers and feed spacers. This may lead to a species-sensitive measurement of forming biofilms due to the different metabolism products of various bacterial species.

Author Contributions Conceptualization, H.O. and D.W.; methodology, H.O., D.W., and K.L.; software, H.O., D.W., and K.L.; validation H.O. and D.W.; formal analysis, H.O.; investigation, H.O. and D.W.; resources, H.O. and M.G.; data curation, H.O., D.W., and K.L.; writing original draft preparation, H.O. and D.W., writing—review and editing, H.O., D.W., K.G., and M.E.; visualization, H.O. and D.W.; supervision, K.G. and M.E.; project administration, H.O. and K.G.; funding acquisition, K.G. and M.E. All authors have read and agreed to the published version of the manuscript.

Funding The German Ministry of Economic Affairs and Climate Action (BMWK), grant number KK5022305CR0, founded this study.

Acknowledgments : The authors wish to thank Heribert Voit (Endress + Hauser GmbH+Co. KG) for the good cooperation and the rental of sensors to execute the experiments. Furthermore, the authors wish to thank Dietmar Schulte (Gullimex GmbH) for the rental of ATP-measuring devices and for sponsoring ATP test kits.

Conflicts of Interests The authors declare no conflict of interest. The founders had no influence in the design of this study, the experiments, the analyses, in writing of the manuscript, or in the decision to publish the results.

3.2.6 References

- [B1] P.S. Goh, W.J. Lau, M. Othman, A.F. Ismail, Membrane fouling in desalination and its mitigation strategies, *Desalination* 425 (2018) 130–155.
- [B2] R. Baten, K. Stummeyer, How sustainable can desalination be?, *Desalination and Water Treatment* 51 (2013) 44–52.
- [B3] P. Sperle, C. Wurzbacher, J.E. Drewes, B. Skibinski, Reducing the Impacts of Biofouling in RO Membrane Systems through In Situ Low Fluence Irradiation Employing UVC-LEDs, *Membranes* 10 (2020).
- [B4] H.-C. Flemming, G. Schaule, T. Griebe, J. Schmitt, A. Tamachkiarowa, Biofouling—the Achilles heel of membrane processes, *Desalination* 113 (1997) 215–225.
- [B5] A.F. Ismail, K.C. Khulbe, T. Matsuura, RO Membrane Fouling, in: *Reverse Osmosis*, Elsevier, 2019, pp. 189–220.
- [B6] H.-C. Flemming, Reverse osmosis membrane biofouling, *Experimental Thermal and Fluid Science* 14 (1997) 382–391.
- [B7] J. Schmitt, Nivensm D., D.-C. White, H.-C. Flemming, Changes of biofilm properties in response to sorbed substances — An ftr-atr study, *Water Science and Technology* 32 (1995).
- [B8] Matin, Z. Khan, S. Zaidi, M.C. Boyce, Biofouling in reverse osmosis membranes for seawater desalination: Phenomena and prevention, *Desalination* 281 (2011) 1–16.
- [B9] J.S. Vrouwenvelder, S.M. Bakker, L.P. Wessels, J. van Paassen, The Membrane Fouling Simulator as a new tool for biofouling control of spiral-wound membranes, *Desalination* 204 (2007) 170–174.
- [B10] J.S. Vrouwenvelder, S.A. Manolarakis, J.P. van der Hoek, J.A.M. van Paassen, W.G.J. van der Meer, J.M.C. van Agtmaal, H.D.M. Prummel, J.C. Kruithof, M.C.M. van Loosdrecht, Quantitative biofouling diagnosis in full scale nanofiltration and reverse osmosis installations, *Water research* 42 (2008) 4856–4868.
- [B11] C. Dreszer, H.-C. Flemming, A.D. Wexler, A. Zwijnenburg, J.C. Kruithof, J.S. Vrouwenvelder, Development and testing of a transparent membrane biofouling monitor, *Desalination and Water Treatment* 52 (2014) 1807–1819.
- [B12] C. Dreszer, J.S. Vrouwenvelder, A.H. Paulitsch-Fuchs, A. Zwijnenburg, J.C. Kruithof, H.-C. Flemming, Hydraulic resistance of biofilms, *Journal of Membrane Science* 429 (2013) 436–447.
- [B13] S. Hager, A. Bachmann, T. Hofmann, R. Engelbrecht, K. Glas, CaCO₃ deposits in reverse osmosis Part I - Shortcomings of current approaches leading to a new prediction model and monitoring device, *Brewing science* (2021) 122–133.
- [B14] S. Reitmeier, S. Kiessling, K. Neuhaus, D. Haller, Comparing Circadian Rhythmicity in the Human Gut Microbiome, *STAR protocols* 1 (2020) 100148.
- [B15] B. Zitová, J. Flusser, Image registration methods: a survey, *Image and Vision Computing* 21 (2003) 977–1000.
- [B16] D. Wright, Pseudo feature point registration of pavement images, *Journal of Traffic and Transportation Engineering (English Edition)* 5 (2018) 254–267.
- [B17] S. Mohapatra, J.C. Weishaar, Modified Pearson correlation coefficient for two-color imaging in spherocylindrical cells, *BMC bioinformatics* 19 (2018) 428.
- [B18] K. Pearson, VII. Mathematical contributions to the theory of evolution.—III. Regression, heredity, and panmixia, *Phil. Trans. R. Soc. Lond. A* 187 (1896) 253–318.

- [B19]K. Peters, Polymer optical fiber sensors—a review, *Smart Mater. Struct.* 20 (2011) 13002.
- [B20]D.J. Webb, Fibre Bragg grating sensors in polymer optical fibres, *Meas. Sci. Technol.* 26 (2015) 92004.
- [B21]Y.-H. La, R. Sooriyakumaran, D.C. Miller, M. Fujiwara, Y. Terui, K. Yamanaka, B.D. McCloskey, B.D. Freeman, R.D. Allen, Novel thin film composite membrane containing ionizable hydrophobes: pH-dependent reverse osmosis behavior and improved chlorine resistance, *J. Mater. Chem.* 20 (2010) 4615.
- [B22]M. Stolov, V. Freger, Membrane Charge Weakly Affects Ion Transport in Reverse Osmosis, *Environ. Sci. Technol. Lett.* 7 (2020) 440–445.
- [B23]J.S. Vrouwenvelder, D.A. Graf von der Schulenburg, J.C. Kruithof, M.L. Johns, M.C.M. van Loosdrecht, Biofouling of spiral-wound nanofiltration and reverse osmosis membranes: a feed spacer problem, *Water research* 43 (2009) 583–594.
- [B24]J. Simon Vrouwenvelder, J. Kruithof, M. van Loosdrecht, Biofouling of spiral wound membrane systems, *Water Intell Online* 10 (2011) 9781780400990.
- [B25]H.J. de Vries, A.J.M. Stams, C.M. Plugge, Biodiversity and ecology of microorganisms in high pressure membrane filtration systems, *Water research* 172 (2020) 115511.
- [B26]O. Sánchez, Microbial diversity in biofilms from reverse osmosis membranes: A short review, *Journal of Membrane Science* 545 (2018) 240–249.
- [B27]M. Herzberg, M. Elimelech, Physiology and genetic traits of reverse osmosis membrane biofilms: a case study with *Pseudomonas aeruginosa*, *The ISME journal* 2 (2008) 180–194.
- [B28]B. Buszewski, A. Rogowska, P. Pomastowski, M. Złoch, V. Railean-Plugaru, Identification of Microorganisms by Modern Analytical Techniques, *Journal of AOAC International* 100 (2017) 1607–1623.
- [B29]L.A. Bereschenko, G.H.J. Heilig, M.M. Nederlof, M.C.M. van Loosdrecht, A.J.M. Stams, G.J.W. Euverink, Molecular characterization of the bacterial communities in the different compartments of a full-scale reverse-osmosis water purification plant, *Applied and environmental microbiology* 74 (2008) 5297–5304.

Disclaimer/Publisher’s Note: The statements, opinions and data contained in all publications are solely those of the individual author(s) and contributor(s) and not of MDPI and/or the editor(s). MDPI and/or the editor(s) disclaim responsibility for any injury to people or property resulting from any ideas, methods, instructions or products referred to in the content.

3.3 Analytical characterization of damage in reverse osmosis membranes caused by components of a chlorine dioxide matrix

The research article “Analytical characterization of damage in reverse osmosis membranes caused by components of a chlorine dioxide matrix” was published in “Desalination and Water Treatment” in 2024 (doi: 10.1016/j.dwt.2024.100633) [3]. H. Oesinghaus developed the concept and co-wrote the manuscript, a revised version of which was re-submitted to the journal on 29.07.2024. H. Oesinghaus analyzed the data, optimized the methylene blue membrane permeation test, and improved the quantitative ATR-FTIR analysis methods.

The work in this chapter presents an experimental study on degradation processes in RO membranes caused by components of *in-situ* produced chlorine dioxide. Reported studies on RO membranes typically investigate the effects of *ex-situ* manufactured chloride dioxide in the form of an acidic chlorine dioxide disinfectant solution. In contrast, the effects of *in-situ* manufactured chlorine dioxide on RO membranes are poorly understood, despite the fact that *in-situ* produced chlorine dioxide is by far the more common form used in industrial settings [138]. Thus, the present chapter aims to shed light on this highly relevant but understudied class of chloride dioxide by investigating all the known by-products of industrial, *in-situ* manufactured chlorine dioxide. The extent to which these individual by-products harm conventional RO membranes was investigated and listed here in descending order starting with the most harmful: chlorite, persulfate, pure chlorine dioxide, and free chlorine. On the other hand, some by-products of chlorine dioxide, for example chlorate, chloride, and sulfate ions, do not typically damage RO membranes. The present chapter takes a comparative analytical approach to determine the factors governing the detrimental interactions, or lack thereof, between these by-products and RO membranes. The results of this analysis inform the design of a more membrane-compatible, chlorine dioxide-based disinfectant solution, and the process parameters were adapted to minimize mechanical stress on the membrane during disinfection.

Furthermore, different approaches for analyzing the membrane damages are compared, giving a more in-depth understanding of the membrane degradation process and identifying the disinfection methods that most heavily impact the structural integrity of the aramid layer of RO membranes. The membrane areas responsible for a lower retention capacity of the membrane were identified by combining results from a methylene blue test with large-area SEM images. Chemical changes in the membrane surface were characterized by both ATR-FTIR analysis and XP spectroscopy and were found to correlate with the retention capacity of the membrane. The results are finally contextualized using established theories for the chemical changes caused by chlorine dioxide to aramid membranes, and modifications to these theories are proposed.

This work paves the way for an improved reverse osmosis process that strikes a balance between disinfection efficiency and membrane integrity, thus offering an ecologically sustainable water purification solution.

Published manuscript

Authors: Helge Oesinghaus^{*a)}, Eva Eleonora Eiden^{a)}, Tim Kratky^{b)}, Maximilian J. Huber^{c)}, Stephen Schrettl^{d)}, Stephanie Holz^{e)} Martin Elsner^{c)}, and Karl Glas^{a)}

a) Water Systems Engineering, Chair of Food Chemistry and Molecular Sensory Science, TUM School of Life Sciences, Maximus-von-Imhof-Forum 2, 85354 Freising, Germany

b) Physical Chemistry with Focus on Catalysis, TUM School of Natural Sciences, Lichtenbergstraße 4, 85748 Garching, Germany

c): Institute of Water Chemistry, TUM School of Natural Sciences, Lichtenbergstraße 4, 85748 Garching, Germany

d): Functional Materials for Food Packaging, TUM School of Life Sciences, Maximus-von-Imhof-Forum 2, 85354 Freising, Germany

e): Dr. Küke GmbH, Langer Acker 33, 30900 Wedemark, Germany

3.3.1 Abstract

Reverse osmosis (RO), an important membrane technology for producing process and tap water, faces challenges due to biofilms formed by viable microorganisms, which significantly impair membrane performance. Disinfection is commonly employed to suppress biofilm formation but can also damage the crucial selective upper layer of the membrane. The present study aims to improve and compare analytical methods for detecting membrane damage to aid the design of targeted disinfection approaches that do not compromise RO efficiency. To achieve this, the accompanying byproducts of *in-situ* formed chlorine dioxide are analyzed individually with regards to their harmfulness for RO membranes. Combined insights from ATR-FTIR investigations, the methylene blue (MB) dye test, and XPS measurements enable a systematic assessment of the chemical constituents in the chlorine dioxide, ranking their harmfulness as: chlorite < persulfate < purified chlorine dioxide < free chlorine. Further investigations reveal that mechanical stress in the form during disinfection significantly accelerates membrane damage during disinfection. The results of this study pave the way for improved RO processes that account for the effects of chemical by-products and mechanical stresses to balance disinfection efficacy and membrane integrity for environmentally sustainable water purification solutions.

3.3.2 Introduction

The scarcity of fresh water in many regions of the world, exacerbated by the effects of industrialization, agricultural irrigation, and a growing world population, has made water purification an urgent global concern [C1–C3]. Commonly exploited reservoirs for fresh water are expended and increasingly polluted [C3], which has

significantly spurred interest in various membrane separation technologies [C2,C4]. Among such purification processes, reverse osmosis (RO) stands out as an effective method capable of removing inorganic, organic, and pathogenic pollutants from feed water [C5,C6].

Membranes used for RO separation processes are typically comprised of a polyester base, a polyethersulfone support, and a thin layer (10–200 nm) of an aromatic polyamide (aramid, see Figure 3.22). The latter is crucial for the diffusion-driven filtration process [A7], and rejects up to 99 % of the ions dissolved in the feed water.

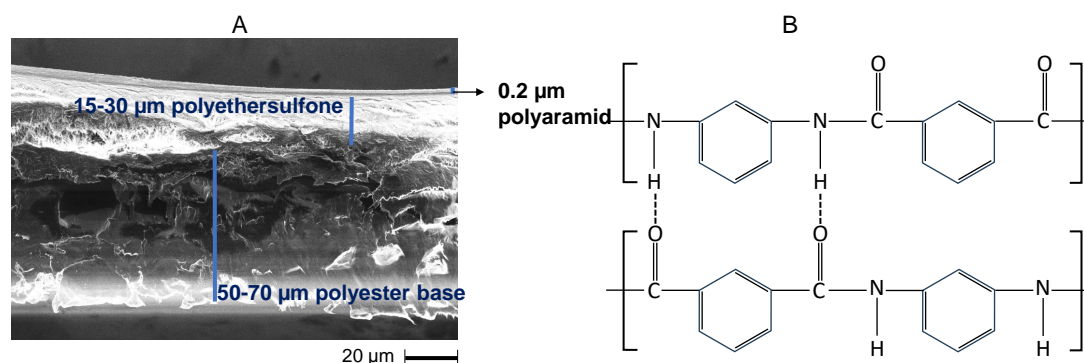


Figure 3.22: (A) Scanning electron microscopy (SEM) cross-section of a compacted DOW XLE reverse osmosis (RO) membrane with the typical layers comprising a polyester base, a polyethersulfone support, and the aramid layer. (B) Chemical structure of the aromatic polyamide (meta-aramid) that is used as a separating layer in RO membranes. Typical RO membranes feature a 10–200 nm thick layer of meta-aramid, which rejects 99 % of the ions dissolved in the water feed.

While high rejection rates are desirable in RO membrane purification systems to effectively remove water impurities, this also leads to an increased concentration of water constituents at the membrane surface [C6,C8–C10]. This effect renders the membranes vulnerable to different types of fouling [C11], among which biological fouling is a prominent mechanism that impedes the efficiency of RO technology. Indeed, the challenge of limiting bio-fouling has attracted considerable research attention, with efforts particularly focused on the sanitation of feed water and the membranes by using selected disinfectants [C12–C17]. Such disinfection schemes, however, face a significant challenge: the oxidative conditions not only reduce viable microorganisms populations, but they can severely damage the selective aramid layer of the RO membranes.

While chlorine is the most frequently studied disinfectant [C13,C18–C21], monochloramine and chlorine dioxide (ClO_2) are being explored as emerging alternatives [22–24]. In particular, the latter are proposed as chlorine alternatives that are less damaging to RO membranes. However, while the role of free chlorine in membrane degradation is well understood, only a few studies have conducted a detailed analytical characterization of the mechanisms underlying damage caused by chlorine dioxide. A focus has been on changes in the rejection capacity of RO membranes during disinfection with ClO_2 [C23] as well as on changes in the surface charge and

atomic composition of RO membranes at different pH values [C24]. To the best of our knowledge, the latter study is the only one that has proposed a reaction mechanism for chlorine dioxide with the aramid layer. Furthermore, the salt passage of RO membranes during disinfection with ClO_2 has been correlated with a characterization by IR spectroscopy [C17]. Comparing these different studies would be beneficial to gain a comprehensive understanding of membrane degradation processes, the utility of disinfection approaches, and RO process conditions. However, the variation in analytical methods and ageing conditions vary significantly across these studies, rendering their correlation difficult. Indeed, the experimental conditions use diverse scenarios such as active filtration conditions in a RO test rig and passive soaking conditions without applied pressure. Most importantly, the formation of chlorine dioxide was carried out in different ways so that varying amounts of additional oxidative agents such as hypochlorite or chlorite could be present (see below), which may have pronounced effects on membrane integrity. To unambiguously ascertain the potential of chlorine dioxide as disinfectant and its role in membrane degradation, the present study focuses on the investigation of the production processes of ClO_2 and the associated byproducts, as well as the damaging effects. To this end, a combination of targeted experiments that dissect the chemical matrix of ClO_2 formation were carried out with the aim to achieve a better understanding of the membrane degradation processes and underlying reactions.

Generally, membrane damage and the deterioration of its performance is often initiated by chemical changes to the aramid layer, which is thought to lower the resistance to mechanical stresses and may even lead to a delamination from the supporting polyether sul-fone (PES) layer [A13,A16,A22]. To the best of our knowledge, previous studies focused on investigating changes to the mechanical properties of aramid upon exposure to free chlorine. Changes in the stress-strain curves of aramid fibers were analyzed after soaking in different concentrations of free chlorine [A13], and changes in the ductility and stiffness of thin aramid films at the air-water interface were explored using pendant drop mechanical analysis [A16]. However, these studies were conducted under conditions that differ significantly to the typical conditions of RO processes, rendering a direct relation of these results such processes difficult. Also, the insights from such studies of mechanical properties have so far not been correlated with experiments using offline spectroscopic techniques that would allow to quantify the chemical changes to the aramid layer. As outlined in the following overview, flanking analytical techniques for investigating membrane integrity can be differentiated in (1) high-end laboratory-based methods and (2) more practical approaches to characterize process performance *in-situ*. In both cases, compelling insight can be expected if they are used in combination with a targeted experimental design of process conditions.

1. High-End Laboratory Methods

In order to investigate oxidative changes in the aramid layer, attenuated total reflection (ATR) Fourier-transform infrared (FTIR) spectroscopy has been frequently used [C16,C18,C22]. To the best of our knowledge, however, there is only one publication that correlated peak ratios from ATR-FTIR measure-

ments with the Fujiwara test to quantify chemical changes to the membrane [C22]. Alternatively, visible defects in the aramid layer have been analyzed by means of scanning electron microscopy (SEM) [C7,C25,C26]. Here, a prominent current research gap is the reliable differentiation of artefacts such as scratches on the membranes' surfaces from damage that impacts transport properties. Surface-sensitive X-Ray photoelectron spectroscopy (XPS), finally, reveals a comprehension on changes in chemical composition and functionalization of the membrane [C27,C28].

2. *In-situ* Analytical Approaches

To classify the performance of RO membranes in processes, traditional measurements of salt rejection rates or membrane permeability are commonly used [C22,C23,C25]. However, these process parameters have the drawback that they only change after the membrane has been severely damaged. Hence, these methods fail to identify the onset of chemical changes as the primary cause for a subsequent macroscopic failure of the membrane. Another method to assess membrane damage is the so called methylene blue (MB) dye test [C12]. This test allows to directly visualize the transport of the MB dye in the form of blue taches on the permeate side of RO membranes, which indicates locations of diminished membrane performance. So far, however, testing with the MB dye has only been utilized for a qualitative understanding of membrane integrity [C29,C30]. To the best of our knowledge there is so far no opportunity to use this test in a quantitative way to elucidate the extent of damage and the relation of the latter to the different treatment conditions. To provide an improved analysis of the effects of the chlorine dioxide matrices on RO membranes, the present study uses ATR-FTIR to quantify chemical changes in combination with a refined MB dye test with complementary SEM and XPS measurements that provide localized microscopic and spectroscopic insights.

To gain broad insights through our thorough analytical characterization of ClO_2 -induced membrane damage, we pursued a carefully designed experimental approach. In particular, our approach extends beyond considering chlorine dioxide, but aims to include other potential chemical oxidants commonly observed in a ClO_2 matrix. With this approach we aim to address the variability in chlorine dioxide production methods and acknowledge that commercially available ClO_2 products often contain by-products of the manufacturing process such as free chlorine (hypochlorite/hypochlorous acid), chlorite, or persulfate. Indeed, the concentrations of added precursors or byproducts strongly depends on the ClO_2 generation method [C31]. Whereas the hydrochloric acid-chlorite or the chlorine-chlorite process (see Scheme 3.23A) use free chlorine as reactant to generate ClO_2 [C31,C32], the persulfate-chlorite process is responsible for a comparatively lower free chlorine content (see Scheme 3.23B), but leads to an excess of persulfate, which remains in the disinfectant solution [C31,C32]. Finally, the acid-chlorite processes leads to an acidic disinfectant solution, which has an overall higher oxidative capacity (see Scheme 3.23C) [C24].

In all processes, factors such as temperature, pH, and the concentration of the precursors are expected to be highly relevant for the concentration of possible membrane-damaging oxidative byproducts. For example, the reported concentrations of possible byproducts as molar ratios compared to the concentration of chlorine dioxide were 100-200 % for persulfate, 50-70 % for chlorite, and 0-23 % for free chlorine [C33–C35].

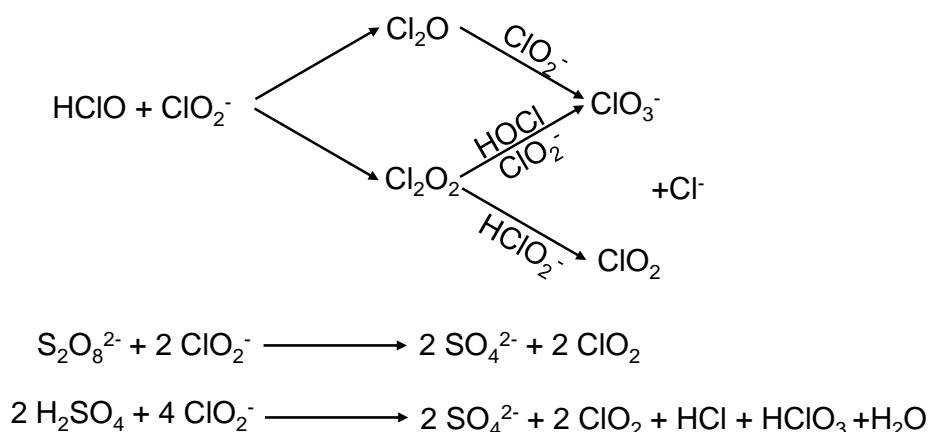


Figure 3.23: Reaction schemes describing three important manufacturing processes to produce chlorine dioxide. A: Chlorine-chlorite process, B: Persulfate-chlorite process, C: Acid-chlorite process.

Considering these factors, the present study aims to elucidate the effects of the chlorine dioxide matrix on RO membranes. For a careful characterization of membrane damage, we report a comprehensive study that combines insights from different analytical techniques [C24,C31], targeting to advance the analysis towards gaining quantitative insights. Additionally, we examine the influence of various intermediate by-products from the chlorine dioxide production process by specifically targeting the damage by each component separately.

3.3.3 Materials and Methods

Commercially available DOW XLE membranes were used in this study. The membranes were cutted from Grünbeck GbR 4-84 spiral wound modules. All experiments were conducted at a controlled temperature of 21 °C. Accelerated degradation experiments were performed with solutions of sodium hypochlorite (NaClO), chlorine dioxide (ClO₂), sodium persulfate (Na₂S₂O₈), sodium chlorite (NaClO₂), sodium chloride (NaCl), sodium sulfate (NaSO₄), and sodium chlorate (NaClO₃), which were chosen to represent the possible components of a ClO₂ matrix. For the special case of free chlorine, we adjusted the pH value of hydrochloric acid solutions by using sodium hydroxide to form the different species of free chlorine; if the pH value of the solution was below the pK_a value (7.53), hydrochloric acid is the predominant species, while hypochlorite is the predominant species at higher pH values [C15].

The solution of ClO_2 was prepared by reaction of $\text{Na}_2\text{S}_2\text{O}_8$ and NaClO_2 at neutral pH. The aqueous ClO_2 solution was purified using gas stripping followed by redilution in desalinated water to concentrations of 3 g L^{-1} by the Dr. Kücke GmbH. The investigation of membrane damage was performed in two different experimental setups: (i) membrane soaking experiments and (ii) active filtration conditions in an RO plant. The membrane soaking experiments were designed to simulate long-term exposure, whereas the active filtration conditions represent the operational environment of an RO system. This dual approach allowed us to comprehensively assess the impact of the various oxidative chemicals under both controlled and practical conditions.

Membrane soaking experiments

Membrane soaking experiments were performed using $8 \times 8 \text{ cm}^2$ RO membrane sheets. The sheets were immersed in aqueous solutions in 50 mL Falcon tubes containing the components found in commercially used ClO_2 disinfectant solutions. The soaking experiments were carried out over the course of seven days. At specific time intervals (days 1, 2, 3, and 7), the anions of the solutions

were analyzed by photometric methods and by ion-chromatography to monitor changes in chemical composition. Before and after the soaking process, membranes were rinsed using desalinated water. The concentrations were intentionally chosen to exceed typical disinfectant concentrations to ensure that damage can indeed be observed if individual components have the potential to affect the membrane, thereby offering insight into the impact on membrane integrity under controlled conditions.

In-situ analysis of RO membranes at varying active filtration conditions

Membrane damage under active filtration conditions was studied with pure ClO_2 solutions. For this purpose, membranes were installed in an RO pilot plant designed to minimize the catalytic effects of iron ions on membrane damaging reactions, as comprehensively described elsewhere [C6,C36]. To achieve this, the use of steels and iron-containing alloys in the pilot plant was avoided, instead opting for a construction from titanium and polyvinyl chloride (PVC) components. For all experiments under active filtration conditions, an aqueous ClO_2 solution with a concentration of 1 gram/L was used. During the experiments, the transmembrane pressure (*TMP*) and the Reynolds number (*Re*) were varied to investigate the effect of the filtration conditions on the membrane damage. The Reynolds number was calculated by the cross-flow velocity v , the characteristic flow diameter d_f and the viscosity ρ of pure water at $21 \text{ }^\circ\text{C}$. The cross-flow velocity in bulk was calculated according to equation 3.5 using the feed channel width ($w = 4 \text{ cm}$) and height ($h = 8 \text{ cm}$), the feed spacer porosity ($\epsilon = 0.89$), and the flow rate Q [C10].

$$v = \frac{Q}{w \cdot h \cdot \epsilon} \quad (3.5)$$

The characteristic flow diameter (d_f) was calculated according to Crittenden *et al.*[C8]:

$$d_f = \frac{4 \cdot w \cdot h}{2 \cdot w + 2 \cdot h} \quad (3.6)$$

Before the membrane was exposed to the ClO₂ solution the membrane was compacted for at least 24 h at experimental conditions with desalinated water. Hence, the cross-flow velocity, as well as the TMP, were the same as during the ClO₂ exposure. The ClO₂ solution was pumped into the membrane flat cell during the filtration. The retentate and permeate were recycled in the feed vessel. The membrane properties were measured continuously by flow, pressure, conductivity, and pH sensors. The data was recorded in one second time intervals by a Siemens S7 SPS. The complete RO installation is comprehensively described elsewhere [C6,C36].

ATR-FTIR spectroscopy

ATR-FTIR spectroscopy was conducted using a Cary 670 FTIR Spectrometer (Agilent Technologies, Santa Clara/USA) equipped with a germanium crystal. Each membrane sample was analyzed at three different spots to ensure comprehensive coverage and to account for potential variability.

We calculated the absorbance ratios for all peaks corresponding to the aramid layer (peaks 2–4, see SI), using the peak at 1153 cm⁻¹, that corresponds to the SO₂ stretching vibrations, as an intensity reference to avoid any influence from aromatic vibrations of the aramid layer. The degradation index (DI) of the aramid peaks (peaks 1–4) was then calculated by dividing the ratios of the corresponding peak heights $P(i)$ ($i = 2-4$) from the membrane sample (P_s) to those of the pristine membrane (P_p).

$$DI = \frac{P_s(i)/P_s(SO_2)}{P_p(i)/P_p(SO_2)} \quad (3.7)$$

This approach of calculating individual group changes in the aramid layer was expected to provide a more mechanistic understanding of membrane degradation under various disinfection conditions.

Methyleneblue dye test

In the present study, the MB dye test, traditionally used for a binary determination of membrane damage, was combined with image analytical methods to allow for a quantitative assessment of membrane integrity. For this purpose, membrane samples were cut into a circular shape with a radius of ca. 7.5 cm and installed in a filtration cell. After filtering a methylene blue dye solution, the permeate side of the membrane samples were photographed. Dyed membrane areas were identified by optical imaging and the ratio of these dyed areas to the total membrane surface

was defined as the methylene blue ratio (MBR) (see SI for details). A higher MBR indicates a lower retention capacity for the MB dye, signifying greater membrane damage.

3.3.4 Results and Discussion

The following discussion of the results of the present study is structured into three parts: (1) an evaluation of the quantitative MB dye test by comparison to salt passage and SEM imaging, (2) an assessment of the membrane damaging effects of the different potential components of a chlorine dioxide matrix flanked by our comprehensive analytical approach, and (3) a discussion of the exploratory investigations of the impact of varying RO process parameters on membrane integrity during disinfection.

Quantitative methylene blue dye test based on optical imaging

To validate the quantitative MB dye test, the methylene blue ratio (MBR) as a measure for the extent of coloration (see Methods section for details) was correlated with the salt passage (SP). To this end, soaking experiments were carried out with membrane samples that were immersed in solutions containing different amounts of a commercially available ClO₂ disinfectant solution (see Methods section for details). Selected membrane samples were subsequently examined for their salt rejection with an aqueous sodium chloride solution ($c = 2 \text{ g L}^{-1}$) and for the retention of the MB dye (Figure 3.24). The filtration cell used for the MB dye tests was used throughout and the relative salt passage through the membranes was determined as described by Karabelas et al. by taking concentration polarization effects into consideration [C37,C38].

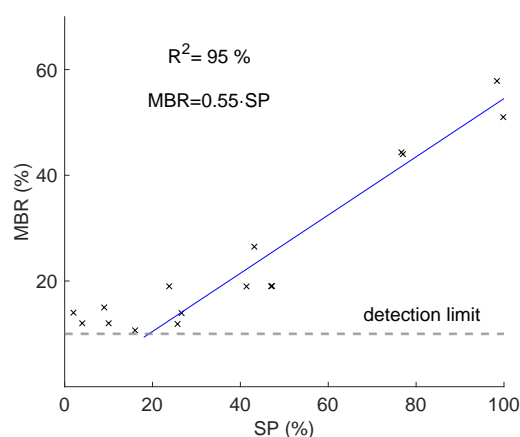


Figure 3.24: Validation of the image analytical quantification of the methylene blue dye test. The plot shows the relationship between the salt passage (SP) and the methylene blue ratio (MBR) as determined by the conductivities of the feed, retentate, and permeate, respectively. The observed linear relation ($R^2 = 95$) serves to validate the image analytical method.

Higher MBR and SP indicate a diminished retention capacity, which in turn indicates increased membrane damage. A plot correlating the determined MBR and SP values as shown in Figure 3.24 reveals a linear correlation above MBR values of ca. 10 %, which validates the method of determining MBR as a direct measure of the quality of the membrane above this threshold. The MBR, hence, enables reliable and quantitative assessment of membrane damage from a technical perspective. For membranes that display SP below ca. 20 %, the MBR remains constant around 12 %. This lack of differentiation at low SP values could possibly arise from the challenge of an accurate background detection.

To further characterize the damage detected in the MB dye test, sections of the membrane samples were additionally imaged by means of SEM (Figure 3.25). To reconstruct large membrane sections, SEM images were recorded with a 20 % overlap and stitched together (see SI for details) [C6]. Figure 3.25 shows a series of images from a damaged and dyed RO membrane, progressing from photographs to optical microscopy images, and finally to SEM images. The optical microscopy image reveals a blue perforation spot, which corresponds to several defects as visually discernible in the SEM image of the same membrane (Figure 3.25). The morphology of the membrane surface seems to have a lower topography at several locations than the intact area of the membrane. The features shown in Figure 3.25 are representative for images of other membrane samples that were exposed to the chlorine dioxide disinfectant and analyzed by means of both the MB dye test and SEM imaging.

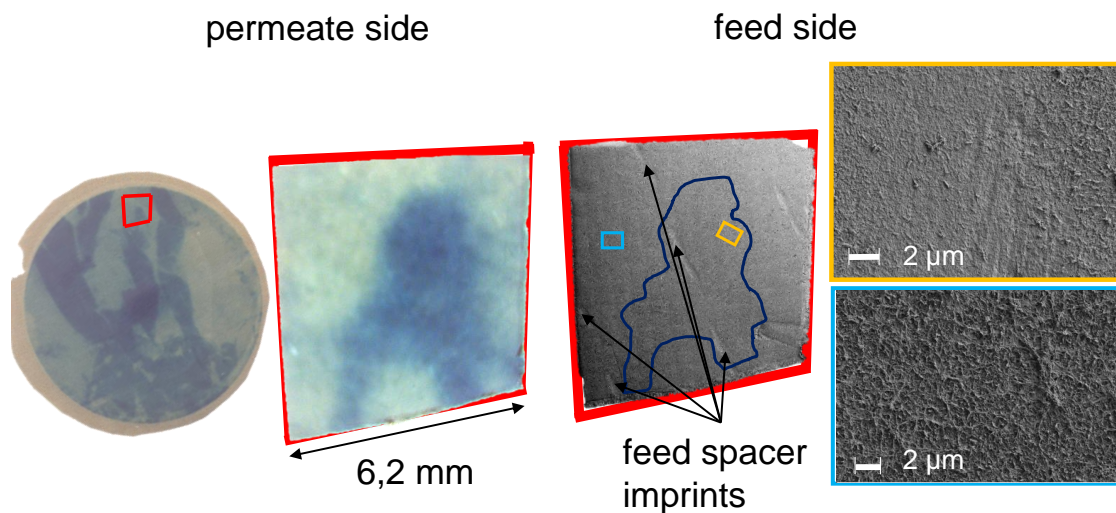


Figure 3.25: Sequential analysis of a damaged membrane using the methylene blue (MB) dye test as well as imaging by scanning electron microscopy (SEM). From left to right: photograph of a membrane after the MB dye test and SEM images of the same section of the membrane showing the physical damage to the membrane surface in greater detail. The images demonstrate the correlation between the visible damage in the MB test (dark blue surrounded area) and the microscale structural damage.

Interestingly, imprints from the feed spacers are distinctly visible in the SEM micrographs of samples with low and high SP. Apparently, these surface defects or

artefacts do not impact the membrane's retention properties. This interpretation is corroborated by a comparison with the photographs recorded after the MB dye test that shows that these imprints do not coincide with dyed sections of the membrane (Figure 3.25). Indeed, the results of the MB dye test suggest that, in the case of the membrane shown in Figure 3.25, shallow surface scratches have no effect on MB rejection or SP. Hence, the MB breakthroughs can be directly linked to damages observable in SEM images, providing a comprehensive understanding of the nature and extent of membrane damage.

Dissecting the damaging potential of different components of the chlorine dioxide matrix

Soaking experiments were designed to assess the damaging effects of components typically found in commercially available chlorine dioxide disinfectant solutions on RO membrane integrity. To assess the membrane damage, we employed a combination of the MB dye test, SEM imaging, ATR-FTIR spectroscopy, and XPS.

To determine the specific components of the chlorine dioxide matrix that compromise membrane integrity, we employed the newly established quantitative MB dye test. To this end, soaking experiments were performed with the different chemical components of the chlorine dioxide matrix (see Methods section for details). Figure 3.26 provides an overview of the results of the MBR determined for these soaking experiments.

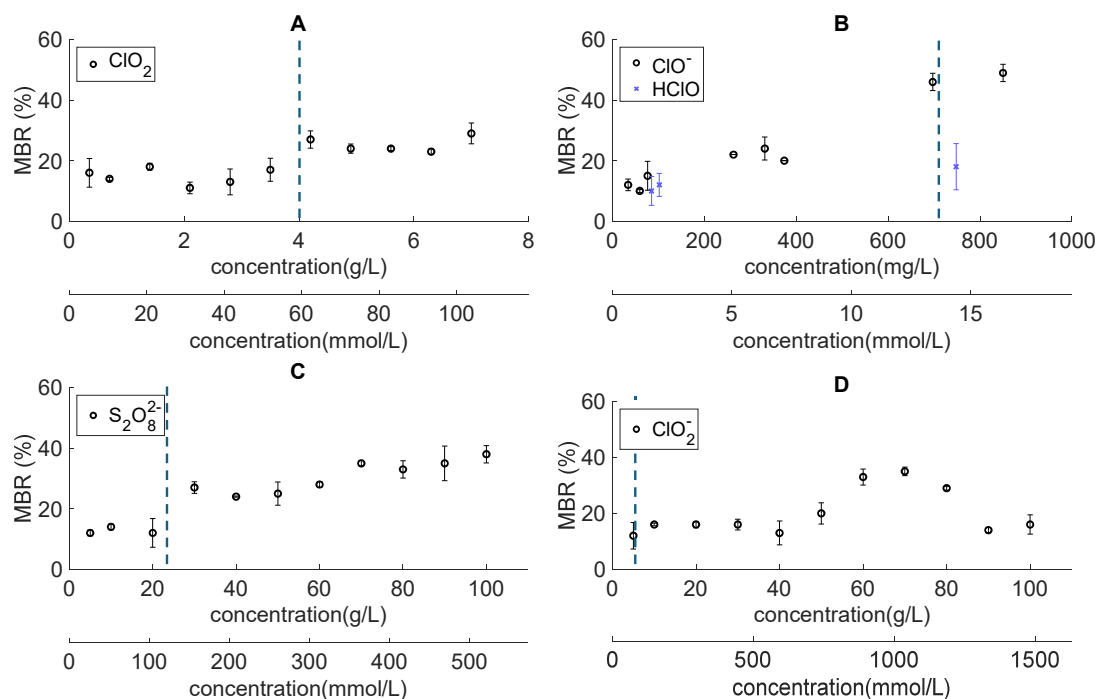


Figure 3.26: Plots of the methylene blue ratio (MBR) determined for DOW XLE membranes soaked in aqueous solutions of different individual components of the chlorine dioxide matrix. Shown are plots of the MBR against (A) the concentration of chlorine dioxide, (B) hypochlorite and hypochlorous acid, (C) persulfate, and (D) chlorite ions. Each data point represents the mean values and the 90 % confidence intervals. The vertical dashed lines mark a worst-case scenario for the case that free chlorine, persulfate or chlorite are present as by-products in a commercial ClO_2 formulation. Such a scenario could be constructed for the case of a chlorine dioxide solution of 60 mmol L^{-1} .

Observations of the MBR against the explored concentration range (0 to 100 g L^{-1}) for experiments with sulfate, chloride, and chlorate ions do not show a significant variation, suggesting that these ions do not affect membrane integrity (see SI). By contrast, the MBR increased with exposure to increasing concentrations of chlorine dioxide (ClO_2) (0 to 7 g L^{-1}), free chlorine (OCl^- , HOCl) (0 to 16 mmol L^{-1}), persulfate ions ($\text{S}_2\text{O}_8^{2-}$) (0 to 520 mmol L^{-1}), and chlorite ions (ClO_2^-) (0 to 1480 mmol L^{-1}). It therefore appears evident that these compounds induce membrane damage and lead to a diminished rejection capacity. However, the threshold concentrations at which membrane damage can be detected varies greatly. In the case of free chlorine, damage to the membrane samples is observable at very low concentrations of ca. $5\text{--}14 \text{ mmol L}^{-1}$ (Figure 3.26b), with the pH value of the solution significantly influencing the extent of damage. These pH-dependent effects on membrane integrity are well described in the literature, varying with the presence of reactive species present at low pH values, i.e., hypochlorous acid that triggers a chlorination of the aramid's aromatic ring [C13,C20,C21]. Instead of chlorinating the aromatic rings, the presence of hypochlorite at higher pH values is believed to predominantly lead to a hydrolysis of the amide bond [C39,C40]. Compared to the manufacturer's specifications, which assume a maximum chlorine exposure of 1000 ppmh, we exceeded this

by a factor of 43, even at the low concentrations of 5 mmol L^{-1} and exposure time of one week [C41]. The degradation of the membrane at these high concentrations is plausible according to the manufacturer's specifications.

For chlorine dioxide, the concentration at which membrane damage becomes apparent is ca. 50 mmol L^{-1} , while the concentration increases to 150 mmol L^{-1} for persulfate ions (Figure 3.26c) and to ca. 750 mmol L^{-1} for chlorite (Figure 3.26d). Chlorite ions appear to damage the membrane with increasing concentrations up to a concentration of ca. 1.2 mmol L^{-1} (Figure 3.26c). Surprisingly, at even higher chlorite concentrations, the determined MBR values return to levels akin to those for pristine membranes, hinting at complex chemical interactions with the membrane material. With regard to the results of the MB-test and the possible reactions, the presence of free chlorine in a commercial chlorine dioxide solution could significantly affect membrane degradation, which may inadvertently be attributed to ClO_2 if the coexistence of free chlorine is not taken into account.

Chemical analysis via ATR-FTIR

To elucidate the chemical changes to the membrane, we subjected membrane samples to ATR-FTIR spectroscopy. Shown in Figure 3.27 are representative ATR-FTIR spectra that were recorded before and after exposure to a chlorine dioxide solution ($c = 102 \text{ mmol L}^{-1}$) over the course of 7 days. The spectra recorded after exposure show decreasing intensities of the characteristic bands associated with the aromatic polyamide (aramid) layer of the membrane, particularly for the amide I (carbonyl bond), the H-bonded carbonyl, and the amide II (N-H bond) vibrational modes (Figure 3.27A). By contrast, the intensity of the bands associated with the polysulfone layer barely change. To quantify the changes induced by the different chemical components of the chlorine dioxide matrix, multiple IR spectra were recorded for each membrane sample after exposure and a detailed analysis was carried out to explore how the aramid layer changes (see Methods section for details).

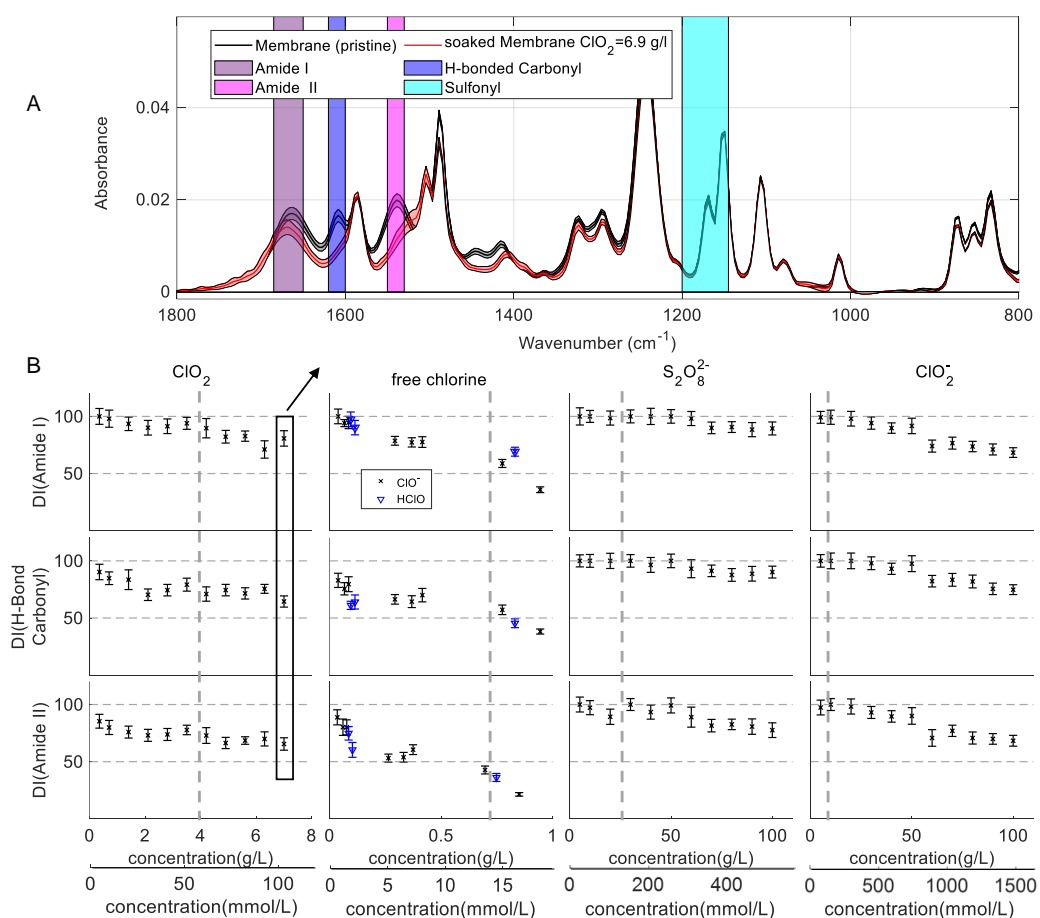


Figure 3.27: (A) FTIR spectra of membranes soaked in $6.9 \text{ g L}^{-1} \text{ ClO}_2$ ($c = 102 \text{ mmol L}^{-1}$; red spectrum) and in deionized water for 1 week (black spectrum). The thick lines mark the mean spectrum of the triplicate. The 90% confidence interval is displayed by the less color-intense area around the mean spectrum. (B) Degradation indices, DI, (see equation 3.7) of three important groups of the FTIR spectrum of the aramid. Shown are DI values of membranes samples soaked in purified chlorine dioxide, free chlorine, persulfate, and chlorite. In analogy to Figure 3.26, the vertical dashed lines mark a worst-case scenario for the byproducts free chlorine, persulfate and chlorite in a chlorine dioxide solution of 60 mmol L^{-1} .

To account for variations in band intensities for different samples and variable measuring conditions, the intensities of analyzed IR bands were normalized relative to the intensity of the band at 1153 cm^{-1} characteristic of the unaffected polysulfone layer. The normalized band intensities of amide I (carbonyl bond), H-bonded carbonyl, and the amide II (N-H bond) bands were then compared to the intensities of the same bands in pristine samples (see equation 3.7). The IR band intensity ratios of the exposed and pristine membrane samples were used to define a degradation index (DI) that was used herein to assess the effects of the different chemical compounds on the aramid layer.

Plots of the DI against the concentration of the different components of the chlorine dioxide matrix show decreasing values after exposure to increased concentrations of chlorine dioxide, free chlorine, persulfate, and chlorite (Figure 3.27B), suggesting

pronounced chemical changes. However, the concentration at which these changes are detectable depend on the type of ion/molecule and the respective chemical functional group of the aramid layer.

Corroborating the preceding analyses by the MB test, free chlorine changes the DI at the lowest relative concentrations. The determined onset concentration for changes to the DI is 1.2 mmol L^{-1} . Whether predominantly hypochlorite or hypochlorite acid is present – as controlled by the pH value of the aqueous solutions – appears to not play a significant role for the degradation of the aramid layer, since the DI values follow a similar progression for samples that were exposed to solutions with higher and lower pH values. These results contradict the observations from the MB test, which may be explained by changes to the surface chemistry that do not similarly affect transport properties. These findings may show-case the importance of correlating chemical analyses with retention tests.

The changes for the DI after exposure of membrane samples to the other oxidants occur in the same concentration range as previously determined by means of the MB test with an onset for chlorine dioxide at ca. 5.2 mmol L^{-1} , for persulfate at ca. 300 mmol L^{-1} , and for chlorite at ca. 600 mmol L^{-1} .

If the concentrations and the changes in the DI values in the present experimental series are compared with the concentrations in a complex chlorine dioxide matrix, it can be concluded that the presence of chlorite should not have a significant effect on the membrane integrity and the same is true for persulfate. With regard to the reaction pathway of commercially *in-situ* formed chlorine dioxide, these two species (chlorite and persulfate) can additionally be considered to not play a significant role in the membrane degradation process, as they are both part of the reactant mixture, and their concentration decreases during chlorine dioxide formation.

The experimental data suggest that free chlorine is the most critical species in the chlorine dioxide matrix concerning membrane integrity. The experiments indicate that a similar membrane damage would only occur with purified chlorine dioxide at a fivefold higher absolute concentration. Considering that commercial chlorine dioxide solutions may contain up to 20% of free chlorine is consistent with the typically observed issues of membrane degradation with such disinfectant solutions [C31,C32,C42].

The whole data set for all oxidants suggest that the amide II group is most significantly affected by exposure to the chlorine dioxide components. The DI determined for the H-bonded carbonyl and the amide I functional group display similar trends, albeit less pronounced compared to the amide II signals. The correlations between the bonds are displayed in Figure 3.28.

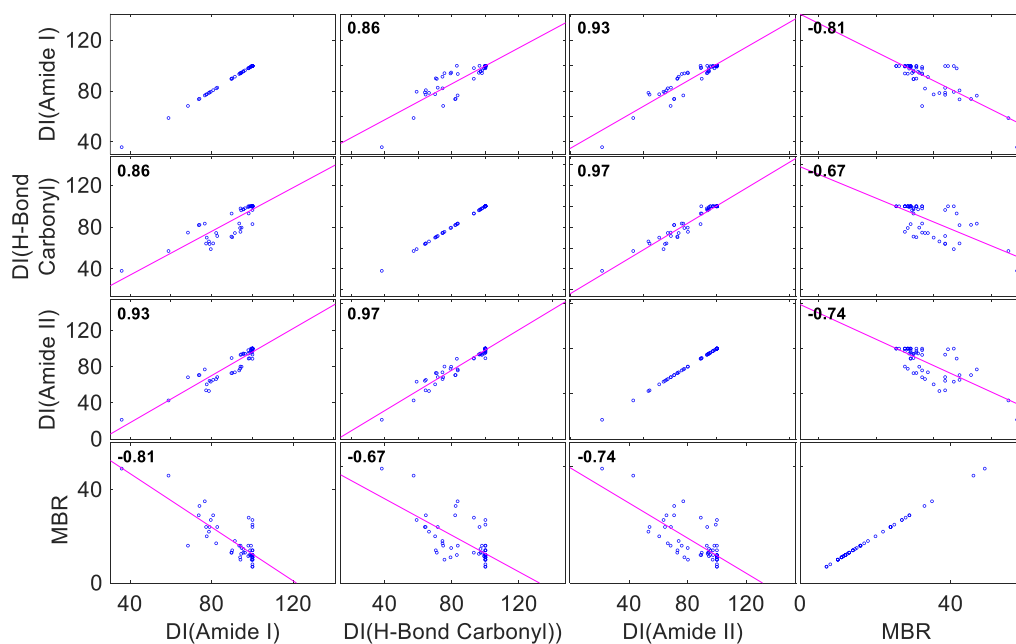


Figure 3.28: Correlation matrix of the DI indexes and the corresponding MBR values. The Pearson correlation coefficients were calculated. The diagonal plots show the histograms of the DI and MBR values, indicating that the major part of the membranes is not severely damaged.

The DI correlate most strongly between amide I - H-bond carbonyl (86%), amide I-amide II (93%) and amid II-H-bond carbonyl (97%). This observation could be explained by the fact that the H-bonds strongly depend on the integrity of the primary structure of the polymer and the integrity of the amide bond. The strongest correlation between the DI and the MBR values was observed in the case of amide II (81% reduction). The negative correlation coefficient illustrates the different behavior of the DI and MBR values. Lower DI values indicate larger chemical changes to the aramid layer, whereas higher MBR values indicates more substantial damages to the membrane.

To study changes in the composition and chemical environment of the surface of the aramid layer in more detail, membrane samples were subjected to further analyses by means of XPS measurements. To this end, membrane samples were soaked in solutions of chlorine dioxide (102 mmol L^{-1}), persulfate (521 mmol L^{-1}), chlorite (1483 mmol L^{-1}) or hypochlorous acid (14 mmol L^{-1}), respectively. Figure 3.29 compiles an XPS survey spectrum of the pristine membrane and detailed spectra of the C 1s, Cl 2p, and S 2p core levels after exposure of samples to the different aqueous solutions.

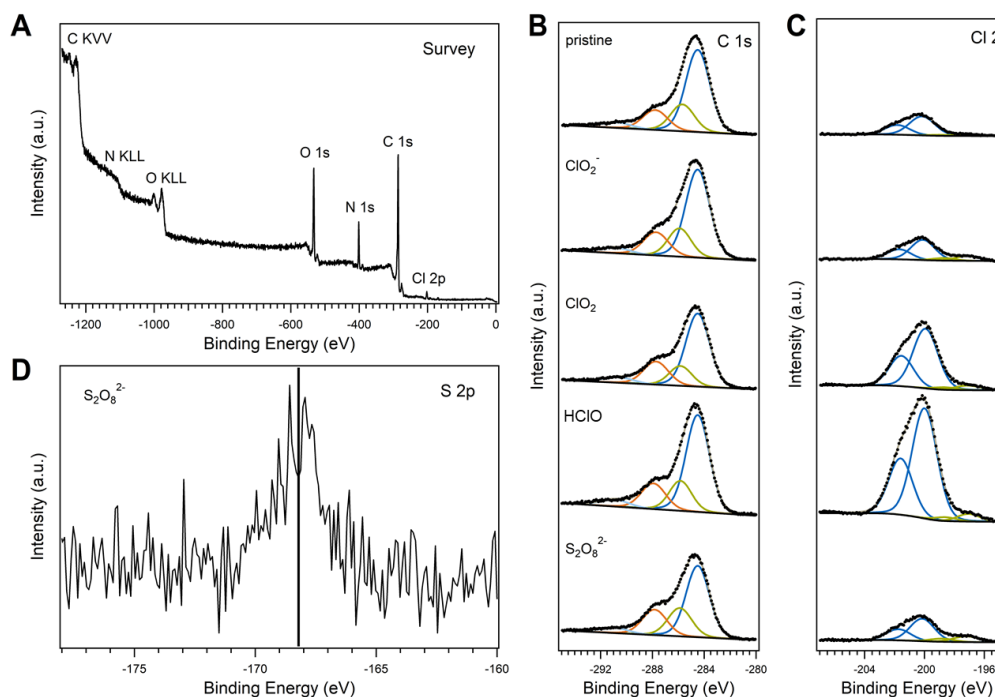


Figure 3.29: XPS analysis of RO membranes: pristine and soaked in 1483 mmol L^{-1} chlorite, 102 mmol L^{-1} chlorine dioxide, 14 mmol L^{-1} hypochlorous acid, and 521 mmol L^{-1} persulfate. (A) Survey spectrum of a pristine membrane with assigned core level and Auger transitions. (B) C 1s core level and (C) Cl 2p core level of the different membranes. (D) S 2p peak only observed at a membrane soaked in persulfate. The intensity of all spectra is scaled to the total N 1s peak intensity.

Whereas the C 1s core level does not show any significant changes across the investigated membrane samples, remarkable intensity variations in the Cl 2p core level are observed. It needs to be noted that chlorine species are present in all membranes, even when no chlorine disinfectant was applied. The less intense photoemission from chlorine in the pristine membrane and the membranes after soaking in chlorite or persulfate solution might originate from the production of the aramid layer where aromatic acyl chlorides and *m*-phenylenediamine are typically used as monomers [C43]. The extent of cross-linking of the polymer through introduction of trifunctional acyl chlorides as co-monomers is not known to us, since this information was considered proprietary by the membrane manufacturer.

Besides the minor chlorine contaminant, the membranes soaked in hypochlorous acid and chlorine dioxide show a distinct chlorine photoemission which is 5 and 3.5 times enhanced compared to the pristine membrane samples. As all soluble species are removed when rinsing the membranes in water after soaking in the disinfectant solutions, the detected increased chlorine is presumably chemically bound to the polymer layer. This finding supports the results from the MB test in which the hypochlorous acid may stabilized the rejection of membrane that could be induced by the chlorination of the polymer and the subsequent tightening effects. Finally, membrane samples that were soaked in persulfate reveals an S 2p core level peak at a binding energy characteristic for sulfate groups, suggesting the incorporation of

sulfur in the polymer.

The presented spectroscopic data therefore allow for a tentative discussion of possible reaction pathways of pure chlorine dioxide and the aramid layer. Alayemięka *et al.* proposed a radical oxidation reaction involving the N–H bond that involves a hydrogen abstraction, which could be enhanced by the higher oxidation potential of chlorine dioxide at low pH values [C24]. Our investigations corroborate this pathway, since we observe changes to the intensity of the amide II vibrational band and the hydrogen-bonding vibrations at low concentrations that were correlated with changes in the MBR values. Our XPS analysis adds complementary information since the higher chlorine peak intensities point at a reaction of the chlorine dioxide that leads to an accumulation of chlorine atoms in the polymer layer. Considering the changes in transport properties and MBR values of membranes immersed in solutions with free chlorine, our findings may be considered in the context of previous reports. In references [C20,C21] hypochlorous acid has been suggested to chlorinate the aramid’s aromatic rings directly or via an Orton rearrangement [C13,C21], causing a reduced mechanical stability of the aramid layer [C13]. Similar observations were reported by Soice *et al.* when using pendant drop analysis [C16]. A resultant lower crystallinity and mechanical stress resistance can cause a tightening effect on the membrane if a transmembrane pressure is applied. The reduced mechanical stability may be caused by the incooperation of chlorine in the aramid layer, which could destabilize the hydrogen bonding interactions between the polymer chains [C44]. Besides chlorinating the aromatic rings, hypochlorite can hydrolyze the amide bond [C15,C39,C45], which may lead to a detachment of the aramid layer from the polyether sulfone support [C39,C40]. Our observations corroborate such pathways, since decreasing intensities of the amide II and amine bond vibrations are observed as well as an increasing chlorine peak intensity in the XPS measurements.

In the case of chlorite ions, we observe a significant degradation of the membrane’s aramid layer using the MB test, whereby the values decrease at very high concentrations to a level comparable to untreated membranes. However, no differences could be detected in the XPS measurements, which indicates that no additional chlorine is bound in the aramid layer. A reaction comparable to that proposed for hypochlorous acid, which could explain the relatively low MBR values at very high concentrations is therefore unlikely.

The IR bands associated with the amine and amide II group show pronounced changes upon exposure to the components of the chlorine dioxide matrix and appear to strongly correlate with a degradation of the RO-membrane (see Figure 3.28). The herein defined DI indices allow for a comparative study of the changes of the aramid layer and its chemical functional groups, which appears to be a significant first indicator for chlorination. Previously proposed chlorination pathways [C46] were supported by the XPS analysis of the membrane surface. Furthermore, the same damage trend can be observed across all tests with regard to the concentrations of the soaking experiments. According to combined evidence from (i) the ATR-FTIR investigations, (ii) the MB test, (iii) the correlating salt retention and (iv) the XPS measurements, the harmfulness of chemical constituents in the chlorine

dioxide matrix can be ranked as: chlorite ; persulfate ions ; purified chlorine dioxide ; free chlorine. In comparison, chlorate, chloride, and sulfate did not impact RO membrane integrity.

The comparison and the reactivity ranking of the components of the chlorine dioxide matrix are based on the expected concentrations for an *in-situ* formed chlorine dioxide solution (see vertical dashed lines in Figures 3.26 and 3.26). In the provided order, we observed increasing changes in the calculated DI values from the ATR-FTIR measurements, higher MBR values from the MB test, which display a loss in membrane rejection capacity, and more extensive changes in the XP spectra. Regarding the likely reaction pathways, we conclude that the oxidation by chlorine (i.e. hypochlorous acid) through an electrophilic attack seems to be the most favourable of all oxidants. At the same time we want to point out that more research is needed for an in-depth investigation of the underlying driving forces.

All the species are oxidizing agents, and they could as such react either by oxygen transfer reactions or single electron transfer. Interestingly, the reactivity trends do not appear to follow the standard redox potentials of the individual reactive species, which are 0.76 V for chlorite, 0.954 V for chlorine dioxide (depending on the pH value) [C24], 1.16 V for free chlorine (depending on the pH value) [C47] and 2.4 V sulfate radicals, which can form from persulfate [C48]. Hence, the observed trends must be attributed to specific reaction mechanisms. The free chlorine, especially at low pH values, may add to the polymer chain by an electrophilic attack [C15]. Through elimination of OH⁻ an equivalent of Cl⁺ could form, which may attack either the amide nitrogen or the aromatic ring [C15,C46]. With respect to pathways that could explain an incorporation of sulfur during persulfate soaking experiments (see XPS data above), the cleavage of persulfate into two sulfate radicals could be the relevant initiation reaction. This reaction can be accelerated at low pH values, higher temperatures, or by UV irradiation [C48]. The observation that – despite the high redox potential of sulfate radicals – only moderate membrane damage was caused can be rationalized by the fact that no aliphatic bonds are present in the aramide structure so that sulfate radicals would have to react with N-H bonds or the aromatic ring, which is less favorable. Chlorite may behave as a nucleophile that could add to the C=O bond of the aramide before oxygen or a reaction could occur after an electron transfer takes place [C49]. Understanding the degradation interactions is, key to designing effective disinfection processes.

Based on the insights, we aimed to explore the effects of chlorine dioxide disinfectant solutions without free chlorine under RO process conditions. To this end, we used a *ex-situ* stable chlorine dioxide solution that was prepared by gas stripping and reportedly avoids free chlorine at neutral pH (see Methods for details). We took advantage of the opportunity of utilizing this benign formulation of purified ClO₂ disinfectant and targeted the actual RO process parameters (=mechanical stress) to investigate which process conditions affect the damaging effects to the membrane. To this end, we chose a neutral pH value to prevent higher oxidative potentials, which could further compromise the integrity of the membrane [C24].

Effects of cross-flow conditions on membrane integrity

To explore the impact of active filtration conditions, we conducted experiments using a purified chlorine dioxide solution (1 g L^{-1}) in a 2^k full factorial design of experiments (DoE) where the Reynolds number, representing cross-flow velocity, and the transmembrane pressure (TMP) were varied as key parameters. The chlorine dioxide concentration employed in these experiments was deliberately chosen about 5000 times higher than typical disinfection levels to ensure accelerated damaging effects. No relevant concentration of by-products could be measured by ion-chromatography and UV-Vis spectroscopy over a measurement period of 7 days. The experiments were repeated twice to ensure reliability. Figure 3.30 illustrates the effect of varying Reynolds numbers and TMP on the salt passage over time.

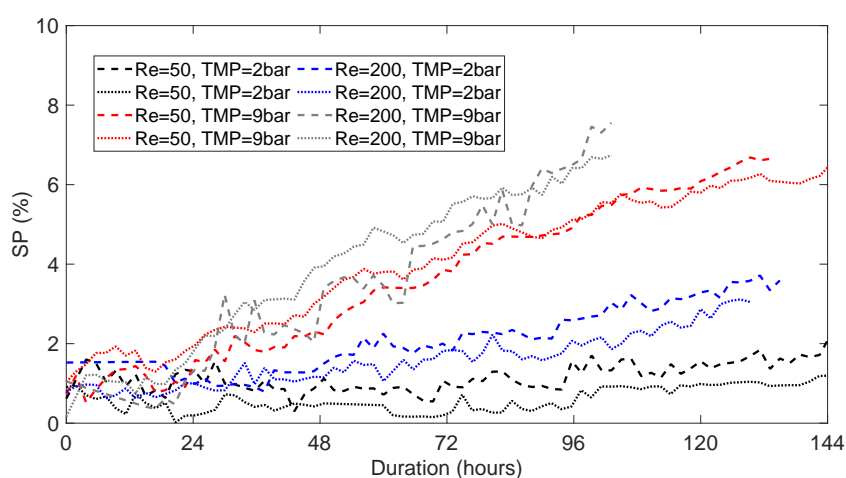


Figure 3.30: Evolution of the salt passage (SP) as determined during accelerated damaging experiments with the membrane and a purified chlorine dioxide solution (1 g L^{-1}).

For all variations of the TMP and Reynolds numbers an increasing salt passage over time could be observed. At a TMP of 2 bar, despite the high chlorine dioxide concentration, the salt passage remained largely unchanged. However, at a TMP of 9 bar, the salt passage increased sixfold over the course of the experiment, underscoring that the TMP has a pronounced effect on membrane integrity in combination with the application of chlorine dioxide. At higher Reynolds numbers, the salt passage slightly increased, reflecting the influence of the flow regime in the feed channel, but the variations were small when compared to the changes with varying TMP. The chosen variations of the Reynolds numbers are representative for spiral wound RO-modules [C8,C50].

In summary, our findings demonstrate that mechanical stress, particularly TMP, plays a substantial role for membrane damage during disinfection with purified chlorine dioxide. Notably, the effects of the TMP are more pronounced than the flow regime. These results suggest that for disinfection processes using chlorine dioxide maintaining low TMP and flow rates would be advantageous to preserve membrane integrity.

3.3.5 Conclusions

This study presents significant improvements in two integrity tests for reverse osmosis (RO) membranes: the MB dye test and FTIR spectroscopy. In the present study, these enhanced methods were applied to elucidate damage mechanisms caused by oxidative components in commercially available chlorine dioxide disinfection solutions and to examine the impact of realistic filtration conditions on membrane damage. Key findings include:

1. By combining several analytical methods a comprehensive view of RO membrane degradation could be provided. Evidence of complementary methods reinforced each other (Figure 6) and evidence of chemical changes provided by IR spectroscopy could be correlated with process-related performance losses.
2. A separate examination of the components of the chlorine dioxide matrix revealed that the components of the matrix impaired the membrane integrity in the ascending order of chlorite ; persulfate ; chlorine dioxide ; free chlorine. The way in which chlorine dioxide is generated *in-situ* is therefore crucial for the concentration of the by-products and an ensuing membrane damage.
3. If the chlorine dioxide can be used *ex-situ* in purified form, the mechanical stress on the membrane has a significant influence on the integrity of the membrane. Reducing flow rates and the TMP can mitigate negative impacts of chlorine dioxide exposure on membrane performance.

Our findings highlight that chemical changes in the aramid layer are a crucial, but not the only factor in membrane integrity loss. Remarkably, selected components of the chlorine dioxide matrix such as free chlorine showed higher damage potential than chlorine dioxide itself. The least damage was observed when a purified chlorine dioxide solution was employed at neutral pH, combined with low crossflow velocities and a low TMP. These conditions suggest that a separate disinfection process from normal RO operations, especially at low TMPs, may significantly extend the lifespan of RO membranes. This study therefore paves the way for more efficient and sustainable RO membrane disinfection processes.

Acknowledgments

We wish to thank Heribert Voit (Endress + Hauser GmbH+Co. KG) for the good cooperation and the rental of sensors to execute the experiments. Furthermore, we wish to thank Daniel Rzoska (Grünbeck GmbH) for his support in adapting the RO setup into a more corrosive resistant design.

Conflict of interests

The authors declare a financial conflict of interest, since the employees of Dr. Küke GmbH have an financial interest in their chlorine dioxide products.

Funding

The German Ministry of Economic Affairs and Climate Action (BMWK), grant number KK5022305CR0, funded this study.

3.3.6 References

- [C1] R. Baten, K. Stummeyer, How sustainable can desalination be?, *Desalination and Water Treatment* 51 (2013) 44–52.
- [C2] V.G. Gude, Desalination and water reuse to address global water scarcity, *Rev Environ Sci Biotechnol* 16 (2017) 591–609.
- [C3] T.-K. Liu, J.-A. Ye, H.-Y. Sheu, Exploring the social acceptability for the desalination plant project: Perceptions from the stakeholders, *Desalination* 532 (2022) 115757.
- [C4] P.S. Goh, W.J. Lau, M. Othman, A.F. Ismail, Membrane fouling in desalination and its mitigation strategies, *Desalination* 425 (2018) 130–155.
- [C5] P. Sperle, C. Wurzbacher, J.E. Drewes, B. Skibinski, Reducing the Impacts of Biofouling in RO Membrane Systems through In Situ Low Fluence Irradiation Employing UVC-LEDs, *Membranes* 11 (2020).
- [C6] H. Oesinghaus, D. Wanken, K. Lupp, M. Gastl, M. Elsner, K. Glas, Incipient Biofouling Detection via Fiber Optical Sensing and Image Analysis in Reverse Osmosis Processes, *Membranes* 13 (2023).
- [C7] A. Antony, A. Branch, G. Leslie, P. Le-Clech, Impact of membrane ageing on reverse osmosis performance – Implications on validation protocol, *Journal of Membrane Science* 520 (2016) 37–44.
- [C8] J.C. Crittenden, *Water treatment principles and design*, 3rd ed., John Wiley, Hoboken, N.J., 2012.
- [C9] A.J. Karabelas, M. Kostoglou, C.P. Koutsou, Modeling of spiral wound membrane desalination modules and plants – review and research priorities, *Desalination* 356 (2015) 165–186.
- [C10] G. Schock, A. Miquel, Mass transfer and pressure loss in spiral wound modules, *Desalination* 64 (1987) 339–352.
- [C11] H.-C. Flemming, G. Schaule, T. Griebe, J. Schmitt, A. Tamachkiarowa, Biofouling—the Achilles heel of membrane processes, *Desalination* 113 (1997) 215–225.
- [C12] N. García, F. Vigo, S. Chesters, M. Armstrong, Rachel L. Wilson, M. Fazel, a study of the physical and chemical damage on reverse osmosis membranes detected by autopsies, *The International Desalination Association World Congress on Desalination and Water Reuse* (2013) 1–17.
- [C13] S. Avlonitis, W.T. Hanbury, T. Hodgkiess, Chlorine degradation of aromatic polyamides, *Desalination* 85 (1992) 321–334.
- [C14] R. Sandín, E. Ferrero, C. Repollés, S. Navea, J. Bacardit, J.P. Espinós, J.J. Malfeito, Reverse osmosis membranes oxidation by hypochlorite and chlorine dioxide: spectroscopic techniques vs. Fujiwara test, *Desalination and Water Treatment* 51 (2013) 318–327.
- [C15] R. Verbeke, V. Gómez, I.F. Vankelecom, Chlorine-resistance of reverse osmosis (RO) polyamide membranes, *Progress in Polymer Science* 72 (2017) 1–15.
- [C16] N.P. Soice, A.R. Greenberg, W.B. Krantz, A.D. Norman, Studies of oxidative degradation in polyamide RO membrane barrier layers using pendant drop mechanical analysis, *Journal of Membrane Science* 243 (2004) 345–355.
- [C17] J.H. Oh, am Jang, Application of chlorine dioxide (ClO₂) to reverse osmosis (RO) membrane for seawater desalination, *Journal of the Taiwan Institute of Chemical Engineers* 68 (2016) 281–288.
- [C18] A. Antony, R. Fudianto, S. Cox, G. Leslie, Assessing the oxidative degradation of polyamide reverse osmosis membrane—Accelerated ageing with hypochlorite exposure, *Journal of Membrane Science* 347 (2010) 159–164.

- [C19]A. Ettori, E. Gaudichet-Maurin, J.-C. Schrotter, P. Aimar, C. Causserand, Permeability and chemical analysis of aromatic polyamide based membranes exposed to sodium hypochlorite, *Journal of Membrane Science* 375 (2011) 220–230.
- [C20]J. Glater, M.R. Zachariah, S.B. McCray, J.W. McCutchan, Reverse osmosis membrane sensitivity to ozone and halogen disinfectants, *Desalination* 48 (1983) 1–16.
- [C21]J. Glater, M.R. Zachariah, A Mechanistic Study of Halogen Interaction with Polyamide Reverse-Osmosis Membranes, in: S. Sourirajan, T. Matsuura (Eds.), *Reverse Osmosis and Ultrafiltration*, American Chemical Society, Washington, D.C., 1985, pp. 345–358.
- [C22]Da Silva, M. K., Wada, K., I.C. Tessaro, Investigation of oxidative degradation of polyamide reverse osmosis membranes by monochloramine solutions, *Journal of Membrane Science* 282 (2006) 375–382.
- [C23]W.R. Adams, The effects of chlorine dioxide on reverse osmosis membranes, *Desalination* 78 (1990) 439–453.
- [C24]E. Alayemieka, S. Lee, Modification of polyamide membrane surface with chlorine dioxide solutions of differing pH, *Desalination and Water Treatment* 45 (2012) 84–90.
- [C25]R. Cruz-Silva, S. Inukai, T. Araki, A. Morelos-Gomez, J. Ortiz-Medina, K. Takeuchi, T. Hayashi, A. Tanioka, S. Tejima, T. Noguchi, M. Terrones, M. Endo, High Performance and Chlorine Resistant Carbon Nanotube/Aromatic Polyamide Reverse Osmosis Nanocomposite Membrane, *MRS Advances* 1 (2016) 1469–1476.
- [C26]H. Huang, S. Lin, L. Zhang, L. Hou, Chlorine-Resistant Polyamide Reverse Osmosis Membrane with Monitorable and Regenerative Sacrificial Layers, *ACS applied materials & interfaces* 9 (2017) 10214–10223.
- [C27]C.Y. Tang, Y.-N. Kwon, J.O. Leckie, Effect of membrane chemistry and coating layer on physiochemical properties of thin film composite polyamide RO and NF membranes, *Desalination* 242 (2009) 149–167.
- [C28]K. Hashiba, S. Nakai, W. Nishijima, M. Ohno, T. Gotoh, Degradation of secondary polyamide reverse osmosis membrane by hypochlorite in the presence of calcium ions, *Polymer Degradation and Stability* 181 (2020) 109351.
- [C29]L. Rezaei, M. Dehghani, A.H. Hassani, V. Alipour, Seawater reverse osmosis membrane fouling causes in a full scale desalination plant; through the analysis of environmental issues: raw water quality, *Environ Health Eng Manag* 7 (2020) 119–126.
- [C30]S.P. Chesters, N. Pena, S. Gallego, M. Fazel, M.W. Armstrong, F. Del Vigo, Results from 99 seawater RO membrane autopsies, *IDA Journal of Desalination and Water Reuse* 5 (2013) 40–47.
- [C31]F. Kücke, *Die Erzeugung von Chlordioxid für den menschlichen Gebrauch*, Wiley VCH Verlagsgesellschaft 2005 1–18.
- [C32]D. Angyal, I. Fábrián, M. Szabó, Kinetic Role of Reactive Intermediates in Controlling the Formation of Chlorine Dioxide in the Hypochlorous Acid-Chlorite Ion Reaction, *Inorganic chemistry* 62 (2023) 5426–5434.
- [C33]J. Han, X. Zhang, W. Li, J. Jiang, Low chlorine impurity might be beneficial in chlorine dioxide disinfection, *Water research* 188 (2021) 116520.
- [C34]World health organisation, Chlorine dioxide, chlorite, and chlorate in drinking water, Background document for development of WHO Guidelines for Drinking-water Quality, 2016.

- [C35]M.A. Rouf, The Effect of Sulfuric Acid, Persulfate and Acetic Anhydride on the Preparation of Chlorine Dioxide from Chlorite Solution. Dissertation, Rajshahi, Bangladesh, 2013.
- [C36]S. Hager, H. Oesinghaus, A. Bachmann, M. Meinardus, T. Hofmann, K. Glas, CaCO₃ deposits in reverse osmosis: Part III – Incipient Scaling detection via polymer optical fibre sensors. Comparison to hydrochemical prediction and image analytical methods, *Brewing science* (2023) 19–29.
- [C37]S.T. Mitrouli, M. Kostoglou, A.J. Karabelas, Calcium carbonate scaling of desalination membranes: Assessment of scaling parameters from dead-end filtration experiments, *Journal of Membrane Science* 510 (2016) 293–305.
- [C38]A.J. Karabelas, M. Kostoglou, S.T. Mitrouli, Incipient crystallization of sparingly soluble salts on membrane surfaces: The case of dead-end filtration with no agitation, *Desalination* 273 (2011) 10: 117.
- [C39]J. Powell, J. Luh, O. Coronell, Amide Link Scission in the Polyamide Active Layers of Thin-Film Composite Membranes upon Exposure to Free Chlorine: Kinetics and Mechanisms, *Environmental science & technology* 49 (2015) 12136–12144.
- [C40]D.H. Shin, N. Kim, Y.T. Lee, Modification to the polyamide TFC RO membranes for improvement of chlorine-resistance, *Journal of Membrane Science* 376 (2011) 302–311.
- [C41]DuPont Company, Water Chemistry and Pretreatment-Biological Fouling Prevention (Chlorination/Dechlorination), 15th ed., Wilmington USA, 2022.
- [C42]V. Rougé, S. Allard, J.-P. Croué, U. von Gunten, In Situ Formation of Free Chlorine During ClO₂ Treatment: Implications on the Formation of Disinfection Byproducts, *Environmental science & technology* 52 (2018) 13421–13429.
- [C43]Z. Zhai, Z. Xu, Q.J. Niu, Boosting the performance of reverse osmosis membrane by macrocyclic molecule through interfacial coordination-driven strategy, *Journal of Membrane Science* 689 (2022) 122162.
- [C44]J. Xu, Z. Wang, X. Wei, S. Yang, J. Wang, S. Wang, The chlorination process of crosslinked aromatic polyamide reverse osmosis membrane: New insights from the study of self-made membrane, *Desalination* 313 (2013) 145–155.
- [C45]L. Valentino, T. Renkens, T. Maugin, J.-P. Croué, B.J. Mariñas, Changes in physicochemical and transport properties of a reverse osmosis membrane exposed to chloraminated seawater, *Environmental science & technology* 49 (2015) 2301–2309.
- [C46]J. Glater, S. Hong, M. Elimelech, The search for a chlorine-resistant reverse osmosis membrane, *Desalination* 95 (1994) 325–345.
- [C47]H. Park, Y.-C. Hung, D. Chung, Effects of chlorine and pH on efficacy of electrolyzed water for inactivating *Escherichia coli* O157:H7 and *Listeria monocytogenes*, *International journal of food microbiology* 91 (2004) 13–18.
- [C48]C. Liang, C.-F. Huang, Y.-J. Chen, Potential for activated persulfate degradation of BTEX contamination, *Water research* 42 (2008) 4091–4100.
- [C49]I.R. Epstein, K. Kustin, R.H. Simoyi, Systematic design of chemical oscillators. 78. Kinetics and mechanism of the chlorite-thiourea reaction in acidic medium, *J. Phys. Chem.* 96 (1992) 5852–5858.
- [C50]C.P. Koutsou, S.G. Yiantsios, A.J. Karabelas, A numerical and experimental study of mass transfer in spacer-filled channels: Effects of spacer geometrical characteristics and Schmidt number, *Journal of Membrane Science* 326 (2009) 234–251.

4 Discussion

Innovative methods for tackling membrane fouling are critical for the proper function of reverse osmosis (RO) filtration systems, especially for many industrial processes in which feed water with high nutrient and/or microbial loads is used. However, most anti-fouling treatments are implemented only after significant biofilm or mineral deposits have already formed, which necessitates the use of harsh reagents or processes that lead to membrane damage. To address this challenge, this thesis developed an approach using polymer optical fibers (POFs) for the early detection of fouling in RO processes, with the aim of facilitating more benign treatment strategies that can ultimately extend the operating lifetime of RO membranes. Moreover, chemical component analyses were carried out on commonly used membrane disinfection solutions, and the results of these analyses provide insights into the undesirable side effects of *in-situ* generated chemical by-products on RO membrane integrity. Based on these results, alternative treatment protocols were proposed that more effectively reverse the effects of fouling without sacrificing membrane performance.

In Chapters 3.1 and 3.2, a POF sensor was developed, installed, and tested in RO filtration setups, which enabled the early detection of both scaling in the form of calcite, gypsum, celestite, and barite mineral deposits (Chapter 3.1) and of biofilm formation in feed water with a microbial load representative of typical tap water installations (Chapter 3.2). In these setups, the POF sensor was either placed under the feed spacer (Chapter 3.1) or incorporated into the feed spacer structure itself (Chapter 3.2). The employed *ex-situ* and *in-situ* orientations not only minimized the impact of the newly developed POF sensor on the dynamic flow conditions encountered in the spacer-filled feed channels but also facilitated the detection of changes in the filtration setup caused by antiscalants (Chapter 3.1) and pulsatile crossflow conditions (Chapter 3.2). Moreover, the POF installation provided real-time information on the effectiveness of biofilm removal processes. Finally, Chapter 3.3 elucidates the effects of different components of chlorine dioxide disinfectant solutions on RO filtration processes. The insights gained in this chapter pave the way for new anti-fouling treatments that balance potential loss of RO membrane integrity with the gains in membrane performance afforded by fast and effective eradication of biofouling.

The following chapter separates the discussion of the achieved benchmarks into three parts: (1) a discussion of how POFs can be used to detect fouling much earlier than other monitoring systems, (2) the application of chlorine dioxide in RO systems in the context of other membrane integrity studies, and (3) an evaluation of the proposed fouling detection and countermeasure system.

4.1 Early detection of fouling using polymer optical fibers

The early detection of fouling made possible by POF sensors was crucial for the effectiveness of anti-fouling countermeasures that were applied to combat the initial formation of mineral nuclei as well as the surface adhesion of microorganisms as the first step of biofilm formation. Only if the countermeasures were adjusted to the first presence of crystal nuclei or onset of biofilm formation can a performance loss of the RO membrane be avoided. Since both types of fouling were typically detected in different ways, the following discussions concerning early fouling detection were treated separately for scaling (Section 4.1.1) and biofouling (Section 4.1.2).

4.1.1 Detecting the early onset of scaling

The formation of crystals at the membrane surface lead to a buildup of osmotic pressure [125]. This increased osmotic pressure decrease the flux across the membrane, which in turn decreases the membrane's permeability [36]. Thus, the presence of crystals on the surface of the reverse osmosis membrane is often detected indirectly by measuring the conductivity of the permeate, since this fluctuates in line with the osmolality of the permeate. In contrast, the POF system introduced in Chapter 3.1 provided a more direct and sensitive method for detection of crystal growth, the effectiveness of which was evaluated by directly comparing the results obtained from the POF sensor with other commonly monitored online performance parameters. As part of the first experimental setup presented in Chapter 3.1, CaCO_3 crystal formation was induced by dosing NaOH into the recycled feed. The setup was implemented in this way in order to quickly saturate the feed with all precursors for heterogeneous and homogeneous crystallization and thus promoted the formation of all known polymorphs of CaCO_3 . While filtering the saturated feed through the membrane, the signals of the POF and the online parameters, as well as the saturation points of the precursors for the CaCO_3 crystallization, were measured.

However, in our experiments, it was not immediately clear whether the change in the salt passage was caused by the changing pH [130, 131] or by the first crystallization nuclei that formed on the membrane surface. Generally, salt passage through a membrane is most efficient when the latter has reached its optimal electric charge. If the pH of the feed increases, salt passage through the membrane decreases until the membrane reaches its optimum and then increases again. Moreover, in our experimental setup, the increase in salt passage at pH values above the membrane's charge optimum could possibly coincide with the beginning of crystallization. Thus, in order to precisely determine the charge optimum of the polyaramid layer, experiments were carried out in triplicate using a 4 mmol L^{-1} phosphate buffer in full recycling mode (Figure 4.1). The experiment was started at pH 4, and a 0.5 mol L^{-1} NaOH solution was added to the feed stream at a flow rate of 10 mL h^{-1} during the experiment. The experiment, hence, used comparable experimental conditions to

those displayed in Figure 3.6 but without the risk of mineral formation on the RO membrane.

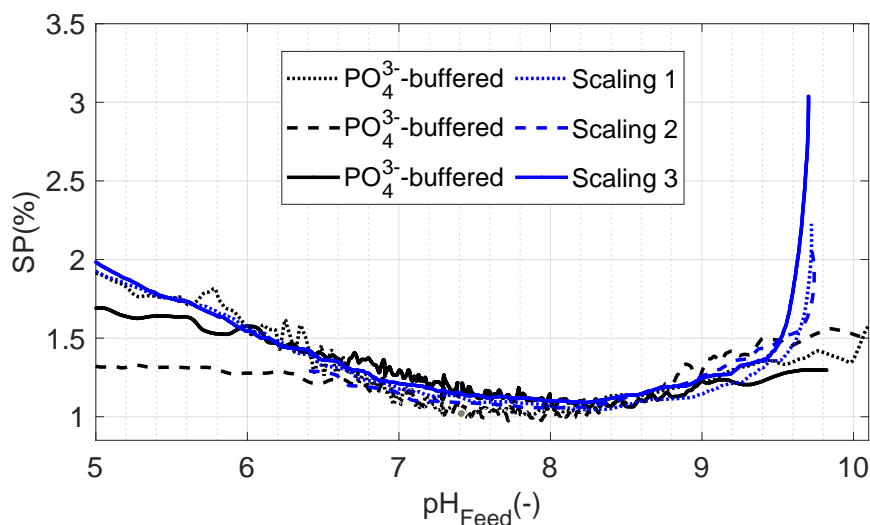


Figure 4.1: Plot depicting the salt passage as a function of pH in the feed for different filtration runs through the RO pilot plant. Black traces indicated trials carried out using a phosphate-buffered feed in which no scaling events were detected, while the blue traces correspond to runs with un-buffered feed for which scaling events were detected at pH values above 9.5. The experiments using a phosphate-buffered feed were carried out under comparable experimental conditions to those shown in Figure 3.6. For all trials, the minimum salt passage coincides with the membrane’s isoelectric point at pH 8.

Figure 4.1 shows that salt passage through the membrane reached a minimum at the optimal charge point of the RO membrane, which occurred when the feed is at pH 8. This indicates that the change in the salt passage trend in Figure 3.6 was likely due to changes in the properties of the polyaramid layer and not to the presence of the first crystal nuclei. At pH values above 9.5, scaling events for the un-buffered feeds were detected via a rapid increase in salt passage (Figure 4.1). Moreover, the feed channel pressure drop indicated that scaling occurs hours after changes in the POF signal were detected and was in line with the saturation point of amorphous calcium carbonate (ACC). Thus, the changes in POF signal were likely a consequence of homogeneous CaCO_3 crystallization in the cross-flowing bulk. Taken together, these data indicate that the POF sensor signals the onset of scaling much earlier than the commonly monitored RO performance parameters.

In addition to monitoring the conventional online parameters, we obtained an image-processed signal from a camera focused on the membrane surface, and a simulation using the Langier saturation index (LSI) was carried out for the experiment as well. The visible crystals on the membrane surface were identified hours after the POFs indicated first the presence of crystal nuclei. On the other hand, the simulation of saturation using the LSI suggested that the saturation point was reached at the same time the changes in the POF signals were detected, thus providing evidence that the POF sensor can detect the onset of crystal growth at a very early stage.

Despite these encouraging results, one drawback of the experimental setup reported in Chapter 3.1 is that the pH of the feed solutions used to induce the saturation of CaCO_3 was much higher than in typical use cases. Therefore, an alternative experimental setup was devised to demonstrate the POFs' functionality for a feed with constant calcite supersaturation in a pH range closer to that of industrial water feeds. The feed was not saturated for the other polymorphs of calcium carbonate, namely MCC and ACC. In the experiments in Chapter 3.1, the POF indicated scale formation earlier than all other previously discussed measurands, none of which show the presence of scaling via the typical parameters of salt passage, permeability, or feed channel pressure drop (FCP) for hours after the crystals were detected by the POF. Intriguingly, the timeframe of the scale formation indicated the POF, as well as the image analysis performed on the membrane surface, clearly showed that scaling started to occur before the known precursor MCC is saturated, thus contradicting existing theories of crystal nuclei formation [35]. This apparent contradiction can be partly explained by how the POF was installed in the feed channel for the RO experiments, which could result in higher local saturation due to increased concentration polarization effects. As a result of these local higher concentrations, the POF could detect the crystallization nuclei formed by the flow shadows caused by the sensor itself.

Although the POFs in these two experimental setups present a promising approach for early scaling detection, the POF sensors could not be directly compared against other *in-situ* detection methods such as ultrasonic time domain reflectometry (UTDR) and electrical impedance spectrometry (EIS) in the experimental setups carried out. The RO pilot plant that was used did not allow an implementation of these techniques. However, to the best of my knowledge, the excellent agreement between the timeframe of the detected POF signals and the saturation times predicted by simulations is unprecedented and has so far not been achieved using UTDR and EIS methods. Thus, using POF sensors in combination with simulations represents a highly effective method for the detection of scaling before mineral crystallization impedes the RO process.

4.1.2 Detecting the early onset of biofilm formation

Biological fouling is different from scaling, as it involves the formation of deposits on the feed spacers rather than on the membrane [139]. The distinction between scaling and biofouling is in how they form and when intervention is most effective. Biofouling formation involves different phases, which determine the best time for effective intervention [57]. The speed at which crystals form depends on the degree of supersaturation. Therefore, early monitoring is more crucial for biofouling than for scaling.

In Chapter 3.2, the POF was incorporated into the feed spacer, and the sensor zone was not created by removing the fluoropolymer coating with ethyl acetate rather than through mechanical abrasion. This manufacturing method was thought to

result in a higher surface roughness, which makes it easier for microorganisms to adhere to the surface of the POF and generate a detectable change in light transmission through the POF. In this vein, Chapter 3.2 utilized a standardized method for growing biofilms on RO membranes [63, 72] in order to accelerate biofouling in the feed channel of the RO membranes. This method aimed to demonstrate the effectiveness of POF sensors for detecting biofilm formation.

The primary challenge faced by a POF-based system for detecting biofouling was the long-term stability of the POF signal. Over time, the POF's ability to transfer light could be hampered by water uptake or mechanical stress when the POF is incorporated into the membrane flat cell [140]. Since biofilm growth was indicated by a decrease in the POF's light transmission signal, presumably due to an attenuation of the evanescent fields traveling through the POFs, the long-term effect (water uptake and mechanical stress) of the POF impedes the actual measurement. According to our findings, the POF signal stabilized after around 96 h. Once the signal was stabilized, the POFs were able to detect biofouling before any online or offline parameters were affected by the presence of biofilm in the feed channel. Only offline measurements of the total organic carbon and its balancing through the flow rates in the feed, retentate and permeate indicated the accumulation of organic carbon, and therefore the onset of biofilm formation, in the feed channel. Moreover, removal of the biofilm by using pulsatile cross-flow conditions, so temporary higher cross-flow velocities led to a recovery of the original POF transmission signal, providing further confirmation that the loss in POF signal was in fact due to biofilm formation. Having said that, it was determined that post-adaptation mechanisms (water uptake and mechanical stress) could overlap with the actual measurement of biofilm growth (see Figure 3.18). Therefore, due to the conditions used and signal adaptation phase of the POF in the first few hours, no real statements can be made about the presence of biofouling.

Moving forward, further improvements in biofouling detection could be gained by designing the reported POF sensors such that biofilm formation has a higher impact on the POF's transmission, as this would ensure accurate monitoring of biofouling at all formation phases. The hypothesis that microorganisms influence evanescence fields could explain why the impact of microorganisms on the light transmission of POFs is much less than the scattering of mineral crystals. Given that CaCO_3 crystals have a higher optical density than the fiber core, these crystals scatter light out of the fiber and thus directly influence the total reflection of light within the fiber [50–53]. Microstructured fibers with sensor zones that consist of functional binding groups, such as extracellular protein serving as substrate, areas with partly higher surface roughness or silicon based micropillar arrays [141–143], could enhance future microorganism detection by increasing the effectiveness with which microorganisms bind to the fiber surface and thus influence the POF signal.

In conclusion, despite the potential drawbacks of using POFs for biofouling detection, POFs were in principle capable of detecting, under the right conditions, the adhesion of biological material at the earliest possible stages. In addition, the monitoring of countermeasures against biofouling was also possible.

4.2 Sensitivity of polymer optical fibers to existing anti-fouling treatments

From a process engineering standpoint, POF sensors fill a gap in the portfolio of methods available for monitoring crucial membrane processes. For example, real-time information from POF sensors could be used to activate pumps that dose controlled amounts of antiscalants or biocides into the feed stream of RO filtration setups. Alternatively, POFs could be used to notify RO filtration operators when the spiral wound modules are in need of cleaning. In these ways, POF sensors hold promise as a feasible strategy for preserving membrane process performance and protecting RO membranes from the impacts of various types of fouling. However, in order for POF sensor systems to be effectively used in industrial settings, the impact of different anti-fouling treatments on the POFs themselves must be well understood.

To address this question, experiments were first carried out in Chapter 3.1 to evaluate how the extent of CaCO_3 crystallization and, hence, the POF signal was affected by the concentration of antiscalant employed. The findings showed that high concentrations of the antiscalant, in this case, a hexametaphosphate-based MT4000 chemical, maintained a higher light transmission through the core of the POF, demonstrating the retarded crystal formation. However, the experiments with the POF and antiscalant were only performed *ex-situ* without using the POF in a real membrane flat channel. Therefore, the effects of concentration polarization and flow conditions were not taken into account in the POF tests with antiscalants. A final demonstration that the POF can control the antiscalant concentration in the feed channel is still pending.

In Chapter 3.2, the POF was used under pulsatile cross-flow conditions. This means that the cross-flow velocity was temporarily increased to achieve higher shear rates on the feed spacer and membrane surfaces. These higher shear rates have been shown to enhance cleaning efficacy and thus reduce fouling impact on the flux or permeability of a membrane [144, 145]. Moreover, other studies employed pulsatile cross-flow using a sinusoidal oscillation, involving the trans membrane pressure (TMP) and the cross-flow velocity [144–146]. In the setup reported in Chapter 3.2, a different approach was used to demonstrate the POF's ability to monitor the cleavage of biomass from its surface. In this case, the cross-flow rate was increased at certain times when biomass accumulation was expected. The POF signal recovered immediately after the higher flow rate was applied, thus proving that POF sensors can quickly adapt to high fluid shear conditions.

In conclusion, POFs were found to be able to react favorably to antiscalant dosing and to alternate process conditions such as pulsatile cross-flow. Thus, fouling countermeasures can be readily implemented in POF-containing RO systems by altering the hydrodynamic conditions in the feed channel and using chemical cleaning agents.

4.3 Chlorine dioxide as a biocide for reverse osmosis membranes

Other than antiscalants, another commonly used chemical treatment in research and industrial-scale RO purification systems is chlorine dioxide [103, 115, 147], which is a biocide used to combat the growth of biofilm on RO membranes. However, while chlorine dioxide is effective at limiting the amount of viable microorganisms in the feed and on the membrane surface, the biocide also tends to impede the membrane rejection efficiency and permeability [103, 115, 147]. Thus far, studies that have attempted to determine the origin of the detrimental effects of chlorine dioxide have fallen short. This has been largely due to the fact that the chlorine dioxide is either employed under active filtration conditions with a TMP and differing cross-flow velocities or by immersing the membrane only in a chlorine dioxide solution that induces variable levels of mechanical stress on the membrane [111]. Furthermore, the configuration of the RO plants employed was inconsistent across these different studies, meaning that the used materials and surfaces were not comparable [12, 103, 111, 114, 120]. For example, the use of iron or other transition metals in the RO plant could accelerate membrane damage and complicate the analysis [148]. Thus, it is difficult to discern to what extent the membrane damage observed in these studies was due to the use of chlorine dioxide or mechanical stress on the membrane.

To address this issue, Chapter 3.3 of this dissertation investigated chlorine dioxide usage by soaking RO membranes in the isolated chemical by-products of a commercially available chlorine dioxide matrix. Conventional analytical techniques were employed to detect the ensuing damage to the membranes, with the aim of evaluating the sensitivity and reliability of these techniques for assessing RO membrane damages. To this end, chlorine dioxide was purified via gas stripping.

It was observed in several experiments that by avoiding membrane-damaging by-products and disinfecting the membrane during less mechanical stress, the membrane stayed nearly intact.

It is important to note that the chlorine dioxide concentrations used here for the membrane disinfection trials were approximately 5000 times higher than that normally used for water disinfection. Therefore, the extent of membrane damage observed in these studies is highly accelerated compared to standard disinfection conditions [121].

Overall, the results in Chapter 3.3 provide a valuable contribution to our understanding of the compatibility of chlorine dioxide disinfection with RO membranes. Having said that, further research is needed to understand more precisely what reactions occur in the membrane's polyaramid layer, which would aid greatly in the development of more effective disinfectants.

4.4 Developments in fouling detection and prevention in reverse osmosis processes

In the previous sections, the feasibility of the developed sensing techniques and countermeasures that now seem usable for RO membrane fouling suppression has been discussed. The present chapter now discusses in detail the strengths, weaknesses, opportunities, and threats of the proposed strategies and detection methods.

The main **strength** of the fouling detection and countermeasure methods proposed herein is the ability of the fiber optical sensors to detect the early onset of scaling and biofouling and to respond quickly to the application of antiscalants and high cross-flow velocities. This enables the sensors to be used in conjunction with anti-fouling countermeasures to optimize these treatments and to avoid negative effects on the environment or the process itself. Another key strength are the insights gained into the effects of different components of chlorine dioxide on membrane integrity, since these findings should facilitate the optimization of disinfectant formulations for maximum effectiveness while avoiding membrane damage.

The key **opportunity** that arises from the studies presented herein is the possibility to upscale the employed monitoring and treatment strategies to industrial-scale RO plants. The combined approach to the detection and control scaling and biofouling enables the use of highly concentrated antiscalants in highly saturated feed solutions. The sensing enables the RO user to react to the likely accelerated biofilm formation that the highly concentrated antiscalants could provoke. In this context, one mitigation strategy could be to disinfect either the feed water or the membrane in a cleaning step. For this purpose, Chapter 3.3 demonstrated the possibility of using a more RO membrane-compatible chlorine dioxide solution. Finally, the opportunity to upscale the POF sensor principle could lead to lower cross-sensitivities. Generally, the SWMs typically used in large-scale RO setups do not contain metal housings. Therefore, the suspected periodic behavior of the POF, which is most likely caused by the temperature fluctuations of the metal housings that compress and decompress the entire flat membrane cell housing, could be eliminated when implementing the POF in SWMs.

Although increased cross-sensitivity can be expected in a large-scale setup, such effects have not yet been evaluated on a large scale. This is the major **weakness** of the fouling detection and fouling countermeasure concept. How the POF sensor works if it is implemented in an SWM has yet to be investigated. There could be a difference in the sensor technology, as the fiber connections are less mechanically stressed, and therefore, the modes (e.g., angle of total reflection) are different. However, these modes are important because the higher angles in the total reflection directly influence the evanescent fields. The best way to overcome this weakness is to use a combined membrane flat cell (MFC) setup with SWMs. The MFC could be installed in a bypass of the first SWM and the retentate stage to detect biofouling and scaling, as was investigated in this dissertation. Furthermore, to the best of my knowledge, the effects of combining antiscalants with chlorine dioxide, for ex-

ample as a result of chemical reactions between the two components, are currently unknown. For example, chlorine dioxide can likely oxidize the complex antiscalant molecules, a reaction which could render both countermeasures ineffective.

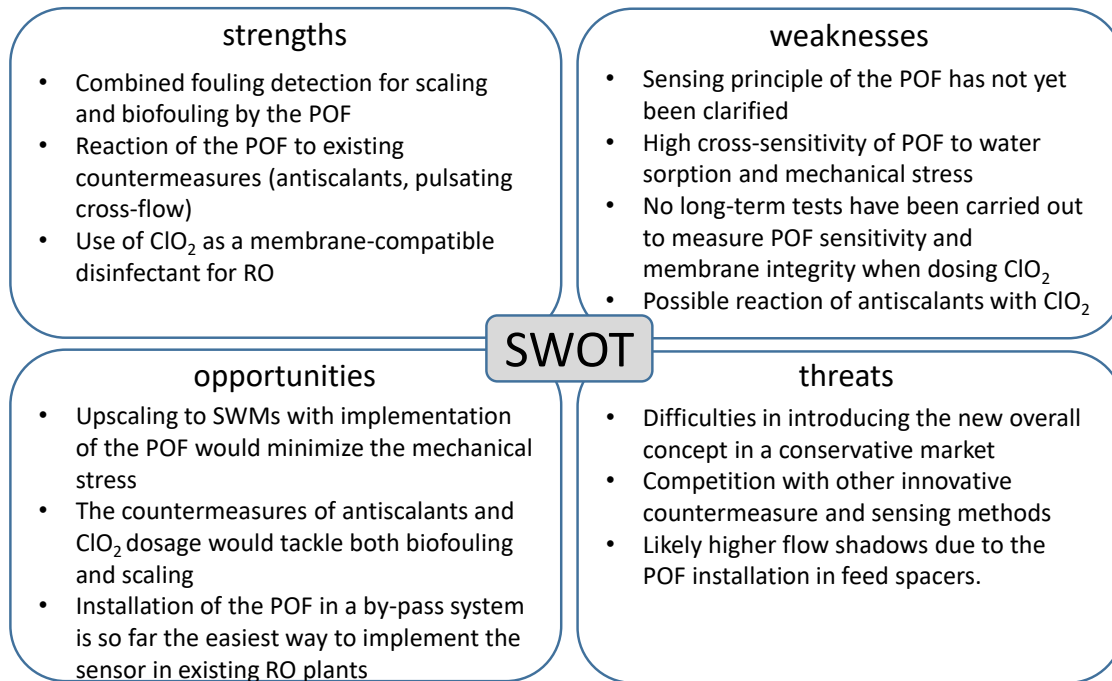


Figure 4.2: Diagram depicting the strengths, weaknesses, opportunities, and threats of the overall early POF sensing concept and combined countermeasures to prevent biofouling and scaling in reverse osmosis processes.

The main **threats** of applying the POF sensor system proposed herein, as well as the usage of chlorine dioxide in RO membrane systems, are primarily associated with the costs and risks that could be incurred when implementing these strategies in industrial-scale RO systems. For example, changing the methods by which SWMs are fabricated, which would be necessary to implement POFs in industrial membrane systems, is not feasible for most SWM manufacturers. At the same time, it is not clear if the POFs are stable enough for long-term usage in industrial RO plants that have been using their SWMs for several years. Moreover, chlorine dioxide usage is comparable to free chlorine for many RO membrane users. It is only known as a membrane-damaging biocide and, therefore, not easy to introduce into the water purification market. The dissection view on the chlorine dioxide matrix and its by-products is not widespread so far. Furthermore, the demonstrated use of chlorine dioxide was only for one week per experiment. Although very high concentrations were used during this time compared to the German drinking water ordinance, it is not possible to determine with certainty which effects long-term usage of chlorine dioxide would have on integrity of RO membranes. Despite the aforementioned weaknesses and threats, the strengths and opportunities of the proposed fouling detection and anti-fouling treatment strategies hold great potential for improving existing reverse osmosis processes and allowing them to operate more sustainably.

4.5 Future opportunities for anti-fouling sensing and treatment

In Chapter 1.5, the challenges encountered when using phosphate-based antiscalants to delay the induction time of mineral crystallization, as well as the issues that arise from accelerated biofilm growth due to high antiscalant dosages, are described. From the viewpoint of this dissertation, the best opportunity to deal with these issues is to detect both fouling types (i.e., scaling and biofouling) as soon as possible during the filtration process. To this end, optical fiber sensors are presented that can detect two types of fouling and monitor existing countermeasures. This will allow future RO membrane users to apply cleaning and countermeasure strategies at the earliest possible stages, without needing to take water samples from the feed, permeate, or retentate for offline analysis. If the POF is installed in future membrane modules, it can detect the early onset of biofouling in the first filtration stage, as well as scaling on the retentate side of the membrane. The importance of such an early detection strategy is emphasized by the fact that, the nutrient concentration, particularly that of assimilable carbon, nitrogen and phosphorus, are at their highest in the first stage of an RO system [55, 151].

On the other hand, in the retentate stage, the cross-flow velocity, concentration polarization, and ionic strength accelerate scale formation. Figure 4.3 illustrates a theoretical concentration and total recovery for stages with a 50 % recovery in each stage. In RO plants, heterogeneous crystallization is more favorable than homogeneous nucleation in the entering feed stream [29, 39]. This fact makes it unlikely that crystallization occurs earlier in the first RO stage. Therefore, a decreasing light transmission signal of a POF in the first stage module most likely signals the accumulation of biological growth, and a decreasing POF signal in the retentate stage most likely signals the first crystal nucleation in the RO module.

Beside the implementation of POFs in RO modules, the differences of fouling formation for scaling and biofouling can be used to enhance the usage of antiscalants and chlorine dioxide to combat fouling. For example, the antiscalants should only be dosed into the last stages of the RO system. In this way, the risk of deposits in the latter modules can be reduced, thus eliminating the risk that the antiscalant promotes biological growth in the early stages of the filtration process. Moreover, chlorine dioxide can be dosed into the inlet in its purified form, either continuously or during the flushing intervals. This would combat the biofilm growth where it would first appear. In addition, the antiscalant would not be degraded by the chlorine dioxide. Furthermore, biocide dosing during the flushing intervals is preferable, as the membrane is exposed to less mechanical stress, and thus, the risk of membrane degradation is reduced.

The application of the POF as well as the dosage points for chlorine dioxide and antiscalants that should be able to detect and counteract both fouling types in a differentiated way is depicted in Figure 4.3.

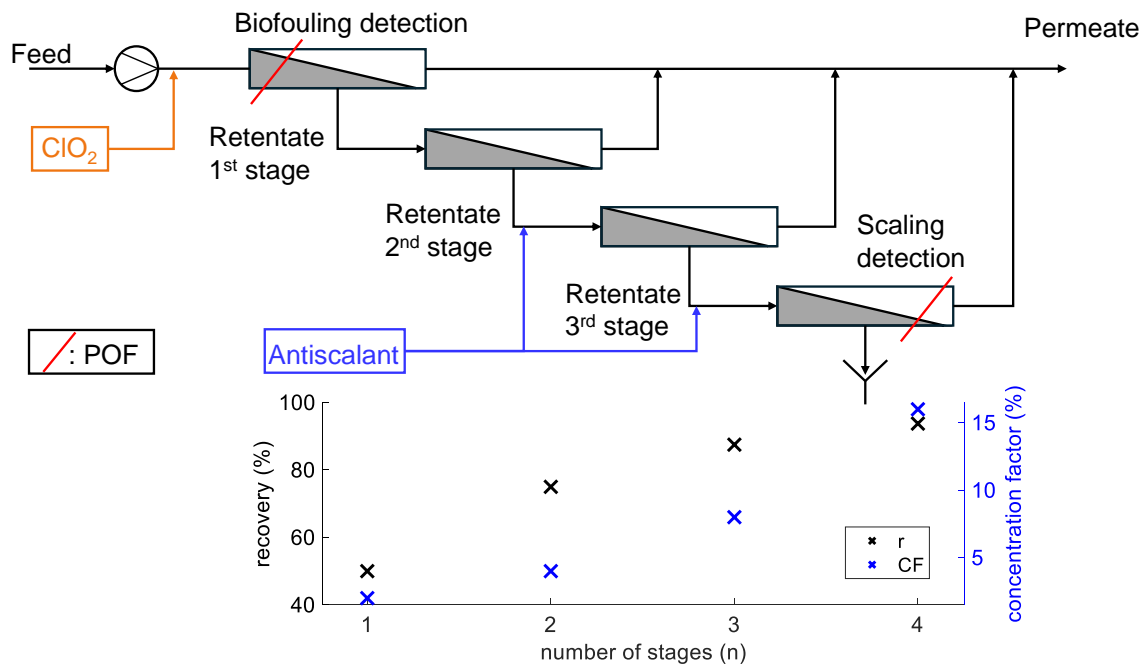


Figure 4.3: Top: Schematic depicting the application of SWM modules with POFs, antiscalants, and chlorine dioxide in a multi-stage reverse osmosis (RO) plant. The implementation of the POF could allow for detection of both biofouling in the first stage and scaling in the retentate stage. The targeted dosing of chlorine dioxide in the first module and of antiscalants in the latter modules would increase the effectiveness of these countermeasures. Bottom: Plot showing the recovery and concentration factors (left and right y-axes, respectively) that are caused at the indicated SWM stages (x-axis) with 50% recovery per stage.

Going forward, the results of this work are anticipated to design a future more sustainable reverse osmosis process that expands the lifespan of RO modules significantly. The development of fiber optic sensors and improvements in fouling countermeasures have allowed for a more effective approach to addressing the most common threat to the membrane separation process while minimizing damage to the membrane. The sensitivity of the fiber sensors now enables the early detection of fouling phenomena, which in turn allows for more precise countermeasures against fouling that could potentially harm the membrane. Additionally, through the identification of harmful components in the chlorine dioxide matrix produced and used *in-situ*, a disinfection process for the RO membrane became feasible. The now possible disinfection process enables the tandem consisting of antiscalants and biocides to counter the two most frequently occurring types of fouling. The antiscalants, which are effective against scaling, can be used to a high targeted concentration in the selected RO modules, since their biofilm-promoting effect is counteracted by the biocide chlorine dioxide in the earlier installed RO stages. Thus, this thesis contributes to a process development for water purification out of very different feed water qualities paving the way for drinking and industrial water production in regions suffering from water shortages.

Bibliography

- [1] S. Hager, H. Oesinghaus, A. Bachmann, M. Meinardus, T. Hofmann, and K. Glas. Caco3 deposits in reverse osmosis: Part iii – incipient scaling detection via polymer optical fibre sensors. comparison to hydrochemical prediction and image analytical methods. *Brewing science*, (76):19–29, 2023.
- [2] H. Oesinghaus, D. Wanken, K. Lupp, M. Gastl, M. Elsner, and K. Glas. Incipient biofouling detection via fiber optical sensing and image analysis in reverse osmosis processes. *Membranes*, 13(6), 2023.
- [3] H. Oesinghaus, E. E. Eiden, T. Kratky, M. J. Huber, S. Schrettl, S. Holz, M. Elsner, and K. Glas. Analytical characterization of damage in reverse osmosis membranes caused by components of a chlorine dioxide matrix. *Desalination and Water Treatment*, page 100633, 2024.
- [4] R. Baten and K. Stummeyer. How sustainable can desalination be? *Desalination and Water Treatment*, 51(1-3):44–52, 2013.
- [5] V. G. Gude. Desalination and water reuse to address global water scarcity. *Reviews in Environmental Science and Bio/Technology*, 16(4):591–609, 2017.
- [6] Ta-Kang Liu, Jia-An Ye, and Haw-Yang Sheu. Exploring the social acceptability for the desalination plant project: Perceptions from the stakeholders. *Desalination*, 532:115757, 2022.
- [7] N. Sreedhar, N. Thomas, N. Ghaffour, and H. A. Arafat. The evolution of feed spacer role in membrane applications for desalination and water treatment: A critical review and future perspective. *Desalination*, 554:116505, 2023.
- [8] P. S. Goh, W. J. Lau, M.H.D. Othman, and A. F. Ismail. Membrane fouling in desalination and its mitigation strategies. *Desalination*, 425:130–155, 2018.
- [9] P. Sperle, C. Wurzbacher, J. E. Drewes, and B. Skibinski. Reducing the impacts of biofouling in ro membrane systems through in situ low fluence irradiation employing uvc-leds. *Membranes*, 10(12), 2020.
- [10] S. Hager, H. Oesinghaus, A. Bachmann, M. Meinardus, T. Hofmann, and K. Glas. Caco3 deposits in reverse osmosis: Part iii – incipient scaling detection via polymer optical fibre sensors. comparison to hydrochemical prediction and image analytical methods. *Brewing science*, 1866-5195(76):19–29, 2023.
- [11] E. M. Kimani, M. Pranić, S. Porada, A.J.B. Kemperman, I. I. Ryzhkov, W.G.J. van der Meer, and P. M. Biesheuvel. The influence of feedwater ph on membrane charge ionization and ion rejection by reverse osmosis: An experimental and theoretical study. *Journal of Membrane Science*, 660:120800, 2022.

- [12] J. Glater, M. R. Zachariah, S. B. McCray, and J. W. McCutchan. Reverse osmosis membrane sensitivity to ozone and halogen disinfectants. *Desalination*, 48(1):1–16, 1983.
- [13] J. Glater and M. R. Zachariah. A mechanistic study of halogen interaction with polyamide reverse-osmosis membranes. In S. Sourirajan and T. Matsuura, editors, *Reverse Osmosis and Ultrafiltration*, volume 281 of *ACS Symposium Series*, pages 345–358. American Chemical Society, Washington, D.C., 1985.
- [14] A. Y. Al-Borno and M. Abdel-Jawad. Conventional pretreatment of surface seawater for reverse osmosis application, state of the art. *Desalination*, 74:3–36, 1989.
- [15] N. AlSawaftah, W. Abuwatfa, N. Darwish, and G. Husseini. A comprehensive review on membrane fouling: Mathematical modelling, prediction, diagnosis, and mitigation. *Water*, 13(9):1327, 2021.
- [16] P. García-Triñanes, M. A. Chairopoulou, and L. C. Campos. Investigating reverse osmosis membrane fouling and scaling by membrane autopsy of a bench scale device. *Environmental technology*, 43(21):3198–3211, 2022.
- [17] V. Geraldes, N. E. Pereira, and M. Norberta de Pinho. Simulation and optimization of medium-sized seawater reverse osmosis processes with spiral-wound modules. *Industrial & Engineering Chemistry Research*, 44(6):1897–1905, 2005.
- [18] L. Wang, Y. Sun, and B. Chen. Rejection of haloacetic acids in water by multi-stage reverse osmosis: Efficiency, mechanisms, and influencing factors. *Water research*, 144:383–392, 2018.
- [19] D. van Gauwbergen and J. Baeyens. Modeling and scaleup of reverse osmosis separation. *Environmental Engineering Science*, 19(1):37–45, 2002.
- [20] M. Qasim, M. Badrelzaman, N. N. Darwish, N. A. Darwish, and N. Hilal. Reverse osmosis desalination: A state-of-the-art review. *Desalination*, 459:59–104, 2019.
- [21] H. Luo, Y. Cui, H. Zhang, C. Li, Z. Wang, and P. Song. Analyzing and verifying the association of spiral-wound reverse osmosis membrane fouling with different secondary effluents: full-scale experiments. *The Science of the total environment*, 711:135150, 2020.
- [22] Y. Al-Wazzan, M. Safar, S. Ebrahim, N. Burney, and A. Mesri. Desalting of subsurface water using spiral-wound reverse osmosis (ro) system: technical and economic assessment. *Desalination*, 143(1):21–28, 2002.
- [23] Y. Zhao, L. Song, and S. L. Ong. Fouling behavior and foulant characteristics of reverse osmosis membranes for treated secondary effluent reclamation. *Journal of Membrane Science*, 349(1-2):65–74, 2010.

- [24] S. R. Pandey, V. Jegatheesan, K. Baskaran, and L. Shu. Fouling in reverse osmosis (ro) membrane in water recovery from secondary effluent: a review. *Reviews in Environmental Science and Bio/Technology*, 11(2):125–145, 2012.
- [25] S. F. E. Boerlage. *Scaling and particulate fouling in membrane filtration systems*. Swets & Zeitlinger, Lisse, 2001.
- [26] J. S. Vrouwenvelder, C. Hinrichs, W. G. J. van der Meer, M. C. M. van Loosdrecht, and J. C. Kruithof. Pressure drop increase by biofilm accumulation in spiral wound ro and nf membrane systems: role of substrate concentration, flow velocity, substrate load and flow direction. *Biofouling*, 25(6):543–555, 2009.
- [27] A. Karanasiou, A. J. Karabelas, and S. T. Mitrouli. Incipient membrane scaling in the presence of polysaccharides during reverse osmosis desalination in spacer-filled channels. *Desalination*, 500:114821, 2021.
- [28] A. J. Karabelas, M. Kostoglou, and S. T. Mitrouli. Incipient crystallization of sparingly soluble salts on membrane surfaces: The case of dead-end filtration with no agitation. *Desalination*, 273(1):105–117, 2011.
- [29] A. J. Karabelas, M. Kostoglou, and S. T. Mitrouli. Incipient crystallization of sparingly soluble salts on membrane surfaces: The case of dead-end filtration with no agitation. *Desalination*, 273(1):105–117, 2011.
- [30] H. Elfil and A. Hannachi. Reconsidering water scaling tendency assessment. *AIChE Journal*, 52(10):3583–3591, 2006.
- [31] S. Hager, A. Bachmann, T. Hofmann, R. Engelbrecht, and Karl Glas. Caco3 deposits in reverse osmosis part i - shortcomings of current approaches leading to a new prediction model and monitoring device. *Brewing science*, (74):122–133, 2021.
- [32] S. Hager, M. Meinardus, T. Hofmann, and K. Glas. Caco3 deposits in reverse osmosis: Part ii - simulation model for hydrochemical predictions of reverse osmosis retentates and scaling propensity. *Brewing science*, 75:54–68, 2022.
- [33] N. Wada, K. Yamashita, and T. Umegaki. Effects of silver, aluminum, and chrome ions on the polymorphic formation of calcium carbonate under conditions of double diffusion. *Journal of Colloid and Interface Science*, 201(1):1–6, 1998.
- [34] Xu-Rong Xu, An-Hua Cai, Rui Liu, Hai-Hua Pan, Rui-Kang Tang, and Kilwon Cho. The roles of water and polyelectrolytes in the phase transformation of amorphous calcium carbonate. *Journal of Crystal Growth*, 310(16):3779–3787, 2008.
- [35] H. Elfil. Role of hydrate phases of calcium carbonate on the scaling phenomenon. *Desalination*, pages 177–186, 2001.

- [36] A. Alshami, T. Taylor, N. Ismail, C. Buelke, and L. Schultz. Ro system scaling with focus on the concentrate line: Current challenges and potential solutions. *Desalination*, 520:115370, 2021.
- [37] A. Pervov. Scale formation prognosis and cleaning procedure schedules in reverse osmosis systems operation. *Desalination*, 83(1-3):77–118, 1991.
- [38] A. Pervov. Investigation of scaling and inhibition mechanisms in reverse osmosis spiral wound elements. *Membranes*, 12(9), 2022.
- [39] S. Mitrouli, A. J. Karabelas, A. Karanasiou, and M. Kostoglou. Incipient calcium carbonate scaling of desalination membranes in narrow channels with spacers—experimental insights. *Journal of Membrane Science*, 425-426:48–57, 2013.
- [40] Qian Liu, Guo-Rong Xu, and Rasel Das. Inorganic scaling in reverse osmosis (ro) desalination: Mechanisms, monitoring, and inhibition strategies. *Desalination*, 468:114065, 2019.
- [41] A. J. Karabelas, M. Kostoglou, and C. P. Koutsou. Modeling of spiral wound membrane desalination modules and plants – review and research priorities. *Desalination*, 356:165–186, 2015.
- [42] O. Söhnel and J. W. Mullin. Precipitation of calcium carbonate. *Journal of Crystal Growth*, 60(2):239–250, 1982.
- [43] N. Dhakal, S. G. Salinas Rodriguez, J. C. Schippers, and M. D. Kennedy. Induction time measurements in two brackish water reverse osmosis plants for calcium carbonate precipitation. *Desalination and Water Treatment*, 53(2):285–293, 2015.
- [44] Z.. Zhanag, A. R. Greenberg, W. B. Krantz, and G.-Y. Chai, editors. *New Insights into Membrane Science and Technology: Polymeric and Biofunctional Membranes*. Membrane Science and Technology. Elsevier, 2003.
- [45] J. Thompson, A. Rahardianto, S. Kim, M. Bilal, R. Breckenridge, and Y. Cohen. Real-time direct detection of silica scaling on ro membranes. *Journal of Membrane Science*, 528:346–358, 2017.
- [46] D. W. Thompson, M. J. DeVries, T. E. Tiwald, and J. A. Woollam. Determination of optical anisotropy in calcite from ultraviolet to mid-infrared by generalized ellipsometry. *Thin Solid Films*, 313-314:341–346, 1998.
- [47] D. J. Park, O. D. Supekar, A. R. Greenberg, J. T. Gopinath, and V. M. Bright. In-situ monitoring of calcium carbonate scale progression on reverse osmosis membranes using raman spectroscopy. *Desalination and Water Treatment*, 273:92–103, 2022.

- [48] A. J. Karabelas, S. T. Mitrouli, and M. Kostoglou. Scaling in reverse osmosis desalination plants: A perspective focusing on development of comprehensive simulation tools. *Desalination*, 474:114193, 2020.
- [49] M. Wang, B. Cao, Y. Hu, and D. F. Rodrigues. Mineral scaling on reverse osmosis membranes: Role of mass, orientation, and crystallinity on permeability. *Environmental Science & Technology*, 55(23):16110–16119, 2021.
- [50] M. Boerkamp, D. W. Lamb, and P. Lye. Progress in the application of exposed core, optical fibre sensors for detecting and monitoring surface crystallization processes. In L. Mazuray, R. Wartmann, A. Wood, J.-L. Tissot, and J. M. Raynor, editors, *Optical Design and Engineering III*, SPIE Proceedings, page 71002G. SPIE, 2008.
- [51] M. Boerkamp, D. W. Lamb, and P. G. Lye. Pmma optical fibers as intrinsic sensors of surface crystal growth. In D. D. Sampson, editor, *19th International Conference on Optical Fibre Sensors*, SPIE Proceedings, page 700440. SPIE, 2008.
- [52] M. Boerkamp, D. W. Lamb, P. G. Lye, C. M. Fellows, A. Al-Hamzah, and A. D. Wallace. Detecting and monitoring industrial scale formation using an intrinsic exposed-core optical fiber sensor. *Industrial & Engineering Chemistry Research*, 49(10):4682–4686, 2010.
- [53] D. W. Lamb, M. Boerkamp, and P. Lye. Monitoring surface crystal growth using an intrinsic exposed-core optical fiber sensor (iecofs). In D. D. Sampson, editor, *19th International Conference on Optical Fibre Sensors*, SPIE Proceedings, page 700424. SPIE, 2008.
- [54] H.-C. Flemming, G. Schaule, T. Griebe, J. Schmitt, and A. Tamachkiarowa. Biofouling—the achilles heel of membrane processes. *Desalination*, 113(2-3):215–225, 1997.
- [55] J. S. Vrouwenvelder, J. C. Kruithof, and M. C. M. van Loosdrecht. *Biofouling of spiral wound membrane systems*. IWA Publishing, London, 2011.
- [56] H.-C. Flemming, G. Schaule, T. Griebe, J. Schmitt, and A. Tamachkiarowa. Biofouling—the achilles heel of membrane processes. *Desalination*, 113(2-3):215–225, 1997.
- [57] H.-C. Flemming. Reverse osmosis membrane biofouling. *Experimental Thermal and Fluid Science*, 14(4):382–391, 1997.
- [58] A. I. Radu, J. S. Vrouwenvelder, M.C.M. van Loosdrecht, and C. Picioreanu. Modeling the effect of biofilm formation on reverse osmosis performance: Flux, feed channel pressure drop and solute passage. *Journal of Membrane Science*, 365(1-2):1–15, 2010.

- [59] J. S. Vrouwenvelder, S. M. Bakker, L. P. Wessels, and J.A.M. van Paassen. The membrane fouling simulator as a new tool for biofouling control of spiral-wound membranes. *Desalination*, 204(1-3):170–174, 2007.
- [60] J. S. Vrouwenvelder, S. A. Manolarakis, J. P. van der Hoek, J. A. M. van Paassen, W. G. J. van der Meer, J. M. C. van Agtmaal, H. D. M. Prummel, J. C. Kruithof, and M. C. M. van Loosdrecht. Quantitative biofouling diagnosis in full scale nanofiltration and reverse osmosis installations. *Water research*, 42(19):4856–4868, 2008.
- [61] A. Matin, Z. Khan, S.M.J. Zaidi, and M. C. Boyce. Biofouling in reverse osmosis membranes for seawater desalination: Phenomena and prevention. *Desalination*, 281:1–16, 2011.
- [62] M. Herzberg and M. Elimelech. Physiology and genetic traits of reverse osmosis membrane biofilms: a case study with pseudomonas aeruginosa. *The ISME journal*, 2(2):180–194, 2008.
- [63] P. Sperle, C. Wurzbacher, J. E. Drewes, and B. Skibinski. Reducing the impacts of biofouling in ro membrane systems through in situ low fluence irradiation employing uvc-leds. *Membranes*, 10(12), 2020.
- [64] H.-C. Flemming. Biofouling and me: My stockholm syndrome with biofilms. *Water research*, 173:115576, 2020.
- [65] E. I. Prest, F. Hammes, M. C. M. van Loosdrecht, and J. S. Vrouwenvelder. Biological stability of drinking water: Controlling factors, methods, and challenges. *Frontiers in microbiology*, 7:45, 2016.
- [66] E. van der Wende, W.G Characklis, and D.B Smith. Biofilms and bacterial drinking water quality. *Water research*, 23(10):1313–1322, 1989.
- [67] M.C.M. Bruijs, L. P. Venhuis, H. A. Jenner, D. G. Daniels, and G. J. Licina. Biocide optimization using an on-line biofilm monitor, 2001.
- [68] P. Cristiani and G. Perboni. Antifouling strategies and corrosion control in cooling circuits. *Bioelectrochemistry (Amsterdam, Netherlands)*, 97:120–126, 2014.
- [69] Giovanni Pavanello, Marco Faimali, Massimiliano Pittore, Angelo Mollica, Alessandro Mollica, and Alfonso Mollica. Exploiting a new electrochemical sensor for biofilm monitoring and water treatment optimization. *Water research*, 45(4):1651–1658, 2011.
- [70] J. C. Chen, Q. Li, and M. Elimelech. In situ monitoring techniques for concentration polarization and fouling phenomena in membrane filtration. *Advances in colloid and interface science*, 107(2-3):83–108, 2004.
- [71] P. Janknecht and L. F. Melo. Online biofilm monitoring. *Reviews in Environmental Science and Bio/Technology*, 2(2-4):269–283, 2003.

- [72] C. Dreszer, J. S. Vrouwenvelder, A. H. Paulitsch-Fuchs, A. Zwijnenburg, J. C. Kruithof, and H.-C. Flemming. Hydraulic resistance of biofilms. *Journal of Membrane Science*, 429:436–447, 2013.
- [73] G. Schock and A. Miquel. Mass transfer and pressure loss in spiral wound modules. *Desalination*, 64:339–352, 1987.
- [74] A. Balaji G., T. K. Radhakrishnan, G. Gobi, and D. Sastikumar. Fibre-optic sensors for the estimation of biofilm thickness on metals. In *Third European Workshop on Optical Fibre Sensors*, SPIE Proceedings, page 66191E. SPIE, 2007.
- [75] A. Rakhimbekova, B. Kudaibergenov, D. Moldabay, A. Zharylgap, O. M. Ajunwa, E. Marsili, and D. Tosi. Biofilm detection by a fiber-tip ball resonator optical fiber sensor. *Biosensors*, 12(7), 2022.
- [76] Nianbing Zhong, Yongwu Wu, Zhengkun Wang, Haixing Chang, Dengjie Zhong, Yunlan Xu, Xinyu Hu, and Liwen Huang. Monitoring microalgal biofilm growth and phenol degradation with fiber-optic sensors. *Analytical chemistry*, 91(23):15155–15162, 2019.
- [77] P. G. Lye, R. Bradbury, and D. W. Lamb. Evaluating a novel application of optical fibre evanescent field absorbance: rapid measurement of red colour in winegrape homogenates. In H. Tan, editor, *PIAGENG 2013: Image Processing and Photonics for Agricultural Engineering*, SPIE Proceedings, page 87610R. SPIE, 2013.
- [78] T. Orii, T. Okazaki, N. Hata, K. Sugawara, F. A. Rahman, and H. Kuramitz. Development of an attenuated total reflection based fiber-optic sensor for real-time sensing of biofilm formation. *Analytical sciences : the international journal of the Japan Society for Analytical Chemistry*, 33(8):883–887, 2017.
- [79] M. Fischer, M. Wahl, and G. Friedrichs. Design and field application of a uv-led based optical fiber biofilm sensor. *Biosensors & bioelectronics*, 33(1):172–178, 2012.
- [80] R. Philip-Chandy, P. J. Scully, P. Eldridge, H. J. Kadim, M. G. Grapin, M. G. Jonca, M. G. D’Ambrosio, and F. Colin. An optical fiber sensor for biofilm measurement using intensity modulation and image analysis. *IEEE Journal of Selected Topics in Quantum Electronics*, 6(5):764–772, 2000.
- [81] N. Zhong, Q. Liao, X. Zhu, and R. Chen. A fiber-optic sensor for accurately monitoring biofilm growth in a hydrogen production photobioreactor. *Analytical chemistry*, 86(8):3994–4001, 2014.
- [82] G. D. de Dobbeleer, M. H. Ledoux-Corbusier, and G. A. Achten. Graft versus host reaction. an ultrastructural study. *Archives of dermatology*, 111(12):1597–1902, 1975.

- [83] M. K. Shahid, M. Pyo, and Y.-G. Choi. The operation of reverse osmosis system with co2 as a scale inhibitor: A study on operational behavior and membrane morphology. *Desalination*, 426:11–20, 2018.
- [84] K. A. Indarawis and T. H. Boyer. Evaluation of ion exchange pretreatment options to decrease fouling of a reverse osmosis membrane. *Desalination and Water Treatment*, 52(25-27):4603–4611, 2014.
- [85] Lauren F. Greenlee, Fabrice Testa, Desmond F. Lawler, Benny D. Freeman, and Philippe Moulin. Effect of antiscalants on precipitation of an ro concentrate: metals precipitated and particle characteristics for several water compositions. *Water research*, 44(8):2672–2684, 2010.
- [86] T. Jain, E. Sanchez, E. Owens-Bennett, R. Trussell, S. Walker, and H. Liu. Impacts of antiscalants on the formation of calcium solids: implication on scaling potential of desalination concentrate. *Environmental Science: Water Research & Technology*, 5(7):1285–1294, 2019.
- [87] W. Yu, Di S., W. Chen, and H. Yang. Antiscalants in ro membrane scaling control. *Water research*, 183:115985, 2020.
- [88] Y. M. Al-Roomi and K. F. Hussain. Potential kinetic model for scaling and scale inhibition mechanism. *Desalination*, 393:186–195, 2016.
- [89] D. Hasson, H. Shemer, and A. Sher. State of the art of friendly “green” scale control inhibitors: A review article. *Industrial & Engineering Chemistry Research*, 50(12):7601–7607, 2011.
- [90] F. Rahman. Calcium sulfate precipitation studies with scale inhibitors for reverse osmosis desalination. *Desalination*, 319:79–84, 2013.
- [91] E. G. Darton. Membrane chemical research: centuries apart. *Desalination*, 132(1-3):121–131, 2000.
- [92] M. Y. Ashfaq, M. A. Al-Ghouti, H. Qiblawey, and N. Zouari. Evaluating the effect of antiscalants on membrane biofouling using ftir and multivariate analysis. *Biofouling*, 35(1):1–14, 2019.
- [93] X. A. M. Mutke, K. Tavichaiyuth, F. Drees, H. V. Lutze, and T. C. Schmidt. Oxidation of the nitrogen-free phosphonate antiscalants hedp and pbtc in reverse osmosis concentrates: Reaction kinetics and degradation rate. *Water research*, 233:119571, 2023.
- [94] X. A. M. Mutke, F. Drees, H. V. Lutze, and T. C. Schmidt. Oxidation of the n-containing phosphonate antiscalants ntmp and dtpmp in reverse osmosis concentrates: Reaction kinetics and degradation rate. *Chemosphere*, 341:139999, 2023.

- [95] J. S. Vrouwenvelder, F. Beyer, K. Dahmani, N. Hasan, G. Galjaard, J. C. Kruithof, and M. C. M. van Loosdrecht. Phosphate limitation to control biofouling. *Water research*, 44(11):3454–3466, 2010.
- [96] V. Bonnélye, L. Guey, and J. Del Castillo. Uf/mf as ro pre-treatment: the real benefit. *Desalination*, 222(1-3):59–65, 2008.
- [97] A. H. Alshahri, L. Fortunato, N. Zaouri, N. Ghaffour, and T. Leiknes. Role of dissolved air flotation (daf) and liquid ferrate on mitigation of algal organic matter (aom) during algal bloom events in ro desalination. *Separation and Purification Technology*, 256:117795, 2021.
- [98] L. Henthorne and B. Boysen. State-of-the-art of reverse osmosis desalination pretreatment. *Desalination*, 356:129–139, 2015.
- [99] G. Naidu, S. Jeong, S. Vigneswaran, and S. A. Rice. Microbial activity in biofilter used as a pretreatment for seawater desalination. *Desalination*, 309:254–260, 2013.
- [100] Ismail Koyuncu, Mark R. Wiesner, Cecile Bele, Gabriel Coriton, Malik Djafer, and Jacques Cavard. Bench-scale assessment of pretreatment to reduce fouling of salt-rejecting membranes. *Desalination*, 197(1-3):94–105, 2006.
- [101] Lenntech. Tech manual excerpt page 1 of 2 * trademark of the dow chemical company form no. 609-02102-704 filmtec membranes cleaning and sanitization: Sanitizing ro & nf membrane systems.
- [102] T. Fujioka, N. Oshima, R. Suzuki, M. Higgins, W. Price, R. K. Henderson, and L. D. Nghiem. Effect of heat treatment on fouling resistance and the rejection of small and neutral solutes by reverse osmosis membranes. *Water Supply*, 15(3):510–516, 2015.
- [103] W. R. Adams. The effects of chlorine dioxide on reverse osmosis membranes. *Desalination*, 78(3):439–453, 1990.
- [104] Julius Glater, Seung-kwan Hong, and Menachem Elimelech. The search for a chlorine-resistant reverse osmosis membrane. *Desalination*, 95(3):325–345, 1994.
- [105] D. Suresh, P. S. Goh, and A. F. Ismail. Dual functionalization of polyamide reverse osmosis thin film composite membrane for improving chlorine resistance. *Materials Today Communications*, 39:109238, 2024.
- [106] Y. Su, H. Peng, Y. Hu, S. Li, J. Rao, and Q. Zhao. Acid and chlorine-resistant cations selective nanofiltration membranes derived from hoffmann alkylation reaction. *Journal of Membrane Science*, 697:122591, 2024.
- [107] A. Etti, E. Gaudichet-Maurin, J.-C. Schrotter, P. Aimar, and C. Causserand. Permeability and chemical analysis of aromatic polyamide based membranes

- exposed to sodium hypochlorite. *Journal of Membrane Science*, 375(1-2):220–230, 2011.
- [108] Jun Xu, Zhi Wang, Xinyu Wei, Shangbao Yang, Jixiao Wang, and Shichang Wang. The chlorination process of crosslinked aromatic polyamide reverse osmosis membrane: New insights from the study of self-made membrane. *Desalination*, 313:145–155, 2013.
- [109] C. Y. Tang, Y.-N. Kwon, and J. O. Leckie. Effect of membrane chemistry and coating layer on physiochemical properties of thin film composite polyamide ro and nf membranes. *Desalination*, 242(1-3):149–167, 2009.
- [110] Y. N. Kwon and J. O. Leckie. Hypochlorite degradation of crosslinked polyamide membranesii. changes in hydrogen bonding behavior and performance. *Journal of Membrane Science*, 282(1-2):456–464, 2006.
- [111] R. Verbeke, V. Gómez, and I. F.J. Vankelecom. Chlorine-resistance of reverse osmosis (ro) polyamide membranes. *Progress in Polymer Science*, 72:1–15, 2017.
- [112] H. Huang, S. Lin, L. Zhang, and L. Hou. Chlorine-resistant polyamide reverse osmosis membrane with monitorable and regenerative sacrificial layers. *ACS applied materials & interfaces*, 9(11):10214–10223, 2017.
- [113] S. Hager, E. Henrichs, T. Hofmann, and K. Glas. Umkehrosmose und chlor-dioxid: Einflüsse auf die prozessperformance und bedarfsgerechte dosage. *Chemie Ingenieur Technik*, 91(8):1152–1156, 2019.
- [114] A. Antony, R. Fudianto, S. Cox, and G. Leslie. Assessing the oxidative degradation of polyamide reverse osmosis membrane—accelerated ageing with hypochlorite exposure. *Journal of Membrane Science*, 347(1-2):159–164, 2010.
- [115] S. Avlonitis, W. T. Hanbury, and T. Hodgkiess. Chlorine degradation of aromatic polyamides. *Desalination*, 85(3):321–334, 1992.
- [116] C. Gablich, J. Frankin, F. Gerringer, K. Ishida, and I. H. Suffet. Enhanced oxidation of polyamide membranes using monochloramine and ferrous iron. *Journal of Membrane Science*, 258(1-2):64–70, 2005.
- [117] R. Sandín, E. Ferrero, C. Repollés, S. Navea, J. Bacardit, J. P. Espinós, and J. J. Malfeito. Reverse osmosis membranes oxidation by hypochlorite and chlorine dioxide: spectroscopic techniques vs. fujiwara test. *Desalination and Water Treatment*, 51(1-3):318–327, 2013.
- [118] K. Hashiba, S. Nakai, W. Nishijima, M. Ohno, and T. Gotoh. Degradation of secondary polyamide reverse osmosis membrane by hypochlorite in the presence of calcium ions. *Polymer Degradation and Stability*, 181:109351, 2020.

- [119] A. Antony, A. Branch, G. Leslie, and P. Le-Clech. Impact of membrane ageing on reverse osmosis performance – implications on validation protocol. *Journal of Membrane Science*, 520:37–44, 2016.
- [120] R. Cruz-Silva, S. Inukai, T. Araki, A. Morelos-Gomez, J. Ortiz-Medina, K. Takeuchi, T. Hayashi, A. Tanioka, S. Tejima, T. Noguchi, M. Terrones, and M. Endo. High performance and chlorine resistant carbon nanotube/aromatic polyamide reverse osmosis nanocomposite membrane. *MRS Advances*, 1(20):1469–1476, 2016.
- [121] Bundesministerium für Gesundheit. Zweite verordnung zur novellierung der trinkwasserverordnung, 23.06.2323.
- [122] J. Oh, H., and Jang. Application of chlorine dioxide (clo₂) to reverse osmosis (ro) membrane for seawater desalination. *Journal of the Taiwan Institute of Chemical Engineers*, 68:281–288, 2016.
- [123] E. Alayemieka and S. Lee. Modification of polyamide membrane surface with chlorine dioxide solutions of differing ph. *Desalination and Water Treatment*, 45(1-3):84–90, 2012.
- [124] J. C. Crittenden. *MWH's water treatment: Principles and design*. John Wiley and Sons, Hoboken, N.J, 3rd ed. edition, 2012.
- [125] A. Antony, J. How Low, St. G., A. E. Childress, P. Le-Clech, and G. Leslie. Scale formation and control in high pressure membrane water treatment systems: A review. *Journal of Membrane Science*, 383(1-2):1–16, 2011.
- [126] M. Kumar, S. Adham, and J. DeCarolis. Reverse osmosis integrity monitoring. *Desalination*, 214(1-3):138–149, 2007.
- [127] C. Niewersch, Christopher Rieth, Leaelaf Hailemariam, Guillem Gilabert Oriol, and Justyna Warczok. Reverse osmosis membrane element integrity evaluation using imperfection model. *Desalination*, 476:114175, 2020.
- [128] T. Yu, C. Xu, F. Chen, H. Yin, H. Sun, L. Cheng, and X. Bi. Microcoagulation improved the performance of the uf-ro system treating the effluent from a coastal municipal wastewater treatment plant: a pilot-scale study. *Journal of Water Reuse and Desalination*, 11(2):177–188, 2021.
- [129] S. T. Mitrouli, M. Kostoglou, and A. J. Karabelas. Calcium carbonate scaling of desalination membranes: Assessment of scaling parameters from dead-end filtration experiments. *Journal of Membrane Science*, 510:293–305, 2016.
- [130] Y.-H. La, R. Sooriyakumaran, D. C. Miller, M. Fujiwara, Y. Terui, K. Yamanaka, B. D. McCloskey, B. D. Freeman, and R. D. Allen. Novel thin film composite membrane containing ionizable hydrophobes: ph-dependent reverse osmosis behavior and improved chlorine resistance. *Journal of Materials Chemistry*, 20(22):4615, 2010.

- [131] M. Stolov and V. Freger. Membrane charge weakly affects ion transport in reverse osmosis. *Environmental Science & Technology Letters*, 7(6):440–445, 2020.
- [132] C. P. Koutsou, S. G. Yiantsios, and A. J. Karabelas. A numerical and experimental study of mass transfer in spacer-filled channels: Effects of spacer geometrical characteristics and schmidt number. *Journal of Membrane Science*, 326(1):234–251, 2009.
- [133] G. Schock and A. Miquel. Mass transfer and pressure loss in spiral wound modules. *Desalination*, 64:339–352, 1987.
- [134] V. A. Haaksman, A. Siddiqui, C. Schellenberg, J. Kidwell, J. S. Vrouwenvelder, and C. Picioreanu. Characterization of feed channel spacer performance using geometries obtained by x-ray computed tomography. *Journal of Membrane Science*, 522:124–139, 2017.
- [135] C. Picioreanu, J. S. Vrouwenvelder, and M.C.M. van Loosdrecht. Three-dimensional modeling of biofouling and fluid dynamics in feed spacer channels of membrane devices. *Journal of Membrane Science*, 345(1-2):340–354, 2009.
- [136] J. Benecke, M. Haas, F. Baur, and M. Ernst. Investigating the development and reproducibility of heterogeneous gypsum scaling on reverse osmosis membranes using real-time membrane surface imaging. *Desalination*, 428:161–171, 2018.
- [137] O. D. Supekar, J. J. Brown, A. R. Greenberg, J. T. Gopinath, and V. M. Bright. Real-time detection of reverse-osmosis membrane scaling via raman spectroscopy. *Industrial & Engineering Chemistry Research*, 57(47):16021–16026, 2018.
- [138] F. Kücke. Die erzeugung von chlordioxid für den menschlichen gebrauch. *Wiley VCH Verlagsgesellschaft*, 2005(103):1–18.
- [139] J. S. Vrouwenvelder, D. A. Graf von der Schulenburg, J. C. Kruithof, M. L. Johns, and M. C. M. van Loosdrecht. Biofouling of spiral-wound nanofiltration and reverse osmosis membranes: a feed spacer problem. *Water research*, 43(3):583–594, 2009.
- [140] O. Ziemann, J. Krauser, P. E. Zamzow, and W. Daum. *POF-Handbuch: Optische Kurzstrecken-Übertragungssysteme*. Springer, Berlin and Heidelberg, 2., bearb. u. erg. aufl. edition, 2007.
- [141] Manuel L. B. Palacio and Bharat Bhushan. Bioadhesion: a review of concepts and applications. *Philosophical transactions. Series A, Mathematical, physical, and engineering sciences*, 370(1967):2321–2347, 2012.
- [142] Wen-Ta Su, Yung-Feng Liao, Chuang-Yu Lin, and Li-Tzu Li. Micropillar substrate influences the cellular attachment and laminin expression. *Journal of biomedical materials research. Part A*, 93(4):1463–1469, 2010.

- [143] Dirk Lehnert, Bernhard Wehrle-Haller, Christian David, Ulrich Weiland, Christoph Ballestrem, Beat A. Imhof, and Martin Bastmeyer. Cell behaviour on micropatterned substrata: limits of extracellular matrix geometry for spreading and adhesion. *Journal of cell science*, 117(Pt 1):41–52, 2004.
- [144] C. Kürzl, T. Tran, and U. Kulozik. Application of a pulsed crossflow to improve chemical cleaning efficiency in hollow fibre membranes following skim milk microfiltration. *Separation and Purification Technology*, 302:122123, 2022.
- [145] C. Kürzl, M. Hartinger, P. Ong, R. Schopf, S. Schiffer, and U. Kulozik. Increasing performance of spiral-wound modules (swms) by improving stability against axial pressure drop and utilising pulsed flow. *Membranes*, 13(9), 2023.
- [146] M. E. Weinberger and U. Kulozik. Pulsatile crossflow improves microfiltration fractionation of cells and proteins. *Journal of Membrane Science*, 629:119295, 2021.
- [147] N. P. Soice, A. R. Greenberg, W. B. Krantz, and A. D. Norman. Studies of oxidative degradation in polyamide ro membrane barrier layers using pendant drop mechanical analysis. *Journal of Membrane Science*, 243(1-2):345–355, 2004.
- [148] DuPont Company. Water chemistry and pretreatment-biological fouling prevention (chlorination/dechlorination).
- [149] G. Lv, D. Shan, Y. Ma, W. Zhang, D. Ciren, S. Jiang, B. Dang, J. Zhang, W. Sun, and H. Mao. In-situ quantitative prediction of pesticide residues on plant surface by atr-ftir technique coupled with chemometrics. *Spectrochimica acta. Part A, Molecular and biomolecular spectroscopy*, 305:123432, 2024.
- [150] A. Céline, O. Gonçalves, F. Jacquemin, and S. Fréour. Qualitative and quantitative assessment of water sorption in natural fibres using atr-ftir spectroscopy. *Carbohydrate polymers*, 101:163–170, 2014.
- [151] P. Desmond, K. T. Huisman, H. Sanawar, N. M. Farhat, J. Traber, E. O. Fridjonsson, M. L. Johns, H. C. Flemming, C. Picioreanu, and J. S. Vrouwenvelder. Controlling the hydraulic resistance of membrane biofilms by engineering biofilm physical structure. *Water research*, 210:118031, 2022.

List of Figures

1.1	A) Composition of a spiral wound module, B) feed spacer from a commercially available LOW 4 Oltremare SWM module.	1
1.2	Top: Reverse osmosis membrane during operation. Shown are the typical cross-flow conditions with a forming boundary layer. The permeate (purified water) is pressed through the membrane. Bottom: Displayed are the four different types of fouling, formed by the rejected water impurities that are concentrated at the boundary layer.	2
1.3	A) Simple reverse osmosis installation with retentate recycling in two stages. B) The first stage is divided into two parallel segments and the retentate is recycled through the second stage to maintain higher cross-flow velocity in the second stage.	3
1.4	Time-dependent biofouling showing the typical phases of formation: 1. lag/accumulation phase, 2. logarithmic or log phase, 3. plateau phase. Adapted from Flemming <i>et al.</i> [57].	9
1.5	Schematic depicting the principles of fiber optic biofilm sensors. A) Orthogonal fiber setup. Microorganisms are detected via backscattered reflected or emitted light. B) The fiber is immersed into the medium, and the fiber cladding is partially removed. Microorganisms are detected by the attenuation of evanescent waves.	10
1.6	Scenarios for the mass transport at the surface of and through the reverse osmosis membrane. A) Cross-flow conditions present in SWMs and membrane flat cells. B) Dead-end conditions. The relevant parameters that are needed to describe the CP is the concentration of the dissolved ions in the bulk (c_B), the concentration of the dissolved ions in the permeate (c_p), the permeate stream Q_P and the retentate stream (Q_r).	16
1.7	A) section of a spacer filled feed channel with the typical feed spacer crossings and the increased pressure drops at the feed spacer crossings. B) flow velocities in a feed spacer square. The graphic is adapted from the results of Picioreanu <i>et al.</i> [135]	19
2.1	Visualization of the main objectives and their relationship	20
3.1	Image processing for crystal detection on the membrane surface. From left to right: Rotated image, taken in transmitted light mode, Cropped image, Contrast stretched grey scaled image, Final binarized image with detected crystals on the surface (white points) and the crystal-ratio=white pixels/total pixels	27
3.2	Polymer optical fiber setup as a sensor for scaling detection	28
3.3	Schematic diagram and photo of the RO pilot plant, involving a cross-flow membrane flat module with POF sensors	30

3.4	Upper part: Transmission data from the POFs immersed in the sulfate solutions. From left to right: Calcium sulfate, strontium sulfate and barium sulfate. Lower Part: Photos of the POFs after the experiments with respective salt crystals on their surfaces. V1, V2, V3 describe the triplicate.	32
3.5	Experimental data from POFs immersed in CaCO_3 -solutions. Top row: transmission data of POFs immersed in a pure CaCO_3 -solution, a solution with 1 mg/l antiscalant (AS) MT4000 and 10 mg/l. Middle row: Development of the pH values of the corresponding experiments. Bottom Row: Photos of the POFs after the experiments with the salt crystals on their surfaces.	33
3.6	Time series from the experiment with CaCO_3 - supersaturating via pH adjustment. The initial pH value is adjusted with hydrochloric acid to 4.5. Then the supersaturation of the CaCO_3 -polymorphs is achieved by dosing 0.1M NaOH into the feed water. The vertical lines mark the first occurrence of supersaturation of the CaCO_3 -polymorphs in the feed and the retentate.	34
3.7	Crystal-RatioTime series with raw images and binarized images. From left to right: no Scaling; light Scaling; progressed scaled membrane .	35
3.8	SEM picture of overlapping calcite crystals on the RO membrane surface. The picture is taken after an experiment with increasing pH value	36
3.9	Time series of an experiment with calcite supersaturation in the retentate stream. The compaction phase of the membrane lasted up to 24 hours. Then the experiment is continued with almost constant saturation conditions where calcite is supersaturated. The pH value is adjusted to 6.8 with HCl at the beginning of the experiment. The vertical lines mark the first occurrence of supersaturation of calcite in the feed and the retentate. MCC and ACC are undersaturated during the experiment.	38
3.10	SEM Picture with a POF imprint from an experiment with constant conductivities and pH values	39
3.11	Integration concept for polymer optical fibers in spiral wound RO-modules: a) POF is replacing a feed-spacer fiber, b) POF with a mirror on the fiber end, c) back and forth integrated POF in the feed-spacer [A26]	41
3.12	Schematic description of the reverse osmosis plant with integrated polymer optical fibers, sensors, and permeate and retentate rejection.	47
3.13	Mode of operation of the fiber-optical sensor. Top: schematic description of the optical fiber with removed fluoropolymer cladding and the two modes of interaction between light and deposits on the surface: scattering and evanescence-based attenuation. Bottom: scanning electron images (SEM) images of the sensor zone. In the left image, the cladding is removed using ethylacetate, and in the right micrograph by mechanical abrasion.	48

3.14	Depiction of the two polymer optical fibers that were included in a feed-spacer-square on the RO membrane surface to enable the detection of biofilm formation.	49
3.15	The process of image registration that was used for image analysis via the four steps of image registration described by Zitová and Flusser .	51
3.16	Plot showing the light transmission of POFs as a function of time. The feed in the experiment was an aqueous NaCl solution (2 g L^{-1}). .	52
3.17	Change in transmitted light intensity as a function of time for POF sensors that were immersed in a water bath, to which yeast was added after a conditioning period of 71 h.	53
3.18	Time series showing the evolution of different selected online parameters. Experimental conditions: dosed nutrients (500, 100, 50) (C:N:P) in feed water (20 % tap water, 80 % desalinated water) from 144 h onwards.	55
3.19	Plots of offline parameters of the biofouling experiment (see figure 3.18).	57
3.20	Plot of a time series from an experiment with cleaning-in-place (CIP) achieved by higher cross-flow velocities on an RO-Membrane with a POF sensor for monitoring and control.	60
3.21	Comparison of parameter changes during the triplicate of biofouling experiments in the RO plant. Time starts when dosing nutrients to the tap water/desalinated water mixture.	61
3.22	(A) Scanning electron microscopy (SEM) cross-section of a compacted DOW XLE reverse osmosis (RO) membrane with the typical layers comprising a polyester base, a polyethersulfone support, and the aramid layer. (B) Chemical structure of the aromatic polyamide (meta-aramid) that is used as a separating layer in RO membranes. Typical RO membranes feature a 10–200 nm thick layer of meta-aramid, which rejects 99 % of the ions dissolved in the water feed. . .	68
3.23	Reaction schemes describing three important manufacturing processes to produce chlorine dioxide. A: Chlorine-chlorite process, B: Persulfate-chlorite process, C: Acid-chlorite process.	71
3.24	Validation of the image analytical quantification of the methylene blue dye test. The plot shows the relationship between the salt passage (SP) and the methylene blue ratio (MBR) as determined by the conductivities of the feed, retentate, and permeate, respectively. The observed linear relation ($R^2 = 95$) serves to validate the image analytical method.	74

- 3.25 Sequential analysis of a damaged membrane using the methylene blue (MB) dye test as well as imaging by scanning electron microscopy (SEM). From left to right: photograph of a membrane after the MB dye test and SEM images of the same section of the membrane showing the physical damage to the membrane surface in greater detail. The images demonstrate the correlation between the visible damage in the MB test (dark blue surrounded area) and the microscale structural damage. 75
- 3.26 Plots of the methylene blue ratio (MBR) determined for DOW XLE membranes soaked in aqueous solutions of different individual components of the chlorine dioxide matrix. Shown are plots of the MBR against (A) the concentration of chlorine dioxide, (B) hypochlorite and hypochlorous acid, (C) persulfate, and (D) chlorite ions. Each data point represents the mean values and the 90 % confidence intervals. The vertical dashed lines mark a worst-case scenario for the case that free chlorine, persulfate or chlorite are present as by-products in a commercial ClO₂ formulation. Such a scenario could be constructed for the case of a chlorine dioxide solution of 60 mmol L⁻¹. 77
- 3.27 (A) FTIR spectra of membranes soaked in 6.9 g L⁻¹ ClO₂ ($c = 102 \text{ mmol L}^{-1}$; red spectrum) and in deionized water for 1 week (black spectrum). The thick lines mark the mean spectrum of the triplicate. The 90 % confidence interval is displayed by the less color-intense area around the mean spectrum. (B) Degradation indices, DI, (see equation 3.7) of three important groups of the FTIR spectrum of the aramid. Shown are DI values of membranes samples soaked in purified chlorine dioxide, free chlorine, persulfate, and chlorite. In analogy to Figure 3.26, the vertical dashed lines mark a worst-case scenario for the byproducts free chlorine, persulfate and chlorite in a chlorine dioxide solution of 60 mmol L⁻¹. 79
- 3.28 Correlation matrix of the DI indexes and the corresponding MBR values. The Pearson correlation coefficients were calculated. The diagonal plots show the histograms of the DI and MBR values, indicating that the major part of the membranes is not severely damaged. 81
- 3.29 XPS analysis of RO membranes: pristine and soaked in 1483 mmol L⁻¹ chlorite, 102 mmol L⁻¹ chlorine dioxide, 14 mmol L⁻¹ hypochlorous acid, and 521 mmol L⁻¹ persulfate. (A) Survey spectrum of a pristine membrane with assigned core level and Auger transitions. (B) C 1s core level and (C) Cl 2p core level of the different membranes. (D) S 2p peak only observed at a membrane soaked in persulfate. The intensity of all spectra is scaled to the total N 1s peak intensity. . . . 82
- 3.30 Evolution of the salt passage (SP) as determined during accelerated damaging experiments with the membrane and a purified chlorine dioxide solution (1 g L⁻¹). 85

-
- 4.1 Plot depicting the salt passage as a function of pH in the feed for different filtration runs through the RO pilot plant. Black traces indicated trials carried out using a phosphate-buffered feed in which no scaling events were detected, while the blue traces correspond to runs with un-buffered feed for which scaling events were detected at pH values above 9.5. The experiments using a phosphate-buffered feed were carried out under comparable experimental conditions to those shown in Figure 3.6. For all trials, the minimum salt passage coincides with the membrane's isoelectric point at pH 8. 92
- 4.2 Diagram depicting the strengths, weaknesses, opportunities, and threats of the overall early POF sensing concept and combined countermeasures to prevent biofouling and scaling in reverse osmosis processes. . . 98
- 4.3 Top: Schematic depicting the application of SWM modules with POFs, antiscalants, and chlorine dioxide in a multi-stage reverse osmosis (RO) plant. The implementation of the POF could allow for detection of both biofouling in the first stage and scaling in the retentate stage. The targeted dosing of chlorine dioxide in the first module and of antiscalants in the latter modules would increase the effectiveness of these countermeasures. Bottom: Plot showing the recovery and concentration factors (left and right y-axes, respectively) that are caused at the indicated SWM stages (x-axis) with 50% recovery per stage. 100

List of Tables

3.1	Overview of the tree publications including title, major objectives, methods and data evaluation and main statements	22
3.2	Examined salt solutions with the individual components from which the crystals on the POF surfaces were formed.	29
3.3	Sensor types in the RO-pilot plant	30
3.4	RO Parameter measured in a reference experiment with 2 g L ⁻¹ NaCl-feed-solution	31
3.5	Relative abundances of MOs from a 16S rRNA analysis of a biofilm on the RO membrane after a 3-week experiment. Not italic: comments to the MO.	59